COUPLING COMPOSITE SCHEMES WITH DIFFERENT TIME STEPS FOR MULTI-SCALE STRUCTURAL DYNAMICS

Sun-Beom Kwon[1] & Arun Prakash[1,*]

[1]Lyles School of Civil and Construction Engineering, Purdue University, West Lafayette, IN 47907, USA

*Address all correspondence to: Arun Prakash, Lyles School of Civil and Construction Engineering, Purdue University, West Lafayette, IN 47907, USA, E-mail: aprakas@purdue.edu

Simulating the dynamics of structural systems containing both stiff and flexible parts with a time integration scheme that uses a uniform time-step for the entire system is challenging because of the presence of multiple spatial and temporal scales in the response. We present, for the first time, a multi-time-step (MTS) coupling method for composite time integration schemes that is well-suited for such stiff-flexible systems. Using this method, the problem domain is divided into smaller subdomains that are integrated using different time-step sizes and/or different composite time integration schemes to achieve high accuracy at a low computational cost. In contrast to conventional MTS methods for single-step schemes, a key challenge with coupling composite schemes is that multiple constraint conditions are needed to enforce continuity of the solution across subdomains. We develop the constraints necessary for achieving unconditionally stable coupling of the composite ρ_∞-Bathe schemes and prove this property analytically. Further, we conduct a local truncation error analysis and study the period elongation and amplitude decay characteristics of the proposed method. Lastly, we demonstrate the performance of the method for linear and nonlinear stiff-flexible systems to show that the proposed MTS method can achieve higher accuracy than existing methods for time integration, for the same computational cost.

KEY WORDS: *Time integration; Domain decomposition; Multi-time-step; Structural dynamics*

1. INTRODUCTION

Simulating the dynamics of structural systems is often conducted by first discretizing the problem domain in space and then using time integration methods to advance the state of the system from

1543–1649/25/$35.00

one time-step to the next (Bathe, 2016; Hughes, 1987; Zienkiewicz and Taylor, 2005). Most commonly, a uniform time-step (UTS) is used for the entire structure where the time integration scheme and the time-step are chosen judiciously to capture the relevant dynamics of the problem. Additional background on UTS time integration schemes and their classification into single-step (SS), Runge-Kutta (RK), and linear multi-step (LMS) schemes is provided in Section 2.1. For multi-scale structures containing both, stiff and flexible components, however, UTS-SS schemes often lead to stability issues and/or spurious oscillations (Bathe and Noh, 2012; Noh and Bathe, 2018). On the other hand, UTS-RK methods, such as the composite ρ_∞-Bathe method (Bathe and Baig, 2005; Noh and Bathe, 2019a), can be configured to achieve accurate solutions to stiff-flexible problems, albeit at a higher computational cost than UTS-SS schemes. Detailed formulation and stability characteristics of the ρ_∞-Bathe method are provided in Section 2.2.

Further, the response of multi-scale structural systems containing both stiff and flexible parts usually spans multiple spatial and temporal scales, making the choice of a single UTS scheme that can capture the system response across all scales very challenging. For such problems, one may employ a domain decomposition (DD) approach to divide the problem into multiple subdomains that can be solved individually and coupled together to obtain the global solution (Dolean et al., 2015; Fragakis and Papadrakakis, 2003, 2004; Toselli and Widlund, 2006). The DD approach enables use of multi-time-step (MTS) methods, as shown in Fig. 1 for instance, where stiff parts of the system are solve with a fine resolution in space and time whereas flexible parts may be simulated with a coarser discretization to save computational time without loss of accuracy. This approach is sometimes also referred to as subcycling or heterogeneous time integration or asynchronous methods (Daniel, 1997; Gravouil et al., 2015; Prakash and Hjelmstad, 2004). Additional background on DD and MTS methods is provided in Section 2.3.

The DD-MTS approach also lends itself naturally to parallelization where subdomains are

solved on different processors simultaneously to reduce the total runtime of the simulation. However, for large problems, of the order of millions of degrees of freedom (DOFs), ensuring scalability (i.e. the rate of reduction of computational time as number of processors are increased) is crucial for efficient parallel computation (Glusa et al., 2020; Keyes, 1998). For DD-based MTS methods, scalability can be achieved by balancing the computational load of the solving individual subdomains among processors (accounting for their different time-steps) and by designing a scalable solver for coupling the subdomain solutions together (Farhat et al., 2000; Jamal et al., 2017).

Despite the superior performance of UTS-RK schemes for stiff-flexible systems and the computational advantages of the DD-MTS approach for multi-scale problems, currently there is no MTS method available in the literature that allows coupling of UTS-RK schemes with different time-steps. In this paper, we develop the first MTS method for an RK scheme for second-order ODEs, namely the composite ρ_∞-Bathe method. First, we formulate the MTS-Bathe method in Section 3. We prove that enforcing the continuity of velocities across the interface between the stiff and flexible subdomains leads to an unconditionally stable method in Section 4. We conduct a local truncation error (LTE) analysis in Section 5 and show that the MTS-Bathe method preserves the order of LTE of the underlying ρ_∞-Bathe method for displacement and velocity. However, due to the presence of Lagrange multipliers, the LTE for accelerations is found to be lower than that of displacements and velocities. Finally, in Section 6, we present several numerical examples of linear and nonlinear structural dynamics to compare the performance of the proposed MTS-Bathe method to the existing methods for stiff-flexible systems. We show that existing MTS methods for SS schemes (such as the MTS-Newmark method) do not perform well for stiff-flexible systems and can lead to unexpectedly large errors (see Section 6.4.2 for details). We also demonstrate the advantage of the proposed MTS-Bathe method over the UTS-Bathe method and the MTS-Newmark method when comparing computational cost and accuracy.

2. BACKGROUND

In this section, we provide the necessary background for key ideas relevant to this article, namely UTS time integration methods, the composite ρ_∞-Bathe method, and using DD in conjunction with MTS.

2.1 Time integration with uniform time-step (UTS) methods

The governing system of ordinary differential equations (ODEs) for structural dynamics is given by:

$$\boldsymbol{M}\boldsymbol{a}(t) + \boldsymbol{D}\boldsymbol{v}(t) + \boldsymbol{K}\boldsymbol{d}(t) = \boldsymbol{f}(t) \tag{1}$$

where matrices $\boldsymbol{M}$, $\boldsymbol{D}$, and $\boldsymbol{K}$ denote the mass, damping and stiffness, respectively and vectors $\boldsymbol{a}$, $\boldsymbol{v}$, $\boldsymbol{d}$, and $\boldsymbol{f}$ denote the acceleration, velocity, displacement, and external force, respectively. Upon time discretization with a time step Δt, we obtain:

$$\boldsymbol{M}\boldsymbol{a}_{n+1} + \boldsymbol{D}\boldsymbol{v}_{n+1} + \boldsymbol{K}\boldsymbol{d}_{n+1} = \boldsymbol{f}_{n+1} \tag{2}$$

where the subscript denotes the instant of time and $\boldsymbol{v}_{n+1}$ and $\boldsymbol{d}_{n+1}$ are approximated with difference equations specific to a time integration scheme. UTS time integration schemes, as shown in Fig. 2, are largely classified into three categories, namely single-step (SS) methods, Runge-Kutta (RK) methods, and linear multi-step (LMS) methods.

SS methods employ known state vectors from the current time step to advance the solution to the next time step, without using multiple intermediate stages. SS methods are the most widely used class of methods which include Newmark-β (Newmark, 1959) (including central difference and trapezoidal rule), three-parameter method (Shao and Cai, 1988) (or equivalently, CH-α (Chung and Hulbert, 1993)), JWH-α (Jansen et al., 2000; Kadapa et al., 2017), HHT-α (Hilber et al., 1977), U0-V0 (Zhou and Tamma, 2004), and numerous others (Bathe, 2016; Hughes, 1987;

Wang et al., 2023; Zienkiewicz and Taylor, 2005).

RK methods are multi-stage methods that divide the time-step Δt into multiple intermediate stages and use the intermediate state vectors to advance the solution. In a similar way, composite time integration methods (e.g. Bathe schemes (Bathe, 2007; Bathe and Baig, 2005)) also divide the time-step into multiple stages and combine two or more different time integration schemes to advance the solution as shown in detail in Section 2.2. Recently, Wang et al. (2023) showed that most of the existing composite time integration schemes belong to the class of RK methods (Kutta, 1901; Runge, 1895). Historically, RK methods have been developed to solve first-order ordinary differential equations (ODEs), while composite time integration schemes have usually been used for second-order ODEs (e.g., structural dynamics).

With LMS schemes, simulations are advanced by using the known state vectors from several previous time-steps. Well-known examples of LMS methods include Adams-Bashforth, Adams-Moulton, and backward difference formulas (BDF) (Bashforth and Adams, 1883; Gear, 1971; Moulton, 1926). Several LMS schemes, such as Park (1975), GBDF (Dong, 2010), and OALTS (Zhang, 2020), and RK schemes, such as Bathe (2007), Kim and Reddy (2017), and Kim and Choi (2018), are able to achieve better performance over the SS schemes, such as Newmark and CH-α, in terms of accuracy and stability, especially for nonlinear problems, as shown in Bathe (2007); Bathe and Baig (2005); Dong (2010); Ji and Xing (2020); Kim (2020); Kim and Choi (2018); Kim and Reddy (2017); Kwon and Lee (2017); Li et al. (2023); Li and Yu (2019); Park (1975); Zhang et al. (2020); Zhang (2020).

2.2 The UTS-Composite ρ_∞-Bathe scheme

In this article, since we develop the first MTS method for a composite time integration scheme where the underlying UTS-Composite method is the ρ_∞-Bathe scheme, we briefly review this

composite time integration method here. The ρ_∞-Bathe scheme followed a sequence of developments by Bathe and his co-workers. Inspired by the TRBDF2 scheme (Bank et al., 1985), Bathe et al. (Bathe, 2007; Bathe and Baig, 2005) developed a composite time integration scheme that uses two sub-steps within each time-step Δt where the first sub-step uses the trapezoidal rule and the second sub-step is advanced with the 3-point backward difference formula. Noh and Bathe (2019a) proposed the ρ_∞-Bathe scheme, which contains not only the standard Bathe and β_1/β_2-Bathe schemes (Malakiyeh et al., 2019) but also the Newmark schemes and the trapezoidal rule (Noh and Bathe, 2019b).

In the ρ_∞-Bathe scheme, each time-step is divided into two sub-steps, as shown in Fig. 3, $t_n \to t_{n+\gamma}$ and $t_{n+\gamma} \to t_{n+1}$ where $t_{n+\gamma} = t_n + \gamma\Delta t$ and γ is the splitting ratio. The ρ_∞-Bathe scheme (Noh and Bathe, 2019a) can then be written in the following form:

$$\begin{aligned} \mathbb{M}_1 \boldsymbol{z}_{n+\gamma} &= \boldsymbol{r}_{n+\gamma} - \mathbb{N}_1 \boldsymbol{z}_n \\ \mathbb{M}_2 \boldsymbol{z}_{n+1} &= \boldsymbol{r}_{n+1} - \mathbb{N}_2 \boldsymbol{z}_{n+\gamma} - \mathbb{O}_2 \boldsymbol{z}_n \end{aligned} \tag{3}$$

where

$$\begin{aligned} \mathbb{M}_1 &= \begin{bmatrix} \boldsymbol{M} & \boldsymbol{D} & \boldsymbol{K} \\ -\frac{\gamma\Delta t}{2}\boldsymbol{I} & \boldsymbol{I} & 0 \\ 0 & -\frac{\gamma\Delta t}{2}\boldsymbol{I} & \boldsymbol{I} \end{bmatrix}, \quad \mathbb{M}_2 = \begin{bmatrix} \boldsymbol{M} & \boldsymbol{D} & \boldsymbol{K} \\ -s_2\Delta t\boldsymbol{I} & \boldsymbol{I} & 0 \\ 0 & -q_2\Delta t\boldsymbol{I} & \boldsymbol{I} \end{bmatrix} \\ \mathbb{N}_1 &= \begin{bmatrix} 0 & 0 & 0 \\ -\frac{\gamma\Delta t}{2}\boldsymbol{I} & -\boldsymbol{I} & 0 \\ 0 & -\frac{\gamma\Delta t}{2}\boldsymbol{I} & -\boldsymbol{I} \end{bmatrix}, \quad \mathbb{N}_2 = \begin{bmatrix} 0 & 0 & 0 \\ -s_1\Delta t\boldsymbol{I} & 0 & 0 \\ 0 & -q_1\Delta t\boldsymbol{I} & 0 \end{bmatrix} \\ \mathbb{O}_2 &= \begin{bmatrix} 0 & 0 & 0 \\ -s_0\Delta t\boldsymbol{I} & -\boldsymbol{I} & 0 \\ 0 & -q_0\Delta t\boldsymbol{I} & -\boldsymbol{I} \end{bmatrix}, \quad \boldsymbol{z} = \begin{bmatrix} \boldsymbol{a} \\ \boldsymbol{v} \\ \boldsymbol{d} \end{bmatrix}, \quad \boldsymbol{r} = \begin{bmatrix} \boldsymbol{f} \\ 0 \\ 0 \end{bmatrix} \end{aligned} \tag{4}$$

and s_0, s_1, s_2, q_0, q_1, and q_2 are Bathe parameters, and $\boldsymbol{I}$ is the identity matrix. Subscripts $[\,]_1$ and $[\,]_2$ represent the first and second sub-steps, respectively, of the ρ_∞-Bathe scheme.

The ρ_∞-Bathe scheme is defined by two parameters, ρ_∞ and γ, and leads to second- or third-order accuracy with unconditional stability when the Bathe parameters are chosen as:

$$\begin{aligned} &s_1 = q_1 = \frac{\rho_\infty + 1}{2\gamma(\rho_\infty - 1) + 4}; \\ &s_0 = q_0 = (\gamma - 1)q_1 + \frac{1}{2}; \quad \text{and} \quad s_2 = q_2 = -\gamma q_1 + \frac{1}{2} \end{aligned} \tag{5}$$

Values for ρ_∞ can be chosen in the closed interval $[-1, 1]$ and γ can take any value, including complex values. Note that with $\rho_\infty = 0$ this time stepping method reduces to the standard Bathe scheme (also referred to as the γ-Bathe scheme). For $\rho_\infty \in [0, 1]$, one obtains identical effective stiffness matrices for each sub-step for the following choice of γ_0

$$\gamma_0 = \begin{cases} \dfrac{2 - \sqrt{2 + 2\rho_\infty}}{1 - \rho_\infty} & \text{for} \quad \rho_\infty \in [0, 1) \\ 0.5 & \text{for} \quad \rho_\infty = 1 \end{cases} \tag{6}$$

This choice leads to maximum amplitude decay and minimum period elongation (Noh and Bathe, 2019a), whereas for $\rho_\infty \in (-1, 1 - \sqrt{3}]$, the scheme is third-order accurate for the following value for γ (Kwon et al., 2021; Noh and Bathe, 2019b):

$$\gamma_p = \frac{\rho_\infty + 2 - \sqrt{\rho_\infty^2 - 2\rho_\infty - 2}}{3(\rho_\infty + 1)} \quad \text{for} \quad \rho_\infty \in (-1, 1 - \sqrt{3}] \tag{7}$$

Note that ρ_∞ is an algorithmic parameter and the spectral radius, $\rho \to |\rho_\infty|$ as $\Delta t \to \infty$ (Noh and Bathe, 2019b). Thus, even negative values of $\rho_\infty \in [-1, 0]$ lead to unconditionally stable methods. Note that the ρ_∞-Bathe scheme is only A-stable and not BN-stable. It can achieve L-stability when $\rho_\infty = 0$ which is suitable for linear stiff problems (for details, see page 44 of the text by Wanner and Hairer (1996)).

On the other hand, the β_1/β_2-Bathe scheme is obtained for the following choice of parameters:

$$\begin{aligned} &s_0 = q_0 = \gamma(1-\beta_1); \\ &s_1 = q_1 = \gamma(\beta_1+\beta_2-1)+1-\beta_2; \quad \text{and} \quad s_2 = q_2 = (1-\gamma)\beta_2 \end{aligned} \tag{8}$$

The β_1/β_2-Bathe scheme is a three-parameter scheme. Malakiyeh et al. (2019) proposed using $\gamma = 0.5$ along with the choice of β_1 and β_2 as either $\beta_2 = 1-\beta_1$ or $\beta_2 = 2\beta_1$. Note that the ρ_∞-Bathe scheme with $\gamma = 0.5$ and β_1/β_2-Bathe scheme with $\beta_2 = 1-\beta_1$ yield the same characteristics (Kwon et al., 2020). The ρ_∞-Bathe scheme for certain choice of parameters (see Noh and Bathe (2019a,b) for details) has identical spectral properties to the two-step Newmark method with $\alpha = 0.25(\delta+0.5)^2$.

Table 1 lists common choices of the ρ_∞-Bathe parameters and the associated characteristics of the resulting schemes. In addition, unconditionally stable Bathe schemes that are first-, second- or third-order accurate, depending on the values of the Bathe parameters, can also be designed (Kwon et al., 2021). Further, optimal use of Bathe schemes was investigated for the solution of transient wave propagation with linear finite elements (Kwon et al., 2020; Li et al., 2021) and overlapping finite elements (Kim and Bathe, 2021), and optimal load selection at the sub-step for Bathe schemes was identified (Kwon et al., 2021). In general, however, the choice of ρ_∞-Bathe parameters and the time-step Δt is based on the dynamic characteristics of the problem at hand. Table 1 and Noh and Bathe (2019a,b) may be used as a guideline for the selection of ρ_∞-Bathe parameters and for the time-step typically, one would use a value that is one-tenth of the time period corresponding to the highest frequency of interest. For wave propagation problems, the time-step for the Bathe method can be obtained from the Courant–Friedrichs–Lewy (CFL) condition (Kwon et al., 2020; Noh et al., 2013).

Systems that are composed of mechanically stiff and flexible substructures, such as the one

shown in Fig. 1 occur frequently in practice. The difference in stiffness of between the substructures may be physical (e.g. resulting from additional construction over an existing structure) or it may be numerical (e.g. presence of penalty constraints, or rigid links connecting different components, or contact with a large stiff body and similar other scenarios) – see Bathe (2016); Bathe and Noh (2012); Noh and Bathe (2018) for details. While UTS-SS methods work well for most problems in structural dynamics, one often encounters stability issues and/or spurious oscillations when simulating such stiff-flexible systems with these methods (Bathe and Noh, 2012; Ji and Xing, 2020; Kadapa et al., 2017; Kim, 2020; Kim and Choi, 2018; Kim and Reddy, 2017; Noh and Bathe, 2018, 2019a,b, 2023; Zhang, 2020). In contrast, UTS-RK methods such as the composite ρ_∞-Bathe method can achieve accurate solutions to stiff-flexible problems for certain choice of parameters as listed in Table 1.

Finally, since we are developing a MTS method for the ρ_∞-Bathe scheme, it is helpful to cast it in a form which shows how the solution can be advanced by m time-steps from t_0 to t_m (or t_n to t_{n+m}, in general). This is achieved by solving the following lower triangular system:

$$\begin{bmatrix} \mathbb{M}_1 & & & & & & \\ \mathbb{N}_2 & \mathbb{M}_2 & & & & & \\ & \mathbb{N}_1 & \mathbb{M}_1 & & & & \\ & \mathbb{O}_2 & \mathbb{N}_2 & \mathbb{M}_2 & & & \\ & & \ddots & \ddots & \ddots & & \\ & & & & \mathbb{N}_1 & \mathbb{M}_1 & \\ & & & & \mathbb{O}_2 & \mathbb{N}_2 & \mathbb{M}_2 \end{bmatrix} \begin{bmatrix} \boldsymbol{z}_\gamma \\ \boldsymbol{z}_1 \\ \boldsymbol{z}_{1+\gamma} \\ \boldsymbol{z}_2 \\ \vdots \\ \boldsymbol{z}_{m-1+\gamma} \\ \boldsymbol{z}_m \end{bmatrix} = \begin{bmatrix} \boldsymbol{r}_\gamma - \mathbb{N}_1 \boldsymbol{z}_0 \\ \boldsymbol{r}_1 - \mathbb{O}_2 \boldsymbol{z}_0 \\ \boldsymbol{r}_{1+\gamma} \\ \boldsymbol{r}_2 \\ \vdots \\ \boldsymbol{r}_{m-1+\gamma} \\ \boldsymbol{r}_m \end{bmatrix} \tag{9}$$

Since the system is lower triangular, it can be solved easily from top to bottom using forward substitution. This is identical to conventional time stepping with a UTS method.

Stability of the ρ_∞-Bathe scheme has been proven using a spectral analysis (Bathe and Noh,

2012; Noh and Bathe, 2019a). However, to facilitate a proof of stability for the proposed MTS-Bathe method (presented later in Section 4), we first derive an energy balance equation for the UTS-Bathe scheme using the approach presented by Hughes et al. (Hughes, 1987; Hughes and Liu, 1978b).

Using modal decomposition (Zienkiewicz and Taylor, 2005), the governing system of second-order ODEs for structural dynamics shown in Eq. (1) for a multi-degree of freedom (MDOF) system is decoupled into a number of scalar second-order ODEs governing the behavior of each single-degree of freedom (SDOF) mode. This replaces matrices and vectors with their modal scalar equivalents: $\boldsymbol{M} \rightarrow 1$; $\boldsymbol{K} \rightarrow \omega_0^2$; $\boldsymbol{a} \rightarrow a$; $\boldsymbol{v} \rightarrow v$; $\boldsymbol{d} \rightarrow d$; and $\boldsymbol{f} \rightarrow r$ (where ω_0 is the modal natural frequency and r is the generalized force). Next, we define:

$$\Delta KE[a] = (a_{n+1}^2 - a_n^2)/2; \quad \Delta PE[v] = (v_{n+1}^2 - v_n^2)\omega_0^2/2; \tag{10}$$

as the change in kinetic and potential energies from t_n to t_{n+1}.

Note that stability requires that $\Delta KE[a] + \Delta PE[v] \leq 0$ because that ensures that a_{n+1} and v_{n+1} will be bounded as long as a_n and v_n are bounded. Consequently, from the governing Eq. (1), d_{n+1} will also be bounded as long as d_n is bounded. Expressing a_{n+1} and v_{n+1} in terms of a_n, v_n, d_n, $r_{n+\gamma}$, and r_{n+1} using the relationships of the Bathe scheme and the time discretized equations of motion (Eq. (3)), one can derive the following result:

$$\Delta KE[a] + \Delta PE[v] = -D[\Delta a, \Delta v] + E_{ext}[\Delta a, \Delta v, \Delta r, \Delta_\gamma r] \tag{11}$$

where D and E_{ext} represent numerical damping, and work due to external forces, respectively.

These quantities are defined as:

$$D[\Delta a, \Delta v] = \frac{(1-\rho_\infty^2)\gamma^2(1-\gamma)^2\Delta t^2\omega_0^2\left\{\Delta a^2 + \Delta v^2\omega_0^2\right\}}{8(2-\gamma(1-\rho_\infty))^2 + 2(1-\rho_\infty)^2\gamma^2(1-\gamma)^2\Delta t^2\omega_0^2}; \tag{12}$$

$$E_{ext}[\Delta a, \Delta v, \Delta r, \Delta_\gamma r] = \frac{1}{\Delta t}\Delta v\Delta r + \eta_\rho[\Delta a, \Delta v](\gamma\Delta r - \Delta_\gamma r) \tag{13}$$

where

$$\eta_\rho[\Delta a, \Delta v] = (1+\rho_\infty)\frac{2(2-\gamma(1-\rho_\infty))\Delta a + (1-\rho_\infty)\gamma(1-\gamma)\Delta t\omega_0^2\Delta v}{4(2-\gamma(1-\rho_\infty))^2 + (1-\rho_\infty)^2\gamma^2(1-\gamma)^2\Delta t^2\omega_0^2}$$

and the operators Δ and Δ_γ are defined as: $\Delta(\cdot) = (\cdot)_{n+1} - (\cdot)_n$ and $\Delta_\gamma(\cdot) = (\cdot)_{n+\gamma} - (\cdot)_n$ respectively.

Since E_{ext} has no impact on stability of time integration schemes (Liu and Belytschko, 1982), stability condition is $D \geq 0$. From Eq. (12), one may verify that the denominator is always positive and the numerator will be non-negative as long as $|\rho_\infty| \leq 1$. Therefore, the ρ_∞-Bathe scheme is unconditionally stable when $|\rho_\infty| \leq 1$ for any value of γ. This is identical to stability result derived from spectral radius of the amplification matrix in Noh and Bathe (2019a).

2.3 Domain decomposition and multi-time-step methods

We present the finite element tearing and interconnecting (FETI) method – a domain decomposition method based on the dual-Schur complement approach – and discuss the use of multiple time-steps in conjunction with it. The FETI method was proposed by Farhat and Roux (Farhat et al., 1994a; Farhat and Roux, 1991, 1994) and uses element partitioning and Lagrange multipliers to enforce kinematic continuity at the interface of shared nodes between the subdomains. Using the FETI method, a problem domain Ω is decomposed into two subdomains Ω^A and Ω^B with an internal boundary Γ^I as shown in Fig. 1. Lagrange multipliers, $\boldsymbol{\lambda}$, are used to impose

the continuity of kinematic quantities, such as displacement, velocity, and acceleration, at the internal boundary (see Farhat and Roux (1991) for general framework). Gravouil and Combescure (Combescure and Gravouil, 2002; Gravouil and Combescure, 2001) formulated a MTS method for Newmark schemes and found that imposing continuity of velocities at the fine time-scale results in a stable, but dissipative algorithm. Prakash and Hjelmstad (Prakash and Hjelmstad, 2004; Prakash et al., 2014) proposed a modified MTS method imposing continuity of velocities at the coarse time-scale to eliminate numerical dissipation and lower the computational cost. This method is unconditionally stable and preserves the energy norms of individual subdomains. We refer to this method as the MTS-Newmark method in this article and use it as a benchmark to compare the performance of the proposed MTS-Bathe method.

For the MTS-Newmark method, the semi-discrete equations of motion of a decomposed system, such as that shown in Fig. 1, are given as:

$$\boldsymbol{M}^A\boldsymbol{a}^A(t) + \boldsymbol{D}^A\boldsymbol{v}^A(t) + \boldsymbol{K}^A\boldsymbol{d}^A(t) + \boldsymbol{C}^{A^T}\boldsymbol{\lambda}(t) = \boldsymbol{f}^A(t) \tag{14}$$

$$\boldsymbol{M}^B\boldsymbol{a}^B(t) + \boldsymbol{D}^B\boldsymbol{v}^B(t) + \boldsymbol{K}^B\boldsymbol{d}^B(t) + \boldsymbol{C}^{B^T}\boldsymbol{\lambda}(t) = \boldsymbol{f}^B(t) \tag{15}$$

$$\boldsymbol{C}^A\boldsymbol{w}^A(t) + \boldsymbol{C}^B\boldsymbol{w}^B(t) = 0 \tag{16}$$

where superscripts A and B denote the subdomain, $\boldsymbol{\lambda}$ is the Lagrange multiplier, and $\boldsymbol{C}$ represents the Boolean connectivity matrix across the interface. In Eq. (16), $\boldsymbol{w}$ may be replaced by either $\boldsymbol{a}$, $\boldsymbol{v}$, or $\boldsymbol{d}$ to enforce the continuity of accelerations, velocities, or displacements, respectively. Lagrange multipliers, $\boldsymbol{\lambda}(t)$, represent the internal forces between the two subdomains. For further details, see Prakash and Hjelmstad (2004).

In contrast to a UTS method, where one uses a uniform time-step for the entire problem domain, the MTS method uses two different time-steps for subdomains Ω^A and Ω^B. As shown in Fig. 1, the flexible subdomain Ω^A is advanced with a large time-step ΔT and the stiff subdomain

Ω^B is advanced with a small time-step Δt. Note that $\Delta T = m\Delta t$ where m is the time-step ratio between the two subdomains. The fully discrete equations of motion for advancing the solution from t_0 to t_m are:

$$\boldsymbol{M}^A \boldsymbol{a}_m^A + \boldsymbol{D}^A \boldsymbol{v}_m^A + \boldsymbol{K}^A \boldsymbol{d}_m^A + \boldsymbol{C}^{A^T} \boldsymbol{\lambda}_m = \boldsymbol{f}_m^A \tag{17}$$

$$\boldsymbol{M}^B \boldsymbol{a}_j^B + \boldsymbol{D}^B \boldsymbol{v}_j^B + \boldsymbol{K}^B \boldsymbol{d}_j^B + \boldsymbol{C}^{B^T} \boldsymbol{\lambda}_j = \boldsymbol{f}_j^B \quad \text{for } j = 1, 2, ..., m \tag{18}$$

$$\boldsymbol{C}^A \boldsymbol{w}_m^A + \boldsymbol{C}^B \boldsymbol{w}_m^B = 0 \tag{19}$$

$$\boldsymbol{C}^A \boldsymbol{h}_j^A + \boldsymbol{C}^B \boldsymbol{h}_j^B = 0 \quad \text{for } j = 1, 2, ..., (m-1) \tag{20}$$

where the subscripts refer to the time-step as depicted in Fig. 1 and vector $\boldsymbol{h}$ depends upon the time integration method used and the coupling constraints chosen for the specific MTS method. Together with the difference equations of the underlying time integration scheme, these equations are used to advance the solution for the entire problem domain from t_0 to t_m. This process is called *block*-time-stepping and can be repeated successively to advance the simulation.

One finds numerous MTS methods that combine different SS schemes in the literature leading to different stability and accuracy characteristics. There are methods that enable coupling of implicit and explicit schemes in different subdomains, but with a single time-step (Belytschko and Mullen, 1976; Hughes and Liu, 1978a,b; Park, 1980) or methods that use different time-steps in different subdomains (Belytschko et al., 1984, 1979; Daniel, 1997; Liu and Belytschko, 1982; Smolinski, 1992). While these methods try to combine different time integration schemes, their stability and accuracy, in general, is not guaranteed and is sometimes problem-dependent. More recently, MTS methods for Newmark time integration schemes were developed by Gravouil and Combescure (Combescure and Gravouil, 2002; Gravouil and Combescure, 2001) and modified by Prakash and Hjelmstad (Prakash and Hjelmstad, 2004; Prakash et al., 2014) that provide excellent stability and accuracy behavior. Mahjoubi et al. (2011) proposed an energy conserving

MTS method to couple the Simo, Krenk, Verlet, HHT-α as well as Newmark schemes. Brun et al. (2015) formulated two MTS methods for Newmark and HHT-α, WBZ-α, and CH-α schemes. Despite the advantages of MTS methods that combine two or more SS schemes, there is currently no work in the literature that formulates a MTS method to combine RK schemes or LMS schemes for second-order ODEs. Some studies have developed DD and MTS methods to combine RK schemes for first-order ODEs (Arrarás et al., 2014; Golbabai and Javidi, 2009; Javidi and Golbabai, 2009; Liang et al., 2019; Nakshatrala et al., 2008, 2009), but not for second-order ODEs. This is a gap in the current literature that the present article addresses.

While the total computational cost of a MTS method is usually lower than that of its underlying UTS methods, ensuring scalability of the method is essential for realizing this gain in performance. Usually, the solution of individual subdomains may be computed on different cores independently of each other and scales well. However, coupling the subdomain solutions together requires communication between the subdomains and is difficult to parallelize efficiently. To overcome this challenge, Farhat and coworkers (Farhat et al., 1995, 2001; Farhat and Mandel, 1998; Farhat et al., 1994b; Farhat and Roux, 1991) developed different implementations of the FETI method where direct solvers are used to compute the solution for each subdomain and an iterative preconditioned conjugate gradient (PCG) solver is used to couple the subdomains solutions. Specifically, the FETI-DP implementation (Farhat et al., 2001) is shown to be scalable because the matrix-vector products needed for the PCG method are readily computed using scalable parallel subdomain solvers and it introduces a coarse problem on the interface to ensure that the number of iterations needed for convergence remains relatively constant as the number of subdomains increases. This approach is effective for static problems and for problems in which the dynamics can be captured well using a UTS approach. However, for the MTS method, one must also account for the difference in time-steps among the subdomains for effective computational load balance between processors. Additionally, the condition number of the coupling operator may worsen as

the ratio of maximum time-step to the minimum time-step increases. This may lead to an increase in the number of iterations needed for convergence and cause loss of scalability. A detailed study of the scalability that addresses these and other issues associated with DD-based MTS methods is beyond the scope of this article and is left as future research.

3. THE MTS-BATHE COUPLING METHOD

In this section we develop a novel MTS method for ρ_∞-Bathe schemes that allows one to decompose a problem domain into smaller subdomains and use different ρ_∞-Bathe schemes and/or different time-steps in each domain to solve problems with multiple temporal scales, such as the stiff-flexible system depicted in Fig. 1. For ease of presentation, we only consider two subdomains Ω^A and Ω^B. The method can be extended for multiple (more than two) subdomains in a manner similar to the technique described by Jamal et al. (2017).

Based on Fig. 1, the time-steps ΔT and Δt, and the Bathe parameters γ^A, γ^B, ρ_∞^A and ρ_∞^B for subdomains Ω^A and Ω^B should be chosen in accordance with their dynamic characteristics, as one would do when selecting these algorithmic parameters for any UTS-Bathe scheme. A detailed view of the time-steps shown in Fig. 1 is provided in Fig. 4, which illustrates the MTS-Bathe method for one *block*-time-step from t_0 to t_m. In the derivation that follows, a superscript A or B denotes the subdomain and the subscript denotes the instant of time within the interval t_0 to t_m as shown in Fig. 4. To advance the solution by one block time-step, we need to compute the state variables for subdomains Ω^A and Ω^B at all intermediate time-steps t_{j+1}, sub-time-steps $t_{j+\gamma^B}$ (where $j = 0, 1, ..., m-1$), and $t_{\gamma^A m}$.

First, we follow the notation of Sections 2.2 and 2.3 to write the fully discretized equations for

Ω^A and Ω^B as:

$$\mathbb{M}_1^A \boldsymbol{z}_{\gamma^A m}^A + \mathbb{C}^{A^T} \boldsymbol{\lambda}_{\gamma^A m} = \boldsymbol{r}_{\gamma^A m}^A - \mathbb{N}_1^A \boldsymbol{z}_0^A \tag{21}$$

$$\mathbb{M}_2^A \boldsymbol{z}_m^A + \mathbb{C}^{A^T} \boldsymbol{\lambda}_m = \boldsymbol{r}_m^A - \mathbb{N}_2^A \boldsymbol{z}_{\gamma^A m}^A - \mathbb{O}_2^A \boldsymbol{z}_0^A \tag{22}$$

$$\mathbb{M}_1^B \boldsymbol{z}_{j+\gamma^B}^B + \mathbb{C}^{B^T} \boldsymbol{\lambda}_{j+\gamma^B} = \boldsymbol{r}_{j+\gamma^B}^B - \mathbb{N}_1^B \boldsymbol{z}_j^B \quad \text{for } j = 0, 1, ..., m-1 \tag{23}$$

$$\mathbb{M}_2^B \boldsymbol{z}_{j+1}^B + \mathbb{C}^{B^T} \boldsymbol{\lambda}_{j+1} = \boldsymbol{r}_{j+1}^B - \mathbb{N}_2^B \boldsymbol{z}_{j+\gamma^B}^B - \mathbb{O}_2^B \boldsymbol{z}_j^B \quad \text{for } j = 0, 1, ..., m-1 \tag{24}$$

where $\mathbb{C}^A = \left[\boldsymbol{C}^A,\, 0,\, 0\right]$ and $\mathbb{C}^B = \left[\boldsymbol{C}^B,\, 0,\, 0\right]$. Note that these equations advance subdomain Ω^A by ΔT and subdomain Ω^B by m times Δt. To aid the computation of the Lagrange multipliers, $\boldsymbol{\lambda}_k$, at the intermediate time-instants t_k (where $k = j + \gamma^B$ and $j+1$), state variables for subdomain Ω^A at the same instants are obtained by piecewise linear interpolation and extrapolation as:

$$\boldsymbol{z}_k^A = c_{0,k} \boldsymbol{z}_0^A + c_{1,k} \boldsymbol{z}_{\gamma^A m}^A + c_{2,k} \boldsymbol{z}_m^A \tag{25}$$

where

$$\begin{array}{lllll}
\text{For } 0 < \gamma^A < 1: & c_{0,k} = \frac{\gamma^A m - k}{\gamma^A m}; & c_{1,k} = \frac{k}{\gamma^A m} & \text{when } k \le \gamma^A m \\
& c_{0,k} = 0; & c_{1,k} = \frac{m-k}{(1-\gamma^A)m} & \text{when } k > \gamma^A m \\
\text{For } \gamma^A > 1: & c_{0,k} = \frac{m-k}{m}; & c_{1,k} = 0 & \text{when } k \le m \\
& c_{0,k} = 0; & c_{1,k} = \frac{m-k}{(1-\gamma^A)m} & \text{when } k > m \\
\text{For } \gamma^A < 0: & c_{0,k} = \frac{\gamma^A m - k}{\gamma^A m}; & c_{1,k} = \frac{k}{\gamma^A m} & \text{when } k \le 0 \\
& c_{0,k} = \frac{m-k}{m}; & c_{1,k} = 0 & \text{when } k > 0
\end{array} \tag{26}$$

with $c_{2,k} = 1 - c_{0,k} - c_{1,k}$. Note that the time-instant $t_{\gamma^A m}$ need not coincide with any intermediate time-step t_k. However, in the case that some value of k is equal to $\gamma^A m$, Eqs. (26) still hold.

Next, we develop a relationship between the Lagrange multipliers at the intermediate time-instants t_k and the Lagrange multipliers at the end of the block time-steps, t_0 and t_m. This is

achieved by restricting the equation of motion for subdomain Ω^A at the interface for the intermediate time-instants t_k as:

$$\boldsymbol{C}^A \left[\boldsymbol{M}^A \boldsymbol{a}_k^A + \boldsymbol{D}^A \boldsymbol{v}_k^A + \boldsymbol{K}^A \boldsymbol{d}_k^A + \boldsymbol{C}^{A^T} \boldsymbol{\lambda}_k \right] = \boldsymbol{C}^A \boldsymbol{f}_k^A \tag{27}$$

Noting that $\boldsymbol{C}^A \boldsymbol{C}^{A^T} = \boldsymbol{I}^\lambda$, which is an identity matrix of size of number of degrees of freedom on the interface (Prakash and Hjelmstad, 2004), Eq. (27) can be rewritten as:

$$\mathbb{C}^A \mathbb{M}^A \boldsymbol{z}_k^A + \boldsymbol{\lambda}_k = \boldsymbol{C}^A \boldsymbol{f}_k^A \tag{28}$$

where $\mathbb{C}^A \mathbb{M}^A = \boldsymbol{C}^A \left[\boldsymbol{M}^A, \boldsymbol{D}^A, \boldsymbol{K}^A \right]$. Substituting Eqs. (21), (22) and (25) into Eq. (28) leads to the following expression for the Lagrange multipliers at the intermediate time-instants $\boldsymbol{\lambda}_k$:

$$\boldsymbol{\lambda}_k = \tilde{\boldsymbol{\lambda}}_k + c_{1,k} \boldsymbol{\lambda}_{\gamma^A m} + c_{2,k} \boldsymbol{\lambda}_m \tag{29}$$

where

$$\tilde{\boldsymbol{\lambda}}_k = \boldsymbol{C}^A \left[\boldsymbol{f}_k^A - c_{1,k} \boldsymbol{f}_{\gamma^A m}^A - c_{2,k} \boldsymbol{f}_m^A \right] - c_{0,k} \mathbb{C}^A \mathbb{M}^A \boldsymbol{z}_0^A \tag{30}$$

Finally, using Eq. (29), equations of motion for subdomain Ω^B (i.e. Eqs. (23) and (24)) can be rewritten as:

$$\mathbb{M}_1^B \boldsymbol{z}_{j+\gamma^B}^B + c_{1,j+\gamma^B} \mathbb{C}^{B^T} \boldsymbol{\lambda}_{\gamma^A m} + c_{2,j+\gamma^B} \mathbb{C}^{B^T} \boldsymbol{\lambda}_m = \boldsymbol{r}_{j+\gamma^B}^B - \mathbb{N}_1^B \boldsymbol{z}_j^B - \mathbb{C}^{B^T} \tilde{\boldsymbol{\lambda}}_{j+\gamma^B} \tag{31}$$

$$\mathbb{M}_2^B \boldsymbol{z}_{j+1}^B + c_{1,j+1} \mathbb{C}^{B^T} \boldsymbol{\lambda}_{\gamma^A m} + c_{2,j+1} \mathbb{C}^{B^T} \boldsymbol{\lambda}_m = \boldsymbol{r}_{j+1}^B - \mathbb{N}_2^B \boldsymbol{z}_{j+\gamma^B}^B - \mathbb{O}_2^B \boldsymbol{z}_j^A - \mathbb{C}^{B^T} \tilde{\boldsymbol{\lambda}}_{j+1} \tag{32}$$

Thus, the final system of equations to be solved for block-time-stepping subdomains Ω^A and Ω^B from t_0 to t_m are Eqs. (21), (22), (31), and (32). The only unknowns remaining in these

equations are two Lagrange multipliers $\boldsymbol{\lambda}_{\gamma^A m}$ and $\boldsymbol{\lambda}_m$ across the interface between subdomains Ω^A and Ω^B. The constraint conditions needed to compute these Lagrange multipliers are discussed next.

3.1 Constraint conditions for computing Lagrange multipliers

Unlike the MTS method for Newmark schemes, which use a single constraint equation to enforce continuity of velocities at the final time-step t_m (Gravouil and Combescure, 2001; Prakash and Hjelmstad, 2004), for composite time integration schemes, we need two constraint equations to compute the two Lagrange multipliers, $\boldsymbol{\lambda}_{\gamma^A m}$ and $\boldsymbol{\lambda}_m$. We evaluated the stability behavior of several combinations of constraint conditions. We present three representative constraint conditions here that show all three types of stability behavior: stable, conditionally stable, and unstable. The following three cases describe these constraint conditions across the interface between subdomains Ω^A and Ω^B:

- *Case 1*: displacement continuity at t_m and linear interpolation for $\boldsymbol{\lambda}_{\gamma^A m}$
- *Case 2*: velocity continuity at t_m and linear interpolation for $\boldsymbol{\lambda}_{\gamma^A m}$
- *Case 3*: acceleration continuity at t_m and linear interpolation for $\boldsymbol{\lambda}_{\gamma^A m}$

For all three cases, the constraint condition, at the final time-step t_m can be written as:

$$\mathbb{B}^A \boldsymbol{z}_m^A + \mathbb{B}^B \boldsymbol{z}_m^B = 0 \tag{33}$$

where the matrices $\mathbb{B}^A$ and $\mathbb{B}^B$ are defined as

$$\mathbb{B}^A \equiv \begin{cases} [0,\, 0,\, \boldsymbol{C}^A] & \text{for case 1} \\ [0,\, \boldsymbol{C}^A,\, 0] & \text{for case 2} \\ [\boldsymbol{C}^A,\, 0,\, 0] & \text{for case 3} \end{cases} \quad \text{and} \quad \mathbb{B}^B \equiv \begin{cases} [0,\, 0,\, \boldsymbol{C}^B] & \text{for case 1} \\ [0,\, \boldsymbol{C}^B,\, 0] & \text{for case 2} \\ [\boldsymbol{C}^B,\, 0,\, 0] & \text{for case 3} \end{cases} \tag{34}$$

In addition, Lagrange multipliers at the intermediate time-instant $t_{\gamma^A m}$ are obtained by linear interpolation between t_0 and t_m:

$$\boldsymbol{\lambda}_{\gamma^A m} = (1-\gamma^A)\boldsymbol{\lambda}_0 + \gamma^A \boldsymbol{\lambda}_m \tag{35}$$

Thus, constraint equations (33) and (35) together with Eqs. (21), (22), (31), and (32) are the final set of equations to be solved for block-time-stepping subdomains Ω^A and Ω^B from t_0 to t_m. To solve these equations, we use a bordered solution procedure described in the next subsection.

To aid in the development of the bordered system of equations, we first write Eq. (35) in a modified form as follows. Multiplying equations of motion for subdomain Ω^B at t_0 and t_m by $(1-\gamma^A)$ and γ^A, respectively, we obtain:

$$\left[\boldsymbol{M}^B,\, \boldsymbol{D}^B,\, \boldsymbol{K}^B\right]\left((1-\gamma^A)\boldsymbol{z}_0^B + \gamma^A \boldsymbol{z}_m^B\right) + \boldsymbol{C}^{B^T}\boldsymbol{\lambda}_{\gamma^A m} = (1-\gamma^A)\boldsymbol{f}_0^B + \gamma^A \boldsymbol{f}_m^B \tag{36}$$

Eliminating $\boldsymbol{\lambda}_{\gamma^A m}$ from Eqs. (21) and (36), we obtain:

$$\begin{aligned}&(1-\gamma^A)\mathbb{C}^B\mathbb{M}^B\boldsymbol{z}_0^B + \gamma^A\mathbb{C}^B\mathbb{M}^B\boldsymbol{z}_m^B - \mathbb{C}^A\mathbb{M}^A\boldsymbol{z}_{\gamma^A m}^A \\ &\quad = \boldsymbol{C}^B\left((1-\gamma^A)\boldsymbol{f}_0^B + \gamma^A\boldsymbol{f}_m^B\right) - \boldsymbol{C}^A\boldsymbol{f}_{\gamma^A m}^A\end{aligned} \tag{37}$$

where $\mathbb{C}^B\mathbb{M}^B = \boldsymbol{C}^B\left[\boldsymbol{M}^B, \boldsymbol{D}^B, \boldsymbol{K}^B\right]$. Eq. (37) effectively replaces Eq. (35) in the final set of equations to be solved for the proposed MTS method. Next, we describe the bordered solution process for solving Eqs. (21), (22), (31)–(33) and (37) together.

3.2 Bordered solution procedure

Eqs. (21), (22), (31)–(33) and (37) form a linear system of equations that is solved to advance subdomains Ω^A and Ω^B by one block time-step from the initial time-instant t_0 to the final time-instant t_m while maintaining continuity of the solution across the interface between them. This

system of equations is solved in a decoupled time-stepping manner for both subdomains Ω^A and Ω^B using a bordered procedure (Prakash et al., 2014) by expressing them in the form of a saddle-point problem (Benzi et al., 2005):

$$\begin{bmatrix} \mathrm{M} & \mathrm{C}^{\mathrm{T}} \\ \mathrm{B} & 0 \end{bmatrix} \begin{bmatrix} \mathrm{z} \\ \lambda \end{bmatrix} = \begin{bmatrix} \mathrm{r} \\ \mathrm{s} \end{bmatrix} \tag{38}$$

where,

$$\mathrm{M} = \left[\begin{array}{ccc|c} \mathbb{M}_1^B & & & \\ \mathbb{N}_2^B & \mathbb{M}_2^B & & \\ & \ddots & \ddots & \\ & \mathbb{N}_1^B & \mathbb{M}_1^B & \\ & \mathbb{O}_2^B & \mathbb{N}_2^B \; \mathbb{M}_2^B & \\ \hline & & & \mathbb{M}_1^A \\ & & & \mathbb{N}_2^A \; \mathbb{M}_2^A \end{array}\right]; \quad \mathrm{z} = \left[\begin{array}{c} \boldsymbol{z}_{\gamma^B}^B \\ \boldsymbol{z}_1^B \\ \vdots \\ \boldsymbol{z}_{m-1+\gamma^B}^B \\ \boldsymbol{z}_m^B \\ \hline \boldsymbol{z}_{\gamma^A m}^A \\ \boldsymbol{z}_m^A \end{array}\right]; \tag{39}$$

$$\mathrm{C}^{\mathrm{T}} = \left[\begin{array}{cc} c_{1,\gamma^B}\mathbb{C}^{B^T} & c_{2,\gamma^B}\mathbb{C}^{B^T} \\ c_{1,1}\mathbb{C}^{B^T} & c_{2,1}\mathbb{C}^{B^T} \\ \vdots & \\ c_{1,m-1+\gamma^B}\mathbb{C}^{B^T} & c_{2,m-1+\gamma^B}\mathbb{C}^{B^T} \\ c_{1,m}\mathbb{C}^{B^T} & c_{2,m}\mathbb{C}^{B^T} \\ \hline \mathbb{C}^{A^T} & 0 \\ 0 & \mathbb{C}^{A^T} \end{array}\right]; \quad \mathrm{r} = \left[\begin{array}{c} \boldsymbol{r}_{\gamma^B}^B - \mathbb{N}_1^B \boldsymbol{z}_0^B - \mathbb{C}^{B^T}\tilde{\boldsymbol{\lambda}}_{\gamma^B} \\ \boldsymbol{r}_1^B - \mathbb{O}_2^B \boldsymbol{z}_0^B - \mathbb{C}^{B^T}\tilde{\boldsymbol{\lambda}}_1 \\ \vdots \\ \boldsymbol{r}_{m-1+\gamma^B}^B - \mathbb{C}^{B^T}\tilde{\boldsymbol{\lambda}}_{m-1+\gamma^B} \\ \boldsymbol{r}_m^B - \mathbb{C}^{B^T}\tilde{\boldsymbol{\lambda}}_m \\ \hline \boldsymbol{r}_{\gamma^A m}^A - \mathbb{N}_1^A \boldsymbol{z}_0^A \\ \boldsymbol{r}_m^A - \mathbb{O}_2^A \boldsymbol{z}_0^A \end{array}\right]; \tag{40}$$

$$\mathrm{B} = \left[\begin{array}{cc|cc} 0\,0\cdots 0\,\boldsymbol{\gamma}^A\mathbb{C}^B\mathbb{M}^B & & -\mathbb{C}^A\mathbb{M}^A & 0 \\ 0\,0\cdots 0 \quad \mathbb{B}^B & & 0 & \mathbb{B}^A \end{array}\right]; \quad \lambda = \begin{bmatrix} \boldsymbol{\lambda}_{\gamma^A m} \\ \boldsymbol{\lambda}_m \end{bmatrix}; \tag{41}$$

$$\mathrm{s} = \begin{bmatrix} \boldsymbol{C}^B\left((1-\boldsymbol{\gamma}^A)\boldsymbol{f}_0^B + \boldsymbol{\gamma}^A\boldsymbol{f}_m^B\right) - \boldsymbol{C}^A\boldsymbol{f}^A_{\gamma^A m} - (1-\boldsymbol{\gamma}^A)\mathbb{C}^B\mathbb{M}^B\boldsymbol{z}_0^B \\ 0 \end{bmatrix} \tag{42}$$

Note that when $\boldsymbol{\gamma}^A = \boldsymbol{\gamma}^B = 1$, the above equations are identical to the MTS-Newmark method for the trapezoidal rule (MTS-TR method).

As bordered systems can be solved using the Schur complement method, the sub-matrix z is represented as

$$\mathrm{z} = \overline{\mathrm{z}} + \mathrm{z}' \tag{43}$$

where $\overline{\mathrm{z}}$ is the uncoupled-free part of the solution and z' represents the coupled-link correction. These quantities can be solved from Eq. (38) as:

$$\overline{\mathrm{z}} = \mathrm{M}^{-1}\mathrm{r} \tag{44}$$

$$\mathrm{z}' = -\mathrm{Y}\lambda \tag{45}$$

$$\mathrm{Y} = \mathrm{M}^{-1}\mathrm{C}^{\mathrm{T}} \tag{46}$$

$$\mathrm{B}\mathrm{M}^{-1}\mathrm{C}^{\mathrm{T}}\lambda = \mathrm{B}\mathrm{M}^{-1}\mathrm{r} - \mathrm{s} \tag{47}$$

Using the uncoupled-free part $\overline{\mathrm{z}}$ and coupled-link correction z', the solution is updated at each block time-step and we repeat this process for the next block time-step ΔT, as represented in Fig. 5. In Algorithm 1, we summarize this procedure for the MTS-Bathe method for the ρ_∞-Bathe scheme in linear dynamics. Following the approach described in Prakash et al. (2014), the proposed MTS-Bathe can also extended to solve non-linear problems.

3.3 Computation of initial accelerations

Before the proposed MTS-Bathe method can be used, we need to compute initial accelerations in subdomains Ω^A and Ω^B when initial displacements and velocities are given. To do so, first the uncoupled initial accelerations are obtained as:

$$\begin{aligned} \overline{\boldsymbol{a}}_0^A &= [\boldsymbol{M}^A]^{-1}(\boldsymbol{f}_0^A - \boldsymbol{D}^A\boldsymbol{v}_0^A - \boldsymbol{K}^A\boldsymbol{d}_0^A) \\ \overline{\boldsymbol{a}}_0^B &= [\boldsymbol{M}^B]^{-1}(\boldsymbol{f}_0^B - \boldsymbol{D}^B\boldsymbol{v}_0^B - \boldsymbol{K}^B\boldsymbol{d}_0^B) \end{aligned} \tag{48}$$

Next the Lagrange multipliers necessary to enforce continuity of the initial accelerations are computed:

$$\boldsymbol{\lambda}_0 = \left(\boldsymbol{C}^A[\boldsymbol{M}^A]^{-1}\boldsymbol{C}^{A^T} + \boldsymbol{C}^B[\boldsymbol{M}^B]^{-1}\boldsymbol{C}^{B^T}\right)^{-1}\left(\boldsymbol{C}^A\overline{\boldsymbol{a}}_0^A + \boldsymbol{C}^B\overline{\boldsymbol{a}}_0^B\right) \tag{49}$$

Lastly, the initial accelerations are updated as follows:

$$\begin{aligned} \boldsymbol{a}_0'^A &= -[\boldsymbol{M}^A]^{-1}\boldsymbol{C}^{A^T}\boldsymbol{\lambda}_0, \quad \boldsymbol{a}_0'^B = -[\boldsymbol{M}^B]^{-1}\boldsymbol{C}^{B^T}\boldsymbol{\lambda}_0 \\ \boldsymbol{a}_0^A &= \overline{\boldsymbol{a}}_0^A + \boldsymbol{a}_0'^A, \quad \boldsymbol{a}_0^B = \overline{\boldsymbol{a}}_0^B + \boldsymbol{a}_0'^B \end{aligned} \tag{50}$$

Once the initial accelerations have been computed, the MTS-Bathe method can proceed.

Algorithm 1: Bordered solution procedure for the MTS-Bathe method in linear dynamics.

A. Initial calculation

1. Decompose problem domain into Ω^A and Ω^B, and select time-step size Δt and ΔT (here $\Delta T = m\Delta t$, m is natural number) and parameters ρ_∞^A, γ^A, ρ_∞^B, γ^B.
2. Construct mass matrices $\boldsymbol{M}^A$, $\boldsymbol{M}^B$, stiffness matrices $\boldsymbol{K}^A$, $\boldsymbol{K}^B$, damping matrices $\boldsymbol{D}^A$, $\boldsymbol{D}^B$, connectivity matrices $\boldsymbol{C}^A$, $\boldsymbol{C}^B$, and force vectors $\boldsymbol{f}^A$, $\boldsymbol{f}^B$, and initialize displacements $\boldsymbol{d}_0^A$, $\boldsymbol{d}_0^B$ and velocities $\boldsymbol{v}_0^A$, $\boldsymbol{v}_0^B$.
3. Compute initial accelerations $\boldsymbol{a}_0^A$, $\boldsymbol{a}_0^B$ from Eqs. (48)–(50)
4. Compute the interface matrix Y: $\mathrm{Y} = \mathrm{M}^{-1}\mathrm{C}^{\mathrm{T}}$ from Eq. (46)

B. For each cycle of the block time-step $\Delta T(= m\Delta t)$

1. Compute the uncoupled-free part $\overline{\mathrm{z}}$: $\overline{\mathrm{z}} = \mathrm{M}^{-1}\mathrm{r}$ from Eq. (44)
2. Compute the Lagrange multipliers λ: $\lambda = [\mathrm{BY}]^{-1}(\mathrm{Bz} - \mathrm{s})$ from Eq. (47)
3. Compute the coupled-link correction z': $\mathrm{z}' = -\mathrm{Y}\lambda$ from Eq. (45)
4. Update the solutions: $\mathrm{z} = \overline{\mathrm{z}} + \mathrm{z}'$ from Eq. (43)

4. STABILITY ANALYSIS

In this section, we first evaluate the stability of the proposed MTS-Bathe method with different continuity constraints presented in Section 3.1. Next, we identify the specific constraint condition that leads to unconditional stability and theoretically prove this property for coupling any ρ_∞-Bathe scheme with any time-step ratio.

4.1 Evaluation of Spectral stability

Stability characteristics are evaluated using a spectral analysis for a split SDOF problem, as presented in Prakash and Hjelmstad (2004); Prakash et al. (2014). In this problem, a SDOF system given by:

$$Ma_{n+1} + Dv_{n+1} + Kd_{n+1} = f_{n+1} \tag{51}$$

is decomposed into two SDOF systems, A and B:

$$\begin{aligned} &M^A a^A_{n+1} + D^A v^A_{n+1} + K^A d^A_{n+1} + \lambda_{n+1} = f^A_{n+1} \\ &M^B a^B_{n+1} + D^B v^B_{n+1} + K^B d^B_{n+1} - \lambda_{n+1} = f^B_{n+1} \\ &w^A_{n+1} - w^B_{n+1} = 0 \end{aligned} \tag{52}$$

that are coupled together with the Lagrange multiplier λ to enforce the continuity of a kinematic quantity w, which may be displacement, velocity or accelerations. The initial conditions of the split SDOF system are inherited from the underlying undecomposed SDOF system:

$$\begin{aligned} d(0) = d^A(0) = d^B(0) = d_0 \\ v(0) = v^A(0) = v^B(0) = v_0 \end{aligned} \tag{53}$$

Without loss of generality, we consider $M^A = M^B = 1$, $D^A = 2\zeta^A\omega_0^A$, $D^B = 2\zeta^B\omega_0^B$, $K^A = (\omega_0^A)^2$, and $K^B = (\omega_0^B)^2$, where ω_0, and ζ denote the natural frequency and damping ratio,

respectively. Note that for the underlying undecomposed SDOF problem, the natural frequency ω_0 and the corresponding natural period are given as:

$$\omega_0 = \sqrt{\frac{(\omega_0^A)^2 + (\omega_0^B)^2}{1+1}} \quad ; \quad T_0 = 2\pi/\omega_0 \tag{54}$$

To facilitate spectral analysis, the proposed MTS-Bathe method is written in a recursive form:

$$\begin{bmatrix} \boldsymbol{z}_{n+m}^A \\ \boldsymbol{z}_{n+m}^B \end{bmatrix} = \boldsymbol{A} \begin{bmatrix} \boldsymbol{z}_n^A \\ \boldsymbol{z}_n^B \end{bmatrix} + \boldsymbol{L}_n \tag{55}$$

where the matrix $\boldsymbol{A}$ and vector $\boldsymbol{L}_n$ are the amplification matrix and the load vector, respectively. The procedure to obtain the amplification matrix $\boldsymbol{A}$ is described in Appendix A. Note that the matrix $\boldsymbol{A}$ depends on the time-step ratio, m, and Bathe parameters, ρ_∞^A, ρ_∞^B, γ^A and γ^B. For stability, the spectral radius of the amplification matrix should be less than or equal to 1. The spectral radius of $\boldsymbol{A}$ is defined as:

$$\rho(\boldsymbol{A}) = \max_i(|\mu_i|) \tag{56}$$

where $\mu_i (i = 1, 2, ..., 6)$ are roots of $p(\mu) = 0$, where $p(\mu)$ is the characteristic polynomial of $\boldsymbol{A}$.

The spectral radius of the MTS-Bathe method is computed for the three cases of constraint conditions given in Section 3.1 for numerous combinations of the Bathe parameters ρ_∞ and γ. Fig. 6 shows a representative result for $\rho_\infty^A = \rho_\infty^B = 0$ (i.e. the γ-Bathe scheme) when $\omega_0^B/\omega_0^A = 1$ and $\zeta^A = \zeta^B = 0$ (i.e. no damping). It is found that case 2 (continuity of velocities) exhibits unconditionally stable behavior and thus we focus on this constraint condition henceforth.

4.2 Energy method of stability analysis for the proposed MTS-Bathe method

In this section, we prove that the proposed MTS-Bathe method with continuity of velocities at the block time-step and linear interpolation of Lagrange multipliers is unconditionally stable for

any value of the time-step ratio, m. For MTS methods, the total energy balance equation (in the absence of external forces) for both subdomains is written as:

$$\Delta KE_m^A + \Delta PE_m^A + \sum_{j=1}^{m} \left\{ \Delta KE_j^B + \Delta PE_j^A \right\} = -D_m^A - \sum_{j=1}^{m} D_j^B + E_{link} \tag{57}$$

where E_{link} is the work done by the Lagrange multipliers. Note that since the underlying UTS-Bathe schemes for subdomains Ω^A and Ω^B are stable, the stability of the proposed MTS-Bathe method only depends on E_{link}.

It is known that Lagrange multipliers manifest as forces on the interface acting equal and opposite on subdomains Ω^A and Ω^B as shown in Fig. 1 (see Farhat and Roux (1991); Prakash and Hjelmstad (2004)). Consequently, E_{link} can be obtained from the definition of E_{ext} in Eq. (13) by replacing r with the effect of Lagrange multipliers on the two subdomains, as follows:

$$\begin{aligned} E_{link} =& E_{ext,m}^A \left[\Delta \boldsymbol{a}_m^A, \Delta \boldsymbol{v}_m^A, -\boldsymbol{C}^{A^T} \Delta \boldsymbol{\lambda}_m, -\boldsymbol{C}^{A^T} \Delta_\gamma \boldsymbol{\lambda}_m \right] \\ &+ \sum_{j=1}^{m} E_{ext,j}^B \left[\Delta \boldsymbol{a}_j^B, \Delta \boldsymbol{v}_j^B, -\boldsymbol{C}^{B^T} \Delta \boldsymbol{\lambda}_j, -\boldsymbol{C}^{B^T} \Delta_\gamma \boldsymbol{\lambda}_j \right] \end{aligned} \tag{58}$$

where $\Delta(\cdot)_m = (\cdot)_m - (\cdot)_0$ and $\Delta_\gamma(\cdot)_m = (\cdot)_{\gamma^A m} - (\cdot)_0$ for subdomain Ω^A, and $\Delta(\cdot)_j = (\cdot)_j - (\cdot)_{j-1}$ and $\Delta_\gamma(\cdot)_j = (\cdot)_{j-1+\gamma^B} - (\cdot)_{j-1}$ for subdomain Ω^B. Eq. (58) can be simplified to:

$$\begin{aligned} E_{link} = & -\frac{1}{\Delta T} \left(\boldsymbol{C}^A \Delta \boldsymbol{v}_m^A \right)^T \left(\boldsymbol{\lambda}_m - \boldsymbol{\lambda}_0 \right) - \sum_{j=1}^{m} \left[\frac{1}{\Delta t} \left(\boldsymbol{C}^B \Delta \boldsymbol{v}_j^B \right)^T \left(\boldsymbol{\lambda}_j - \boldsymbol{\lambda}_{j-1} \right) \right] \\ & - \left(\boldsymbol{C}^A \boldsymbol{\eta}_\rho^A \right)^T \left(\gamma^A \boldsymbol{\lambda}_m - \boldsymbol{\lambda}_{\gamma^A m} + (1-\gamma^A) \boldsymbol{\lambda}_0 \right) \\ & - \sum_{j=1}^{m} \left[\left(\boldsymbol{C}^B \boldsymbol{\eta}_\rho^B \right)^T \left(\gamma^B \boldsymbol{\lambda}_j - \boldsymbol{\lambda}_{j-1+\gamma^B} + (1-\gamma^B) \boldsymbol{\lambda}_{j-1} \right) \right] \end{aligned} \tag{59}$$

where

$$\boldsymbol{\eta}_{\rho}^{A} = (1+\rho_{\infty}^{A})\left(\left(\sigma_{1}^{A}\right)^{2}\boldsymbol{M}^{A} + \left(\sigma_{2}^{A}\right)^{2}\boldsymbol{K}^{A}\right)^{-1}\left(\sigma_{1}^{A}\boldsymbol{M}^{A}\Delta\boldsymbol{a}_{m}^{A} + \sigma_{2}^{A}\boldsymbol{K}^{A}\Delta\boldsymbol{v}_{m}^{A}\right) \tag{60}$$

$$\boldsymbol{\eta}_{\rho}^{B} = (1+\rho_{\infty}^{B})\left(\left(\sigma_{1}^{B}\right)^{2}\boldsymbol{M}^{B} + \left(\sigma_{2}^{B}\right)^{2}\boldsymbol{K}^{B}\right)^{-1}\left(\sigma_{1}^{B}\boldsymbol{M}^{B}\Delta\boldsymbol{a}_{j}^{A} + \sigma_{2}^{A}\boldsymbol{K}^{B}\Delta\boldsymbol{v}_{j}^{B}\right) \tag{61}$$

with $\sigma_1^A = 2(2-\gamma^A(1-\rho_\infty^A))$, $\sigma_2^A = (1-\rho_\infty^A)\gamma^A(1-\gamma^A)\Delta T$, $\sigma_1^B = 2(2-\gamma^B(1-\rho_\infty^B))$, and $\sigma_2^B = (1-\rho_\infty^B)\gamma^B(1-\gamma^B)\Delta t$. From Eqs. (29) and (35), E_{link} can be further reduced as follows:

$$\begin{aligned} E_{link} &= -\left\{\frac{1}{\Delta T}\boldsymbol{C}^{A}\Delta\boldsymbol{v}_{m}^{A} + \sum_{j=1}^{m}\frac{1}{m\Delta t}\boldsymbol{C}^{B}\Delta\boldsymbol{v}_{j}^{B}\right\}(\boldsymbol{\lambda}_{m}-\boldsymbol{\lambda}_{0}) \\ &= -\frac{1}{\Delta T}\left\{\boldsymbol{C}^{A}\Delta\boldsymbol{v}_{m}^{A} + \boldsymbol{C}^{B}\sum_{j=1}^{m}\Delta\boldsymbol{v}_{j}^{B}\right\}(\boldsymbol{\lambda}_{m}-\boldsymbol{\lambda}_{0}) \\ &= -\frac{1}{\Delta T}\left\{\boldsymbol{C}^{A}\left(\boldsymbol{v}_{m}^{A}-\boldsymbol{v}_{0}^{A}\right) + \boldsymbol{C}^{B}\left(\boldsymbol{v}_{m}^{B}-\boldsymbol{v}_{0}^{B}\right)\right\}(\boldsymbol{\lambda}_{m}-\boldsymbol{\lambda}_{0}) \\ &= 0 \end{aligned} \tag{62}$$

The result above shows that continuity of velocities ($\boldsymbol{C}^A\boldsymbol{v}_m^A + \boldsymbol{C}^B\boldsymbol{v}_m^B = 0$) leads to $E_{link} = 0$. Thus, the proposed MTS-Bathe method does not add or remove energy at the interface and leads to an unconditionally stable method.

5. ACCURACY ANALYSIS

In this section we evaluate the accuracy of the proposed MTS-Bathe method by first conducting a truncation error analysis and then studying its characteristics of period elongation and amplitude decay.

5.1 Truncation error analysis

In this section, we compute the local truncation errors (LTEs) in the solution obtained by the proposed MTS-Bathe method by advancing from t_n to t_{n+m}. Without loss of generality, these

can be taken as 0 and $t_{n+m} = \Delta T$ respectively. First, we define the following LTEs in kinematic quantities and Lagrange multipliers:

$$\begin{aligned}
&\boldsymbol{\tau}^A_{\boldsymbol{z}_{\gamma^A m}} = \boldsymbol{z}^A_{\gamma^A m} - \boldsymbol{z}^A(t_{\gamma^A m}); \quad \boldsymbol{\tau}^A_{\boldsymbol{z}_m} = \boldsymbol{z}^A_m - \boldsymbol{z}^A(t_m);\\
&\boldsymbol{\tau}^B_{\boldsymbol{z}_{j+\gamma^B}} = \boldsymbol{z}^B_{j+\gamma^B} - \boldsymbol{z}^B(t_{j+\gamma^B}); \quad \boldsymbol{\tau}^B_{\boldsymbol{z}_{j+1}} = \boldsymbol{z}^B_{j+1} - \boldsymbol{z}^B(t_{j+1});\\
&\boldsymbol{\tau}_{\boldsymbol{\lambda}_{\gamma^A m}} = \boldsymbol{\lambda}_{\gamma^A m} - \boldsymbol{\lambda}(t_{\gamma^A m}); \quad \boldsymbol{\tau}_{\boldsymbol{\lambda}_m} = \boldsymbol{\lambda}_m - \boldsymbol{\lambda}(t_m)
\end{aligned} \tag{63}$$

where $\boldsymbol{z}^A(t_{\gamma^A m})$, $\boldsymbol{z}^A(t_m)$, $\boldsymbol{z}^B(t_{j+\gamma^B})$, $\boldsymbol{z}^B(t_{j+1})$, $\boldsymbol{\lambda}(t_{\gamma^A m})$, and $\boldsymbol{\lambda}(t_m)$ represent the exact values of these quantities at the noted time-instants. Note that the initial values of these quantities are assumed to be exact i.e. $\boldsymbol{z}^A(0) = \boldsymbol{z}^A_0$, $\boldsymbol{z}^B(0) = \boldsymbol{z}^B_0$, and $\boldsymbol{\lambda}(0) = \boldsymbol{\lambda}_0$. The exact values of these quantities at later instants of time are obtained using a Taylor series expansion about $t = 0$:

$$\boldsymbol{z}(t_m) = \sum_{k=0}^{\infty} \frac{\Delta T^k}{k!} \frac{d^k \boldsymbol{z}}{dt^k} \tag{64}$$

Using the definitions above and Eqs. (21), (22), (31), (32), (33) and (35), the following equations can be obtained:

$$\mathbb{M}^A_1 \boldsymbol{\tau}^A_{\boldsymbol{z}_{\gamma^A m}} + \gamma^A \mathbb{C}^{A^T} \boldsymbol{\tau}_{\boldsymbol{\lambda}_m} = \boldsymbol{g}^A_{\gamma^A m} \tag{65}$$

$$\mathbb{M}^A_2 \boldsymbol{\tau}^A_{\boldsymbol{z}_m} + \mathbb{C}^{A^T} \boldsymbol{\tau}_{\boldsymbol{\lambda}_m} = \boldsymbol{g}^A_m - \mathbb{N}^A_2 \boldsymbol{\tau}^A_{\boldsymbol{z}_{\gamma^A m}} \tag{66}$$

$$\mathbb{M}^B_1 \boldsymbol{\tau}^B_{\boldsymbol{z}_{j+\gamma^B}} + \frac{j+\gamma^B}{m} \mathbb{C}^{B^T} \boldsymbol{\tau}^B_{\boldsymbol{\lambda}_m} = \boldsymbol{g}^B_{j+\gamma^B} - \mathbb{N}^B_1 \boldsymbol{\tau}^B_{\boldsymbol{z}_j} \tag{67}$$

$$\mathbb{M}^B_2 \boldsymbol{\tau}^B_{\boldsymbol{z}^B_{j+1}} + \frac{j+1}{m} \mathbb{C}^{B^T} \boldsymbol{\tau}^B_{\boldsymbol{\lambda}_m} = \boldsymbol{g}^B_{j+1} - \mathbb{N}^B_2 \boldsymbol{\tau}^B_{\boldsymbol{z}^B_{j+\gamma^B}} - \mathbb{O}^B_2 \boldsymbol{\tau}^B_{\boldsymbol{z}^A_j} \tag{68}$$

$$\mathbb{B}^A \boldsymbol{\tau}^A_{\boldsymbol{z}_m} + \mathbb{B}^B \boldsymbol{\tau}^B_{\boldsymbol{z}_m} = 0 \tag{69}$$

where

$$
\begin{aligned}
\boldsymbol{g}^A_{\gamma^A m} &= \begin{bmatrix} -\boldsymbol{C}^{A^T}\boldsymbol{g}_{\lambda_{\gamma^A m}} \\ \frac{(\gamma^A\Delta T)^3}{12}\ddot{\boldsymbol{a}}^A_0 + O(\Delta T^4) \\ \frac{(\gamma^A\Delta T)^3}{12}\dot{\boldsymbol{a}}^A_0 + O(\Delta T^4) \end{bmatrix}; \quad \boldsymbol{g}^A_m = \begin{bmatrix} 0 \\ \frac{(3s_1^A(\gamma^A)^2+3s_2^A-1)\Delta T^3}{6}\ddot{\boldsymbol{a}}^A_0 + O(\Delta T^4) \\ \frac{(3q_1^A(\gamma^A)^2+3q_2^A-1)\Delta T^3}{6}\dot{\boldsymbol{a}}^A_0 + O(\Delta T^4) \end{bmatrix}; \\
\boldsymbol{g}^B_{j+\gamma^B} &= \begin{bmatrix} -\boldsymbol{C}^{B^T}\boldsymbol{g}_{\lambda_{j+\gamma^B}} \\ \frac{(\gamma^B\Delta t)^3}{12}\ddot{\boldsymbol{a}}^B_0 + O(\Delta t^4) \\ \frac{(\gamma^B\Delta t)^3}{12}\dot{\boldsymbol{a}}^B_0 + O(\Delta t^4) \end{bmatrix}; \quad \boldsymbol{g}^B_{j+1} = \begin{bmatrix} -\boldsymbol{C}^{B^T}\boldsymbol{g}_{\lambda_{j+1}} \\ \frac{(3s_1^B(\gamma^B)^2+3s_2^B-1)\Delta t^3}{6}\ddot{\boldsymbol{a}}^B_0 + O(\Delta t^4) \\ \frac{(3q_1^B(\gamma^B)^2+3q_2^B-1)\Delta t^3}{6}\dot{\boldsymbol{a}}^B_0 + O(\Delta t^4) \end{bmatrix}; \qquad (70) \\
\boldsymbol{g}_{\lambda_{\gamma^A m}} &= \tfrac{\gamma^A(1-\gamma^A)\Delta T^2}{2}\ddot{\boldsymbol{\lambda}}_0 + \tfrac{\gamma^A(1-(\gamma^A)^2)\Delta T^3}{6}\dddot{\boldsymbol{\lambda}}_0 + O(\Delta T^4); \\
\boldsymbol{g}_{\lambda_{j+\gamma^B}} &= \tfrac{(j+\gamma^B)(m-(j+\gamma^B))\Delta t^2}{2}\ddot{\boldsymbol{\lambda}}_0 + \tfrac{(j+\gamma^B)(m^2-(j+\gamma^B)^2)\Delta T^3}{6}\dddot{\boldsymbol{\lambda}}_0 + O(\Delta T^4); \\
\boldsymbol{g}_{\lambda_{j+1}} &= \tfrac{(j+1)(m-(j+1))\Delta t^2}{2}\ddot{\boldsymbol{\lambda}}_0 + \tfrac{(j+1)(m^2-(j+1)^2)\Delta t^3}{6}\dddot{\boldsymbol{\lambda}}_0 + O(\Delta T^4)
\end{aligned}
$$

where the overdot denotes time derivative, and $\dot{\boldsymbol{a}}^A_0$, $\ddot{\boldsymbol{a}}^A_0$, $\dot{\boldsymbol{a}}^B_0$, $\ddot{\boldsymbol{a}}^B_0$, $\ddot{\boldsymbol{\lambda}}_0$, and $\dddot{\boldsymbol{\lambda}}_0$ are the exact time derivatives of these quantities at $t = 0$. Note that in Eq. (70), we consider linear, quadratic, and cubic terms in the Taylor series. Similar to Section 3.2, this system can be expressed in the form of a saddle-point problem and solved using a bordered procedure. Consequently, we will compute the LTEs defined in Eq. (63) as a sum of uncoupled-free and coupled-link parts:

$$\boldsymbol{\tau}_{\mathrm{z}_m} = \boldsymbol{\tau}_{\bar{\mathrm{z}}_m} + \boldsymbol{\tau}_{\mathrm{z}'_m} \qquad (71)$$

To keep the LTE analysis tractable, and without loss of generality, we compute LTEs for a split SDOF system given by Eq. (52). Solving Eqs. (65)-(69) as a bordered system, we find that the uncoupled-free LTEs in subdomains Ω^A and Ω^B, respectively, as:

$$\boldsymbol{\tau}^A_{\bar{\boldsymbol{z}}_m} \propto O(\Delta T^3), \quad \boldsymbol{\tau}^B_{\bar{\boldsymbol{z}}_m} \propto O(\Delta T^3) \qquad (72)$$

This is consistent with the fact that the underlying UTS-Bathe schemes are at least second-order

accurate. Next, to compute the coupled-link part of the LTEs, we first compute the LTE in matrix Y for the bordered solve using Eq. (46) as:

$$\boldsymbol{Y}^A_{\boldsymbol{\tau}_m} \propto \begin{bmatrix} 1+O(\Delta T) \\ O(\Delta T) \\ O(\Delta T^2) \end{bmatrix}; \quad \boldsymbol{Y}^B_{\boldsymbol{\tau}_m} \propto \begin{bmatrix} -1+O(\Delta T) \\ O(\Delta T) \\ O(\Delta T^2) \end{bmatrix} \tag{73}$$

Thus, the LTE in the Lagrange multiplier is obtained as:

$$\tau_{\lambda_m} = \frac{\tau^A_{\bar{v}_m} - \tau^B_{\bar{v}_m}}{Y^A_{\tau_{v_m}} - Y^B_{\tau_{v_m}}} \propto O(\Delta T^2) \tag{74}$$

Finally, combining Eqs. (72)–(74), LTEs in the kinematic quantities are obtained as:

$$\begin{aligned}
\tau^A_{a_m} \propto \tau^B_{a_m} &\propto \underbrace{O(\Delta T^3)}_{\text{uncoupled-free}} - \underbrace{O(\Delta T^2)\cdot 1}_{\text{coupled-link}} \propto O(\Delta T^2); \\
\tau^A_{v_m} = \tau^B_{v_m} &\propto \underbrace{O(\Delta T^3)}_{\text{uncoupled-free}} - \underbrace{O(\Delta T^2)\cdot O(\Delta T)}_{\text{coupled-link}} \propto O(\Delta T^3); \\
\tau^A_{d_m} \propto \tau^B_{d_m} &\propto \underbrace{O(\Delta T^3)}_{\text{uncoupled-free}} - \underbrace{O(\Delta T^2)\cdot O(\Delta T^2)}_{\text{coupled-link}} \propto O(\Delta T^3)
\end{aligned} \tag{75}$$

Since the lowest order of LTE among τ_{λ_m}, τ_{a_m}, τ_{v_m}, and τ_{d_m} is $O(\Delta T^2)$, the overall rate of convergence of the proposed MTS-Bathe method is one. We also point out that, despite this result for the LTEs, global errors in all of the above quantities are found to be second-order accurate in numerical examples (see Section 6).

In the special case, when $\gamma^A = \gamma^A_p$ and $\gamma^B = \gamma^B_p$ i.e. using third-order accurate UTS-Bathe

schemes for the underlying subdomains, the following expressions for LTEs are found:

$$\begin{aligned}
&\boldsymbol{\tau}^A_{\bar{\boldsymbol{z}}_m} \propto \begin{bmatrix} \frac{\Delta T^3}{6}\zeta^A\omega_0^A\ddot{\lambda}_0 + O(\Delta T^4) \\ -\frac{\Delta T^3}{12}\ddot{\lambda}_0 + O(\Delta T^4) \\ O(\Delta T^4) \end{bmatrix}; \quad \boldsymbol{\tau}^B_{\bar{\boldsymbol{z}}_m} \propto \begin{bmatrix} -\frac{\Delta T^3}{6}\zeta^B\omega_0^B\ddot{\lambda}_0 + O(\Delta T^4) \\ \frac{\Delta T^3}{12}\ddot{\lambda}_0 + O(\Delta T^4) \\ O(\Delta T^4) \end{bmatrix}; \\
&\boldsymbol{Y}^A_{\boldsymbol{\tau}_m} \propto \begin{bmatrix} 1 - \zeta^A\omega_0^A\Delta T + O(\Delta T^) \\ 0.5\Delta T + O(\Delta T^2) \\ \frac{1}{6}\Delta T^2 + O(\Delta T^3) \end{bmatrix}; \quad \boldsymbol{Y}^B_{\boldsymbol{\tau}_m} \propto \begin{bmatrix} -1 + \zeta^B\omega_0^B\Delta T + O(\Delta T^2) \\ -0.5\Delta T + O(\Delta T^2) \\ -\frac{1}{6}\Delta T^2 + O(\Delta T^3) \end{bmatrix}; \\
&\tau_\lambda \propto -\tfrac{1}{6}\Delta T^2\ddot{\lambda}_0 + O(\Delta T^3)
\end{aligned} \tag{76}$$

Combining these expressions as before, LTEs in the kinematic quantities are found to be:

$$\begin{aligned}
\tau^A_{a_m} \propto \tau^B_{a_m} &\propto \underbrace{O(\Delta T^3)}_{\text{uncoupled-free}} - \underbrace{O(\Delta T^2)\cdot 1}_{\text{coupled-link}} = O(\Delta T^2); \\
\tau^A_{v_m} = \tau^B_{v_m} &\propto \underbrace{O(\Delta T^3)}_{\text{uncoupled-free}} - \underbrace{O(\Delta T^2)\cdot O(\Delta T)}_{\text{coupled-link}} \propto O(\Delta T^4); \\
\tau^A_{d_m} \propto \tau^B_{d_m} &\propto \underbrace{O(\Delta T^4)}_{\text{uncoupled-free}} - \underbrace{O(\Delta T^2)\cdot O(\Delta T^2)}_{\text{coupled-link}} \propto O(\Delta T^4)
\end{aligned} \tag{77}$$

It is found that the cubic terms in the LTE for velocities from uncoupled-free and coupled-link parts cancel each other out, leading to an overall LTE of the order of ΔT^4. Note, again, that the LTE in accelerations and Lagrange multipliers are still of the order of ΔT^2 and thus the overall rate of convergence is still one. This is likely a consequence of the linear interpolation of Lagrange multipliers used in the formulation of the proposed MTS-Bathe method.

To verify the theoretical LTEs found above, we compute LTEs for the split SDOF problem by solving it using the proposed MTS-Bathe method for a single time-step and with the following parametric choices: $d_0 = v_0 = 1$, $\omega_0 = 2\pi$, $\zeta^A = 0.2$, and $\zeta^B = 0.1$ for various values of time-step ratio, m, and frequency ratios, ω_0^B/ω_0^A. Note that the exact solution for the split SDOF problem can be readily computed by solving the underlying undecomposed SDOF and thus the

LTEs computed in this way are exact for the specific parameters chosen.

Fig. 7 shows that for $\gamma^A = \gamma^B = 2 - \sqrt{2}$ (i.e. using the γ-Bathe scheme for both subdomains), the convergence rate in LTEs for displacements and velocities for both subdomains is of order 3, whereas that for accelerations and Lagrange multipliers is 2. Similarly, Fig. 8, shows that for the ρ_∞-Bathe scheme with $\gamma^A = \gamma_p^A$ and $\gamma^B = \gamma_p^B$ (i.e. using third-order accurate UTS-Bathe scheme for both subdomains) leads to fourth-order LTE in displacements and velocities, and second-order LTE in accelerations and Lagrange multipliers.

5.2 Period elongation and amplitude decay

In this section, we analyze accuracy characteristics for the proposed MTS-Bathe method and compare them to the MTS-TR method (Prakash and Hjelmstad, 2004). For this analysis, a split SDOF problem defined in Eq. (52) is solved with the following choice of problem parameters:

$$\begin{aligned} &M^A = M^B = 1, \quad D^A = D^B = 0, \quad K^A = (\omega_0^A)^2, \quad K^B = (\omega^B)^2, \\ &f^A(t) = f^B(t) = 0, \quad d_0 = 0, \quad \text{and} \quad v_0 = 1 \end{aligned} \tag{78}$$

The natural frequency and period of the undecomposed system are given by Eq. (54). The exact solution for the split SDOF problems is given as: $v^A(t) = v^B(t) = \cos(\omega_0 t)$. For accuracy analysis, the effect of damping ratio ζ is neglected (Bathe, 2016).

Fig. 9 shows the period elongations, amplitude decays in velocity, and average drift in displacement between subdomains Ω^A and Ω^B with the MTS-Bathe method for the γ-Bathe schemes with parameters $\gamma^A \in (0, 1)$ and $\gamma^B \in (0, 1)$, $\omega_0^B/\omega_0^A = 1$, and time-step ratio $m \in \{2, 5\}$. In these plots, a total of 150 values for $\Delta T/T_0$ are chosen along the abscissa and the time-step ratio $m = \Delta T/\Delta t$ is varied by changing the time-step for subdomain B i.e. Δt. Note that when γ^A or γ^B approach 0 or 1, then the period elongation is maximum and amplitude decay is minimum. On the other hand, when (γ^A, γ^B) are chosen to be (γ_0^A, γ_0^B) or $(0.5, 0.5)$, period elongation is

minimized and amplitude decay is maximized. Both these characteristics are similar to those of the underlying UTS-Bathe scheme (see Table 1 in Section 2.2). Similar trends are observed for various combinations of the Bathe parameters for the split SDOF problem suggesting that the MTS-Bathe method inherits the numerical characteristics of the underlying UTS-Bathe methods.

In Fig. 10, we compare the characteristics of different MTS-Bathe methods to the MTS-TR method for $\omega_0^B/\omega_0^A = 2,\ 10,\ 100$ and varying time-step ratios $m = 1,\ 2,\ 5,\ 50$. Again, larger values of the time-step ratio $m = \Delta T/\Delta t$ are achieved by choosing progressively smaller values of Δt. Note that reducing Δt, in general, leads to a smaller period elongation and amplitude decay and hence a more accurate solution, not only in subdomain B, but also subdomain A. For stiff-flexible problems, numerical damping can be helpful in attenuating spurious oscillations (Bathe and Noh, 2012). Thus, methods with some amplitude decay and low period elongation are well-suited for such problems and Fig. 10 indicates that MTS-Bathe methods with the following parameters possess this property: $(\rho_\infty^A, \rho_\infty^B, \gamma^A, \gamma^B)$: $(0, 0, \gamma_0^A, \gamma_0^B)$, or $(1, 1-\sqrt{3}, 0.5, \gamma_p^B)$, or $(1, 0, 0.5, \gamma_0^B)$. In general, even though the numerical damping leads to reduced accuracy, it can help with stability in nonlinear problems (Bathe, 2007; Bathe and Baig, 2005). This is the case, as we show later in Sections 6.3, 6.5, and 6.6, where the MTS-Bathe method with parameters $(0, 0, \gamma_0^A, \gamma_0^B)$ is used to achieve accurate solutions for linear and nonlinear stiff-flexible problems.

6. NUMERICAL EXAMPLES

In this section, we present six numerical examples to demonstrate the performance of the MTS-Bathe method. We compare the solutions from the MTS-Bathe method and the MTS-TR method. To quantify accuracy, we define four measures of error: the maximum local instantaneous error, $\max_{i,n} e_i^n(x)$, maximum local cumulative error, $\max_n e^n(x)$, maximum global instantaneous error,

$\max_i e_i(x)$, and global cumulative error, $E(x)$:

$$e_i^n(x) = \frac{|x_i^n - \hat{x}_i^n|}{\max_{i,n} \hat{x}_i^n - \min_{i,n} \hat{x}_i^n}; \qquad e^n(x) = \frac{1}{N_i} \sum_i e_i^n(x);$$
$$e_i(x) = \frac{1}{N_n} \sum_n e_i^n(x); \qquad E(x) = \frac{1}{N_i} \sum_i e_i(x) \tag{79}$$

where i and n denote the time-step ($i = 0, 1, 2, ..., N_i = T/\Delta T$) and degree of freedom ($n = 1, 2, ..., N_n$), respectively (where T is the time duration and N_n is the total number of degrees). The variables x_i^n and $\hat{x}_i^n$ denote the numerical solution and a reference solution, respectively, at a degree of freedom n at time t_i. The reference solution is taken to be the exact solution, when available. When the exact solution is not available, we specify how the reference solution is obtained. The error measures in Eq. (79) are devised to quantify errors in both, space and time. The terms *local* and *global* denote whether the error is being computed at a specific degree of freedom n in the model or if it is an average error over all degrees of freedom. Similarly, the terms *instantaneous* and *cumulative* refer to errors at a particular instant of time in contrast to an overall error over the duration of the simulation.

6.1 Split single degree-of-freedom problem

In this section, we solve a split SDOF problem, as shown in Eq. (52), with the following problem parameters: $M^A = 2 \times 10^{-6}$, $M^B = 10^{-6}$, $D^A = D^B = 0$, $K^A = 3 \times 10^4$, $K^B = 2 \times 10^4$, $f^A(t) = 3$, and $f^B(t) = 1$. We impose zero initial displacement and velocity, and solve for the response over the time duration $[0, T]$ where $T = 5T_0$ i.e. 5 time periods of the undecomposed system.

We solve the split SDOF problem with the MTS-TR method and the four MTS-Bathe methods listed in Table 2 with time-step ratios of $m = 2$ and $m = 5$. Here, the block time-step is $\Delta T = 4.87 \times 10^{-6}$ for MTS-TR method (which is one-tenth of the time period i.e. $\Delta T/T_0 = 0.1$)

and $\Delta T = 9.74 \times 10^{-6}$ for MTS-Bathe method i.e. twice that of MTS-TR method. Note that these values of ΔT for both methods ensure that the computational costs of the two methods are equivalent because the MTS-Bathe method requires roughly twice the computational effort of MTS-TR method for the same ΔT.

Fig. 11 compares the time-history of velocity and interface reactions obtained from the five methods above. Computational costs of these methods are compared in Fig. 12 which shows the wall-clock time taken by these methods averaged over 5000 runs. We observe that when the block time-step for MTS-Bathe methods is chosen to be twice that of the MTS-TR method, then these methods have similar computational costs. Note that as the time-step ratio between subdomains Ω^A and Ω^B increases from 2 to 5, the computational cost does not increase proportionally. This is because the computational time includes the cost of solving the two subdomains and computing the Lagrange multipliers. In general, the computational cost does not increase linearly as the time-step ratio increases. This is why MTS methods have a computational advantage over UTS methods and this is even more apparent for MDOF systems.

Finally, Fig. 13 shows the global cumulative errors $E(d)$, $E(v)$, $E(a)$, $E(\lambda)$ for the MTS-TR and MTS-Bathe methods computed according to Eq. (79). Note that, like the MTS-TR method, the MTS-Bathe methods 1, 2, and 4 (i.e. with $\gamma \neq \gamma_p$) are second-order accurate, whereas, the truncation error analysis in Section 5.1 predicts only a first-order rate of convergence overall. Similarly, MTS-Bathe 3 (i.e. with $\gamma = \gamma_p$) is observed to be third-order accurate in displacements and velocities, and second-order accurate in accelerations and the Lagrange multiplier. In contrast, theoretically one would expect a first-order rate of convergence. It is surprising that, for this problem, we observe higher rates of convergence than what our analysis in Section 5.1 predicted. This may be due to a cancellation of local truncation errors between different quantities that was not captured in our theoretical analysis. This figure also shows that for the same block time-step ΔT, errors for the MTS-Bathe method are much lower than that of the MTS-TR method. Note,

however, that if the block time-step ΔT for the MTS-Bathe methods is chosen to be twice that of the MTS-TR method (for computational cost parity), then the errors for the MTS-TR and MTS-Bathe with $\gamma \neq \gamma_p$ methods will be very similar.

6.2 Nonlinear split single degree-of-freedom problem with nonlinear inertial terms

We consider a SDOF van der Pol oscillator with a nonlinear inertial term as described by Semler et al. (1996):

$$(1 + (d_{n+1})^2)a_{n+1} + (c + (d_{n+1})^2)v_{n+1} + d_{n+1} = 0 \tag{80}$$

where c is a negative valued damping coefficient for which the system exhibits a supercritical Hopf bifurcation. Such nonlinear inertial terms can result from geometric nonlinearities in fluid-structure interaction problems (Robinson et al., 2020). Upon DD, the two nonlinear split SDOF problems corresponding to Eq. (80) may be written as:

$$\begin{aligned}(1 + (d^A_{n+1})^2)a^A_{n+1} + (c^A + (d^A_{n+1})^2)v^A_{n+1} + d^A_{n+1} + \lambda_{n+1} = 0\\ (1 + (d^B_{n+1})^2)a^B_{n+1} + (c^B + (d^B_{n+1})^2)v^B_{n+1} + d^B_{n+1} - \lambda_{n+1} = 0\end{aligned} \tag{81}$$

where c^A and c^B are negative damping coefficients such that $c = (c^A + c^B)/2$.

We solve Eq. (81) using the MTS-TR method, the MTS-γ-Bathe method with $\gamma = \gamma_0$ and the MTS-ρ_∞-Bathe method with $\rho_\infty = 1$ and $\gamma = \gamma_0$, over the duration $[0, 160]$ with a small initial perturbation of $d(t = 0) = -10^{-7}$ and $v(t = 0) = 0$. We choose $c^A = -2$ and $c^B = -0.3$ such that subdomains Ω^A and Ω^B have slow and fast dynamic characteristics. A reference solution to the original undecomposed nonlinear SDOF problem is obtained using the UTS-γ-Bathe scheme with $\gamma = \gamma_0$ and small time-step $\Delta t = 10^{-4}$. For each time-step, nonlinear iterations are conducted until a tolerance of 10^{-7} and 10^{-12} is achieved for the absolute and relative residuals, respectively, while limiting the maximum number of iterations to 1000. We use a time-step ratio of $m = 6$ for simulating this problem because the selection of $c^A = -2$ and $c^B = -0.3$ leads to periods of

$T_0^A \approx 40$ and $T_0^B \approx 7.5$ (Kim and Choi, 2018; Semler et al., 1996). We consider five different cases: $\Delta T = 0.05$, 0.1, 0.2, 0.5, and 1 where ΔT is the block time-step for the proposed MTS-Bathe method. For computational cost parity, the block time-step of the MTS-TR method is set to $\Delta T/2$.

Fig. 14 compares the time history and phase space diagrams of displacement and velocity obtained from the MTS-TR method and the proposed MTS-Bathe methods for $\Delta T = 0.5$ (i.e. $T_0^A/\Delta T \approx 80$). One may note that while all three MTS methods are able to simulate this problem with inertial nonlinearity, the MTS-γ-Bathe method has greater period error than the other two. Fig. 15 presents the time history and Fourier spectrum of accelerations which show the presence of spurious oscillations in accelerations, typically observed in numerical solution of stiff-flexible systems. Interestingly, even though the MTS-γ-Bathe method has greater period error, the magnitude of spurious oscillations it exhibits is lower. The frequency of these spurious oscillations is found to be approximately 2 Hz for the MTS-TR method and 1 Hz for the MTS-Bathe methods, coincident with the frequency corresponding to the block time-steps used for these methods. Finally, maximum errors in displacement, velocity, and acceleration $\max(E(d), E(v), E(a))$ are shown in Fig. 16 for five values of block time-step ΔT. As is evident, all three MTS methods are able to achieve a convergence rate of 2, preserving the accuracy of their underlying UTS schemes.

6.3 Three degree-of-freedom problem including stiff and flexible parts

In this section, we consider a three degree-of-freedom (3-DOF) model shown in Fig. 17 decomposed into stiff and flexible sub-systems. This 3-DOF system is a benchmark problem to study general stiff and flexible structures (Bathe and Noh, 2012; Noh and Bathe, 2018, 2019a). The system is excited by specifying the displacement of mass m_1 as a sinusoidal function with frequency ω_p. Further details of this 3-DOF model problem and comments on the importance of the problem are given in Bathe (2016); Bathe and Noh (2012).

As shown in Fig. 17, we can decompose the 3-DOF system into two subdomains linked by one interface reaction λ, for which the governing equations are:

$$\begin{bmatrix} m_2^A & 0 \\ 0 & m_3 \end{bmatrix} \begin{bmatrix} a_2^A \\ a_3 \end{bmatrix} + \begin{bmatrix} k_2 & -k_2 \\ -k_2 & k_2 \end{bmatrix} \begin{bmatrix} d_2^A \\ d_3 \end{bmatrix} + \begin{bmatrix} \lambda \\ 0 \end{bmatrix} = \begin{bmatrix} 0 \\ 0 \end{bmatrix} \tag{82}$$

$$\begin{bmatrix} m_1^B & 0 \\ 0 & m_2^B \end{bmatrix} \begin{bmatrix} a_1 \\ a_2^B \end{bmatrix} + \begin{bmatrix} k_1 & -k_1 \\ -k_1 & k_1 \end{bmatrix} \begin{bmatrix} d_1 \\ d_2^B \end{bmatrix} + \begin{bmatrix} 0 \\ -\lambda \end{bmatrix} = \begin{bmatrix} R_1 \\ 0 \end{bmatrix} \tag{83}$$

where R_1 is the reaction at node 1. Since we prescribe the displacement at node 1, Eq. (83) can be rewritten as:

$$m_2^B a_2^B + k_1 d_2^B - \lambda = k_1 d_1 \tag{84}$$

and the reaction R_1 is computed as $R_1 = k_1 d_1 - k_1 d_2^B$. The parameters chosen for this 3-DOF system are: $m_1 = 0$, $m_2 = m_3 = 1$, $k_1 = 10^7$, $k_2 = 1$ and $\omega_p = 1.2$. Initial conditions are $d_2(t = 0) = d_3(t = 0) = 0$, $v_2(t = 0) = w_p$, and $v_3(t = 0) = 0$. For the decomposed system, mass of node 2 is divided equally: $m_2^A = m_2^B = 0.5$. For time integration of such stiff-flexible problems, it is recommended to use $\rho_\infty = 0$ (Kwon et al., 2020). Thus, the parameter set $(\rho_\infty^A, \rho_\infty^B) = (0, 0)$ is used for the MTS-Bathe method and all splitting ratios γ, γ^A, γ^B are taken to be 0.5. The two natural periods of this system are 0.002 and 6.283, and in accordance with Bathe and Noh (2012), we choose the time-steps for this problem as 0.2618 for the UTS-Bathe method and the block time-step for the MTS-Bathe method. Similarly, for computational cost parity, we choose half the value, 0.1309, as the time step for the UTS-TR method and the block time-step for the MTS-TR method.

Fig. 18 shows numerical results for the 3-DOF stiff-flexible problem using various UTS and MTS methods with a time-step ratio of $m = 3$. The solution obtained by mode superposition

is taken to be the 'reference solution' (Noh and Bathe, 2019a). As previously shown by Bathe and Noh (2012), the UTS-TR method gives poor results for this stiff-flexible problem. Not surprisingly, the MTS-TR method inherits this trait. Fig. 19 compares the errors in acceleration of node 2 and the reaction at node 1 against computational cost (averaged over 100 runs) for the four different UTS and MTS methods. It is also observed that the MTS-Bathe method for the γ-Bathe scheme provides the best results – even when compared to the UTS-Bathe scheme for comparable computational cost and should be the method of choice for such stiff-flexible systems.

6.4 Two-dimensional bi-material cantilever beam problem

In this section, we consider a two-dimensional (2D) bi-material beam in plane stress, shown in Fig. 20. The bi-material beam is composed of subdomains Ω^A and Ω^B with mass densities $\rho^A = 20\rho^B = 1.0 \times 10^{-4}$, elastic modulus $E^A = E^B/60 = 1.0 \times 10^4$, and Poisson's ratio $\nu^A = \nu^B = 0.3$. Dirichlet boundary conditions on the left wall are $d_x^A(t) = 0$ at $x = 0$ and $d_y^A(t) = 0$ at $(x, y) = (0, 2)$.

6.4.1 Undamped beam with external force

First, we consider the beam to be undamped with zero initial displacement and velocity. A harmonic external force is applied per unit length of the right edge as:

$$\boldsymbol{f}^A(t) = 0 \quad \forall \quad \boldsymbol{x} \in \Omega^A, \qquad \boldsymbol{f}^B(t) = \begin{cases} [0 \quad 2.25\sin(6000t)]^T & \forall \quad x = 20 \\ 0 & \text{otherwise} \end{cases} \tag{85}$$

This structural dynamics problem is solved using the UTS-TR, MTS-TR, UTS-Bathe and MTS-Bathe methods. For spatial discretization, we use an uniform mesh of four-node elements with equally spaced nodes ($\Delta x = \Delta y = h = 0.5$). A numerical solution using the UTS-Bathe scheme with $\gamma = \gamma_p$ and $\Delta t = 5 \times 10^{-9}$ is taken to be a reference solution because the UTS-Bathe

scheme with $\gamma = \gamma_p$ leads to the third-order accuracy (Kwon et al., 2021). For computational cost parity, the time-step size for the UTS-TR method and the block time-step size for the MTS-TR method are chosen as half time-step for the UTS-Bathe method and the block time-step size for the MTS-Bathe method. The time duration of the simulation is considered as $[0, 0.0002]$.

Fig. 21 compares global cumulative errors against computational cost for the UTS-TR, UTS-Bathe, MTS-TR, and MTS-Bathe methods for a time-step ratio $m = 5$. We observe that the MTS-Bathe method with $\gamma = \gamma_p$ yields the smallest errors. Note that, for a fixed computational cost, the MTS-Bathe method provides more accurate results than the UTS-Bathe method. This is the main benefit of MTS methods because they are able to maintain high accuracy in stiff subdomains by using small time-steps and also keep computational cost low by using large time-steps in flexible subdomains. Thus, the proposed MTS-Bathe method is better suited for large stiff-flexible problems in structural dynamics than other methods in the literature.

6.4.2 Damped beam problem with a nonzero initial velocity condition

Next, we consider a cantilever beam with Rayleigh damping. No external force is applied, but a zero initial displacement and a nonzero initial velocity is applied on the right edge as follows:

$$\boldsymbol{v}^A(t=0) = 0 \quad \forall \quad \boldsymbol{x} \in \Omega^A, \qquad \boldsymbol{v}^B(t=0) = \begin{cases} [0 \quad 1]^T & \forall \quad x = 20 \\ 0 & \text{otherwise} \end{cases} \tag{86}$$

The problem is solved using the MTS-TR method and the MTS-Bathe methods with $\rho_\infty = 0,\ 0.65,\ 1$ and $\gamma = \gamma_0$ (see Table 1). The subdomains are assumed to have the same mass- and stiffness-proportional Rayleigh damping coefficients of 2.0×10^{-4} and 8.0×10^{-4}, respectively. A regular mesh of four-node elements with equally spaced nodes ($\Delta x = \Delta y = h = 1$) is used for spatial discretization. Note that the P- and S-wave velocities are $20\sqrt{3}c_p^A = c_p^B = 3.6313 \times 10^5$ and $20\sqrt{3}c_s^A = c_s^B = 2.1483 \times 10^5$, respectively. Thus, for accuracy, one should pick a time-step

$\Delta t = 3 \times 10^{-6}$ for subdomain Ω^B and $\Delta T = 10^{-4}$ for subdomain Ω^A.

A reference solution to this problem is obtained using the UTS-γ-Bathe scheme with $\gamma = \gamma_0$ and $\Delta t = 1.0 \times 10^{-7}$ because this method has been shown to produce accurate solutions to stiff-flexible problems and wave propagation problems (Bathe and Noh, 2012; Kwon et al., 2020; Noh and Bathe, 2018, 2019a). To compare the MTS-TR and MTS-Bathe methods using similar computational costs, the block time-step for the MTS-TR method is set as $\Delta T/2$, where $\Delta T = 1.0 \times 10^{-5}$ is the block time-step chosen for the MTS-Bathe method. The time duration of the simulation is $[0, T]$ where $T = 0.0048$ and the solution is obtained by using a time-step ratio of $m = 2$ for both methods.

Fig. 22 shows plots of the normal stress σ_{xx} and the scaled deformed state of the beam at $t = 2.4 \times 10^{-3}$. It is observed that the results of the MTS-Bathe methods with $\rho_\infty = 0$ and $\rho_\infty = 0.65$ are similar to the reference solution. On the other hand, the MTS-TR method and the MTS-Bathe method with $\rho_\infty = 1$ give residual stress errors around the interface between subdomains Ω^A and Ω^B. This is because, the Bathe scheme with $\rho_\infty = 1$ and $\gamma = \gamma_0$ has the same properties as the two-step trapezoidal rule.

To quantify the errors due to these residual stresses, Fig. 23 shows the maximum local instantaneous errors of σ_{xx}. We note that for even values of the time-step ratio m, the MTS-TR method leads to large errors in stress and observe that relative errors in stress are concentrated around the interface between subdomains Ω^A and Ω^B (see Fig. 22). On the other hand, the MTS-Bathe method works well for both odd and even time-step ratios and does not suffer from the peculiar error characteristics of the MTS-TR method for even-valued time-step ratios.

Fig. 24 shows global cumulative errors in displacement and velocity using MTS-TR method and MTS-Bathe methods for different values of the block time-step ΔT and for time-step ratios of $m = 2$ and 5. We note that errors in displacement are similar for all the methods considered and for the two different time-step ratios. On the other hand, while errors in velocity decrease with

decreasing block time-step size ΔT and increasing time-step ratio m, the convergence rate for the MTS-Bathe methods is markedly better than that of the MTS-TR method. This is due to the fact that for stiff-flexible problems, the TR method (both UTS and MTS) exhibits spurious oscillations and the effect of these oscillations is more pronounced in velocity and acceleration time-histories. Thus, in general, for stiff-flexible problems, the proposed MTS-Bathe method gives more accurate solutions compared to the MTS-TR method for similar computational effort.

6.5 Nonlinear two-story shear building

To demonstrate the stability characteristics of the MTS-Bathe method for nonlinear problems, we consider a two-story shear building, as shown in Fig. 25. The nonlinear spring stiffness for each story is given as:

$$k_{NL,i} = k_i(1 + \delta_i(\Delta d_i)^2) \quad \text{for } i = 1,\, 2 \tag{87}$$

where k_i is the initial stiffness and $\Delta d_i = d_i - d_{i-1}$ is the story drift for story i. Note that $\Delta d_1 = d_1$ because d_0 is taken to be zero. We choose the following problem parameters: $m_1 = 10^3$, $m_2 = 10^4$, $k_1 = 10^4$, $k_2 = 10^3$, $\delta_1 = -1$, $\delta_2 = 5$, $f_1(t) = f_2(t) = 2500\sin(\omega_p t)$, and $\omega_p = \pi/2$ (corresponding forcing period is $T_p = 4$). Zero initial displacement and velocity are applied. A reference solution to this nonlinear problem is obtained using the UTS-γ-Bathe scheme with $\gamma = \gamma_0$ and a small time-step $\Delta t = T_p/8000 = 5 \times 10^{-4}$. Fig. 26 shows the time history, phase plot, and Poincaré section of the reference solution depicting chaotic behavior of the system.

The system is partitioned into two subdomains, Ω^A and Ω^B, by dividing the mass of the bottom story equally between the two subdomains. The decomposed equations of motion can be written

as:

$$\begin{bmatrix} 0.5m_1 & 0 \\ 0 & m_2 \end{bmatrix} \begin{bmatrix} a_1^A \\ a_2^A \end{bmatrix} + \begin{bmatrix} k_{NL,2} & -k_{NL,2} \\ -k_{NL,2} & k_{NL,2} \end{bmatrix} \begin{bmatrix} d_1^A \\ d_2^A \end{bmatrix} + \begin{bmatrix} -\lambda \\ 0 \end{bmatrix} = \begin{bmatrix} 0.5f_1 \\ f_2 \end{bmatrix} \tag{88}$$

$$0.5m_1 a_1^B + k_{NL,1} d_1^B + \lambda = 0.5f_1 \tag{89}$$

The decomposed system is solved using the proposed MTS-Bathe method with $\gamma = \gamma_0$ and the MTS-TR method. We consider two cases: $\Delta T = T_p/4 = 1$ and $\Delta T = T_p/400 = 0.01$, where ΔT is the block time-step for the MTS-Bathe method. Again, the block time-step for the MTS-TR method is set to $\Delta T/2$ for computational cost parity. Figs. 27(a) and 28(a) show the time history of displacement and phase space diagram of the bottom story obtained from these methods when $\Delta T = 1$ and $m = 10$. From Fig. 29(a), the primary frequency obtained using the proposed MTS-Bathe method is found to be 0.25, which corresponds to the forcing frequency $f_p = \omega_p/2\pi$. Due to numerical damping of the MTS-Bathe method, however, the Fourier amplitude of higher frequencies is diminished. Note that the MTS-TR method loses its stability, whereas the proposed MTS-Bathe method remains stable, indicating that some numerical damping may be desirable in a time integration method for stability in nonlinear structural dynamics. Nevertheless, as shown in Figs. 27(b), 28(b), and 29(b), both methods give accurate solutions when a small time-step, $\Delta T = 0.01$, is used.

6.6 Nonlinear multi-degree-of-freedom problem with stiff and flexible parts

In this section, we solve a 21-DOF nonlinear problem with a specified displacement of $d_0 = \sin(\omega_p t)$ at the 0$^{\text{th}}$ DOF, as shown in Fig. 30. Conceptually, this problem can be treated as a 21-story shear building with the bottom 11 stories being stiff (Ω^B) and the top 10 stories being flexible

(Ω^A). The nonlinear internal force p_i between DOF $i-1$ and DOF i is taken to be of the form:

$$p_i = k_{1,i}(d_i - d_{i-1}) + k_{3,i}(d_i - d_{i-1})^3 \tag{90}$$

where $k_{1,i}$ and $k_{3,i}$ represent the linear and cubic internal force coefficients, respectively, for story i. We decompose the problem domain into two subdomains by splitting it at DOF 11 and connecting the two subdomains with one Lagrange multiplier λ as shown in Fig. 30. Other problem parameters are chosen as: mass of each story $m_i = 1$ for $i = 0, 1, 2, ..., 21$, forcing frequency $\omega_p = 2\pi$, linear internal force coefficients $k_{1,i} = 10^7$ for Ω^B ($i = 1, 2, ..., 11$), cubic internal force coefficients $k_{3,i} = 10^3$ for Ω^B ($i = 1, 2, ..., 11$), linear and cubic internal force coefficients $k_{1,i} = k_{3,i} = 1$ for Ω^A ($i = 12, 13, ..., 21$). The system is assumed to be initially undeformed i.e. $d_i(t = 0) = 0$ for $i = 1, 2, ..., 21$, but with a uniform initial velocity $v_i(t = 0) = \omega_p$ for $i = 1, 2, ..., 11$, and zero initial velocity $v_i(t = 0) = 0$ for $i = 12, 13, ..., 21$. This initial state mimics a stiff-flexible structure undergoing sudden motion.

A reference solution to this problem is obtained using the UTS-γ-Bathe method with $\gamma = \gamma_0$ and $\Delta t = 0.001$. The problem is then solved using the MTS-Bathe method with $\gamma = \gamma_0$ for both subdomains. Two values of the block time-step for the MTS-Bathe method are considered: $\Delta T = 0.3$ and $\Delta T = 0.05$. Block time-step for the MTS-TR method is taken to be $\Delta T/2$ for computational cost parity. Time-step ratio is chosen as $m = 6$ for both MTS methods.

Fig. 31 compares the phase plane diagrams at nodes 5 and 12 obtained using the MTS-TR and MTS-Bathe methods. At node 5, which is in the stiff subdomain, both MTS methods yield similar results as the reference solution because the dominant frequency of this response is the forcing frequency of the prescribed displacement (i.e. $f = \omega_p/2\pi = 1$) (see the corresponding Fourier spectrum in Fig. 32). On the other hand, the response of node 12 has three dominant frequencies: $f_1 = 0.3$, $f_2 = 1$, and $f_3 = 3$ (with corresponding dominant periods of $T_1 \approx 3.33$, $T_2 = 1$, and $T_3 = 0.33$). Thus, $\Delta T = 0.3$ is too coarse for this problem (as $T_3/\Delta T = 1.1$) and leads to poor

results. On the other hand, with $\Delta T = 0.05$, both MTS-TR and MTS-Bathe are able to capture the dynamics of the system well.

Fig. 33 shows the time history of acceleration at nodes 5 and 12 in the duration $[0, 10]$. It is observed that the MTS-TR method gives poor results at node 5 for large ΔT because it cannot suppress spurious oscillations at high frequencies. For instance, as shown in Fig. 32, when $\Delta T = 0.3$, Fourier amplitudes of acceleration at $f = 17.8$, 19.3, and 19.8 are not negligible. Even for the small block time-step of $\Delta T = 0.05$, there is a peak at $f = 57.5$ in the Fourier spectrum obtained from MTS-TR. On the other hand, the MTS-Bathe method gives an accurate solution owing to numerical dissipation at high frequencies. Thus, in general, MTS-Bathe performs better than MTS-TR for both, linear and nonlinear stiff-flexible problems – a characteristic that these methods share with their underlying UTS schemes.

Finally, Table 3 shows the computational costs and the total number of nonlinear iterations conducted in solving this problem using the two MTS methods. Even though the overall computational cost of the MTS-Bathe method is more than the MTS-TR method, we note from Fig. 34 that the MTS-Bathe method has lower error than MTS-TR method for comparable computational cost. The MTS-Bathe method has a slightly larger total computational cost for this problem than the MTS-TR method because, for nonlinear problems, one must recompute the Y matrices from Eq. (46) for every nonlinear iteration whereas, for linear problems, the Y matrix can be computed in advance of the time-stepping loop and does not change for the duration of the simulation. This example shows that, for comparable computational cost, the proposed MTS-Bathe method gives more accurate result than the MTS-TR method, especially for stiff-flexible problems in structural dynamics.

7. CONCLUDING REMARKS

In the present study, a multi-time-step (MTS) method for the composite ρ_∞-Bathe time integration schemes is presented for simulating the dynamics of stiff-flexible structural systems. The proposed MTS-Bathe method uses *two* novel constraint conditions that are necessary for achieving unconditional stability and high accuracy at a low computational cost. This is achieved by investigating the response of a split SDOF system for several different constraint conditions numerically. It is found that imposing the continuity of velocity at every block time-step and linearly interpolating the Lagrange multipliers for the sub-steps leads to unconditional stability. An analytical proof of stability using the energy method is given in Section 4 showing that the proposed MTS method is unconditionally stable.

A local truncation error (LTE) analysis of the proposed MTS-Bathe method is carried out to show that the method preserves the order of LTEs in displacements and velocities, while the order of LTEs in accelerations and Lagrange multipliers is lower in comparison to the underlying UTS-Bathe schemes. Surprisingly however, from numerical examples, the rate of convergence of the proposed MTS method was observed to be better than what is predicted by the LTE analysis. Next, a split SDOF system is used to compare numerical characteristics such as period elongation and amplitude decay for velocities, and also to quantify the average drift in displacements between subdomains for the proposed MTS-Bathe method. We show that the proposed MTS-Bathe method inherits the property of the underlying UTS-Bathe schemes to dissipate spurious oscillations encountered with stiff-flexible systems and since it uses different time-steps in the stiff and flexible parts of the problem, it is also able to reduce the computational cost while maintaining high accuracy.

Finally, computational performance of the proposed MTS-Bathe method is compared by numerically solving several linear and nonlinear problems in structural dynamics with stiff and flexible parts. Error vs. computational cost curves for the proposed MTS-Bathe method are compared

to those of existing methods for several different combinations of algorithmic parameters and time-steps. It is shown that the MTS-Bathe method has lower errors for the same computational cost, or conversely, has lower computational cost for similar levels of error. Thus, we believe that the proposed MTS-Bathe method is better suited for simulating the structural dynamics of stiff-flexible systems than other methods in the literature.

ACKNOWLEDGMENTS

This work is partly supported by the National Science Foundation (NSF) through Grant CNS-2229136: Collaborative Research: CPS: Co-Designed Control and Scheduling Adaptation for Assured Cyber-Physical System Safety and Performance. The authors also acknowledge support from the Computational Interdisciplinary Graduate Program (CIGP) of Purdue University.

A. AMPLIFICATION MATRIX A OF THE MTS-BATHE METHOD

Here, we describe the procedure to obtain the amplification matrix $\boldsymbol{A}$ defined in Eq. (55). The state variables are decomposed into free part and link correction:

$$\begin{bmatrix} \boldsymbol{z}_m^A \\ \boldsymbol{z}_m^B \end{bmatrix} = \begin{bmatrix} \overline{\boldsymbol{z}}_m^A \\ \overline{\boldsymbol{z}}_m^B \end{bmatrix} + \begin{bmatrix} \boldsymbol{z}_m'^A \\ \boldsymbol{z}_m'^B \end{bmatrix} \tag{A1}$$

Uncoupled-free part

For the uncoupled-free part, it holds that

$$\begin{bmatrix} \overline{\boldsymbol{z}}_m^A \\ \overline{\boldsymbol{z}}_m^B \end{bmatrix} = \begin{bmatrix} \overline{\boldsymbol{A}}^{AA} & \overline{\boldsymbol{A}}^{AB} \\ \overline{\boldsymbol{A}}^{BA} & \overline{\boldsymbol{A}}^{BB} \end{bmatrix} \begin{bmatrix} \boldsymbol{z}_0^A \\ \boldsymbol{z}_0^B \end{bmatrix} \tag{A2}$$

From $\mathrm{M}\bar{\mathrm{z}} = \mathrm{r}$, the state variables for the uncoupled-free part can be expressed as

$$\begin{aligned}
&\overline{\boldsymbol{z}}^A_{\gamma^A m} = \boldsymbol{A}^A_{TR}\boldsymbol{z}^A_0, \quad \overline{\boldsymbol{z}}^A_m = \boldsymbol{A}^A_{Bathe}\boldsymbol{z}^A_0 \\
&\overline{\boldsymbol{z}}^B_m = \left(\boldsymbol{A}^B_{Bathe}\right)^m \boldsymbol{z}^B_0 + \sum_{j=0}^{m-1} \left(\boldsymbol{A}^B_{Bathe}\right)^{m-j-1} \boldsymbol{A}^B_{0,j+1}\boldsymbol{z}^A_0
\end{aligned} \tag{A3}$$

where $\boldsymbol{A}^B_{0,j+1} = -\left(\boldsymbol{L}^B_a c_{0,j+\gamma^B} + \boldsymbol{L}^B_b c_{0,j+1}\right)\left[1,\, 2\zeta^A\omega^A_0,\, (\omega^A_0)^2\right]$. $\boldsymbol{A}_{TR}$ is the amplification matrix for the UTS-trapezoidal rule when time-step is $\gamma\Delta t$ (see Appendix B), and $\boldsymbol{A}_{Bathe}$, $\boldsymbol{L}_a$, and $\boldsymbol{L}_b$ are the amplification matrix and load vectors for the UTS-Bathe scheme (see Appendix A in Ref. Noh and Bathe (2019a)) when time-step is Δt with a particular subdomain denoted by its superscript.

Thus,

$$\begin{aligned}
&\overline{\boldsymbol{A}}^{AA} = \boldsymbol{A}^A_{Bathe}, \quad \overline{\boldsymbol{A}}^{AB} = 0, \\
&\overline{\boldsymbol{A}}^{BA} = \sum_{j=0}^{m-1} \left(\boldsymbol{A}^B_{Bathe}\right)^{m-j-1} \boldsymbol{A}^B_{0,j+1}, \quad \overline{\boldsymbol{A}}^{BB} = \left(\boldsymbol{A}^B_{Bathe}\right)^m
\end{aligned} \tag{A4}$$

Interface

From $\mathrm{MY} = \mathrm{C}^{\mathrm{T}}$, the interface matrices are:

$$\begin{aligned}
&\boldsymbol{Y}^{A1}_{\gamma^A m} = \boldsymbol{L}^A_{TR}, \quad \boldsymbol{Y}^{A1}_m = \boldsymbol{L}^A_a, \quad \boldsymbol{Y}^{A2}_{\gamma^A m} = 0, \quad \boldsymbol{Y}^{A2}_m = \boldsymbol{L}^A_b, \\
&\boldsymbol{Y}^{B1}_m = \sum_{j=0}^{m-1} (\boldsymbol{A}^B_{Bathe})^{m-j-1}\boldsymbol{A}^B_{1,j+1}, \quad \boldsymbol{Y}^{B2}_m = \sum_{j=0}^{m-1} (\boldsymbol{A}^B_{Bathe})^{m-j-1}\boldsymbol{A}^B_{2,j+1}
\end{aligned} \tag{A5}$$

where $\boldsymbol{A}^B_{1,j+1} = -\left(\boldsymbol{L}^B_a c_{1,j+\gamma^B} + \boldsymbol{L}^B_b c_{1,j+1}\right)$ and $\boldsymbol{A}^B_{2,j+1} = -\left(\boldsymbol{L}^B_a c_{2,j+\gamma^B} + \boldsymbol{L}^B_b c_{2,j+1}\right)$.

From $[\mathrm{BM}^{-1}\mathrm{C}^{\mathrm{T}}]\lambda = \mathrm{BM}^{-1}\mathrm{r} - \mathrm{s}$, the Lagrange multipliers are computed from the previous state variables for the both subdomains.

$$\boldsymbol{A}_\lambda \begin{bmatrix} \lambda_{\gamma^A m} \\ \lambda_m \end{bmatrix} = \boldsymbol{B}_\lambda \begin{bmatrix} \boldsymbol{z}^A_0 \\ \boldsymbol{z}^B_0 \end{bmatrix} \tag{A6}$$

where

$$\boldsymbol{A}_\lambda = \begin{bmatrix} -\left[1,\, 2\zeta^B\omega_0^B,\, (\omega_0^B)^2\right]\gamma^A\boldsymbol{Y}_m^{B1} - \left[1,\, 2\zeta^A\omega_0^A,\, (\omega_0^A)^2\right]\boldsymbol{Y}_{\gamma^A m}^{A1} & \boldsymbol{B}^A\boldsymbol{Y}_m^{A1} + \boldsymbol{B}^B\boldsymbol{Y}_m^{B1} \\ -\left[1,\, 2\zeta^B\omega_0^B,\, (\omega_0^B)^2\right]\gamma^A\boldsymbol{Y}_m^{B2} - \left[1,\, 2\zeta^A\omega_0^A,\, (\omega_0^A)^2\right]\boldsymbol{Y}_{\gamma^A m}^{A2} & \boldsymbol{B}^A\boldsymbol{Y}_m^{A2} + \boldsymbol{B}^B\boldsymbol{Y}_m^{B2} \end{bmatrix}^T$$

$$\boldsymbol{B}_\lambda = \begin{bmatrix} -\left[1,\, 2\zeta^B\omega_0^B,\, (\omega_0^B)^2\right]\gamma^A\overline{\boldsymbol{A}}^{BA} - \left[1,\, 2\zeta^A\omega_0^A,\, (\omega_0^A)^2\right]\boldsymbol{A}_{TR}^A & \boldsymbol{B}^A\overline{\boldsymbol{A}}^{AA} + \boldsymbol{B}^B\overline{\boldsymbol{A}}^{BA} \\ -\left[1,\, 2\zeta^B\omega_0^B,\, (\omega_0^B)^2\right]\left((1-\gamma^A)\boldsymbol{I} + \gamma^A\overline{\boldsymbol{A}}^{BB}\right) & \boldsymbol{B}^B\overline{\boldsymbol{A}}^{BB} \end{bmatrix}^T$$

and $\boldsymbol{B}^A \equiv [0,\, 1,\, 0]$ and $\boldsymbol{B}^B \equiv [0,\, -1,\, 0]$.

Coupled-link correction

From $\mathrm{z}' = -\mathrm{Y}\lambda$, at the final time-step, the state variables of the link correction are

$$\begin{bmatrix} \boldsymbol{z}_m'^A \\ \boldsymbol{z}_m'^B \end{bmatrix} = -\begin{bmatrix} \boldsymbol{Y}_m^{A1} & \boldsymbol{Y}_m^{A2} \\ \boldsymbol{Y}_m^{B1} & \boldsymbol{Y}_m^{B2} \end{bmatrix}\begin{bmatrix} \lambda_{\gamma^A m} \\ \lambda_m \end{bmatrix} = -\begin{bmatrix} \boldsymbol{Y}_m^{A1} & \boldsymbol{Y}_m^{A2} \\ \boldsymbol{Y}_m^{B1} & \boldsymbol{Y}_m^{B2} \end{bmatrix}\boldsymbol{A}_\lambda^{-1}\boldsymbol{B}_\lambda\begin{bmatrix} \boldsymbol{z}_0^A \\ \boldsymbol{z}_0^B \end{bmatrix} \tag{A7}$$

Amplification matrix

From Eqs. (A1), (A2), and (A7), we obtain the amplification matrix of the MTS-Bathe method:

$$\boldsymbol{A} = \begin{bmatrix} \overline{\boldsymbol{A}}^{AA} & \overline{\boldsymbol{A}}^{AB} \\ \overline{\boldsymbol{A}}^{BA} & \overline{\boldsymbol{A}}^{BB} \end{bmatrix} - \begin{bmatrix} \boldsymbol{Y}_m^{A1} & \boldsymbol{Y}_m^{A2} \\ \boldsymbol{Y}_m^{B1} & \boldsymbol{Y}_m^{B2} \end{bmatrix}\boldsymbol{A}_\lambda^{-1}\boldsymbol{B}_\lambda \tag{A8}$$

B. AMPLIFICATION MATRIX AND LOAD VECTOR FOR THE UTS-TRAPEZOIDAL RULE WITH TIME-STEP SIZE $\gamma\Delta T$

$$\boldsymbol{A}_{TR} = \begin{bmatrix} -\frac{\beta}{4} - \kappa & -\frac{1}{\gamma\Delta t}(\beta + 2\kappa) & -\frac{\beta}{(\gamma\Delta t)^2} \\ \frac{\gamma\Delta t}{2}\left(1 - \frac{\beta}{4} - \kappa\right) & 1 - \frac{\beta}{2} - \kappa & -\frac{\beta}{2\gamma\Delta t} \\ \frac{(\gamma\Delta t)^2}{4}\left(1 - \frac{\beta}{4} - \kappa\right) & \gamma\Delta t\left(1 - \frac{\beta}{4} - \frac{\kappa}{2}\right) & 1 - \frac{\beta}{4} \end{bmatrix};\quad \boldsymbol{L}_{TR} = \begin{bmatrix} \frac{\beta}{\omega_0^2(\gamma\Delta t)^2} \\ \frac{\beta}{2\omega_0^2\gamma\Delta t} \\ \frac{\beta}{4\omega_0^2} \end{bmatrix} \tag{B1}$$

where

$$\beta = \left(\frac{1}{\omega_0^2 (\gamma \Delta t)^2} + \frac{\zeta}{\omega_0 \gamma \Delta t} + \frac{1}{4} \right)^{-1}, \quad \kappa = \frac{\zeta \beta}{\omega_0 \gamma \Delta t}$$

REFERENCES

Arrarás, A., Portero, L., and Yotov, I., Error analysis of multipoint flux domain decomposition methods for evolutionary diffusion problems, *Journal of Computational Physics*, vol. **257**, pp. 1321–1351, 2014.

Bank, R., Coughran, W., Fichtner, W., Grosse, E., Rose, D., and Smith, R., Transient simulation of silicon devices and circuits, *IEEE Transactions on Computer-Aided Design of Integrated Circuits and Systems*, vol. **4**, no. 4, pp. 436–451, 1985.

Bashforth, F. and Adams, J.C., *An attempt to test the theories of capillary action by comparing the theoretical and measured forms of drops of fluid*, University Press, 1883.

Bathe, K.J., Conserving energy and momentum in nonlinear dynamics: a simple implicit time integration scheme, *Computers & structures*, vol. **85**, no. 7-8, pp. 437–445, 2007.

Bathe, K.J., *Finite element procedures. 2nd ed*, Higher Education Press China, Watertown (MA), 2016.

Bathe, K.J. and Baig, M.M.I., On a composite implicit time integration procedure for nonlinear dynamics, *Computers & Structures*, vol. **83**, no. 31-32, pp. 2513–2524, 2005.

Bathe, K.J. and Noh, G., Insight into an implicit time integration scheme for structural dynamics, *Computers & Structures*, vol. **98**, pp. 1–6, 2012.

Belytschko, T., Liu, W.K., and Smolinksi, P., 1984. Multi-stepping implicit-explicit procedures in transient analysis. *Innovative methods in Nonlinear Analysis*. Pineridge Press, pp. 135–154.

Belytschko, T. and Mullen, R., Mesh partitions of explicit-implicit time integration, *Formulations and computational algorithms in finite element analysis*, pp. 673–690, 1976.

Belytschko, T., Yen, H.J., and Mullen, R., Mixed methods for time integration, *Computer Methods in Applied Mechanics and Engineering*, vol. **17–18**, pp. 259–275, 1979.

Benzi, M., Golub, G.H., and Liesen, J., Numerical solution of saddle point problems, *Acta numerica*, vol. **14**, pp.

1–137, 2005.

Brun, M., Gravouil, A., Combescure, A., and Limam, A., Two FETI-based heterogeneous time step coupling methods for Newmark and α-schemes derived from the energy method, *Computer Methods in Applied Mechanics and Engineering*, vol. **283**, pp. 130–176, 2015.

Chung, J. and Hulbert, G., A time integration algorithm for structural dynamics with improved numerical dissipation: the generalized-α method, *Journal of Applied Mechanics*, vol. **60**, no. 2, pp. 371–375, 1993.

Combescure, A. and Gravouil, A., A numerical scheme to couple subdomains with different time-steps for predominantly linear transient analysis, *Computer methods in applied mechanics and engineering*, vol. **191**, no. 11-12, pp. 1129–1157, 2002.

Daniel, W., The subcycled Newmark algorithm, *Computational Mechanics*, vol. **20**, no. 3, pp. 272–281, 1997.

Dolean, V., Jolivet, P., and Nataf, F., *An introduction to domain decomposition methods: algorithms, theory, and parallel implementation*, SIAM, 2015.

Dong, S., BDF-like methods for nonlinear dynamic analysis, *Journal of Computational physics*, vol. **229**, no. 8, pp. 3019–3045, 2010.

Farhat, C., Chen, P.S., and Mandel, J., A scalable lagrange multiplier based domain decomposition method for time-dependent problems, *International Journal for Numerical Methods in Engineering*, vol. **38**, no. 22, pp. 3831–3853, 1995.

Farhat, C., Crivelli, L., and Roux, F.X., A transient FETI methodology for large-scale parallel implicit computations in structural mechanics, *International Journal for Numerical Methods in Engineering*, vol. **37**, no. 11, pp. 1945–1975, 1994a.

Farhat, C., Lesoinne, M., LeTallec, P., Pierson, K., and Rixen, D., FETI-DP: a dual–primal unified FETI method—part I: A faster alternative to the two-level FETI method, *International journal for numerical methods in engineering*, vol. **50**, no. 7, pp. 1523–1544, 2001.

Farhat, C., Lesoinne, M., and Pierson, K., A scalable dual-primal domain decomposition method, *Numerical linear algebra with applications*, vol. **7**, no. 7-8, pp. 687–714, 2000.

Farhat, C. and Mandel, J., The two-level FETI method for static and dynamic plate problems Part I: An optimal

iterative solver for biharmonic systems, *Computer methods in applied mechanics and engineering*, vol. **155**, no. 1-2, pp. 129–151, 1998.

Farhat, C., Mandel, J., and Roux, F.X., Optimal convergence properties of the FETI domain decomposition method, *Computer methods in applied mechanics and engineering*, vol. **115**, no. 3-4, pp. 365–385, 1994b.

Farhat, C. and Roux, F.X., A method of finite element tearing and interconnecting and its parallel solution algorithm, *International journal for numerical methods in engineering*, vol. **32**, no. 6, pp. 1205–1227, 1991.

Farhat, C. and Roux, F.X., Implicit parallel processing in structural mechanics, *Comp. Mech. Advances*, vol. **2**, pp. 1–124, 1994.

Fragakis, Y. and Papadrakakis, M., The mosaic of high performance domain decomposition methods for structural mechanics: Formulation, interrelation and numerical efficiency of primal and dual methods, *Computer methods in applied mechanics and engineering*, vol. **192**, no. 35-36, pp. 3799–3830, 2003.

Fragakis, Y. and Papadrakakis, M., The mosaic of high-performance domain decomposition methods for structural mechanics–Part II: Formulation enhancements, multiple right-hand sides and implicit dynamics, *Computer methods in applied mechanics and engineering*, vol. **193**, no. 42-44, pp. 4611–4662, 2004.

Gear, C.W., Numerical initial value problems in ordinary differential equations, *Prentice-Hall series in automatic computation*, 1971.

Glusa, C., Boman, E.G., Chow, E., Rajamanickam, S., and Szyld, D.B., Scalable asynchronous domain decomposition solvers, *SIAM Journal on Scientific Computing*, vol. **42**, no. 6, pp. C384–C409, 2020.

Golbabai, A. and Javidi, M., A spectral domain decomposition approach for the generalized burger's–fisher equation, *Chaos, Solitons & Fractals*, vol. **39**, no. 1, pp. 385–392, 2009.

Gravouil, A. and Combescure, A., Multi-time-step explicit–implicit method for non-linear structural dynamics, *International Journal for Numerical Methods in Engineering*, vol. **50**, no. 1, pp. 199–225, 2001.

Gravouil, A., Combescure, A., and Brun, M., Heterogeneous asynchronous time integrators for computational structural dynamics, *International Journal for Numerical Methods in Engineering*, vol. **102**, no. 3-4, pp. 202–232, 2015.

Hilber, H.M., Hughes, T.J., and Taylor, R.L., Improved numerical dissipation for time integration algorithms in

structural dynamics, *Earthquake Engineering & Structural Dynamics*, vol. **5**, no. 3, pp. 283–292, 1977.

Hughes, T.J., *The finite element method: linear static and dynamic finite element analysis*, Prentice Hall, 1987.

Hughes, T.J. and Liu, W., Implicit-explicit finite elements in transient analysis: implementation and numerical examples, *Journal of Applied Mechanics*, vol. **45**, no. 2, pp. 375–378, 1978a.

Hughes, T.J. and Liu, W., Implicit-explicit finite elements in transient analysis: stability theory, *Journal of Applied Mechanics*, vol. **45**, no. 2, pp. 371–374, 1978b.

Jamal, M.H., Prakash, A., and Kulkarni, M., Exploiting semantics of temporal multi-scale methods to optimize multi-level mesh partitioning, *International Journal for Numerical Methods in Engineering*, vol. **112**, no. 1, pp. 58–85, 2017.

Jansen, K.E., Whiting, C.H., and Hulbert, G.M., A generalized-α method for integrating the filtered navier–stokes equations with a stabilized finite element method, *Computer Methods in Applied Mechanics and Engineering*, vol. **190**, no. 3-4, pp. 305–319, 2000.

Javidi, M. and Golbabai, A., A new domain decomposition algorithm for generalized burger's–huxley equation based on chebyshev polynomials and preconditioning, *Chaos, Solitons & Fractals*, vol. **39**, no. 2, pp. 849–857, 2009.

Ji, Y. and Xing, Y., An optimized three-sub-step composite time integration method with controllable numerical dissipation, *Computers & Structures*, vol. **231**, p. 106210, 2020.

Kadapa, C., Dettmer, W., and Perić, D., On the advantages of using the first-order generalised-alpha scheme for structural dynamic problems, *Computers & Structures*, vol. **193**, pp. 226–238, 2017.

Keyes, D., How scalable is domain decomposition in practice, *Proceedings of the 11th International Conference on Domain Decomposition Methods*, Citeseer, pp. 286–297, 1998.

Kim, K.T. and Bathe, K.J., Accurate solution of wave propagation problems in elasticity, *Computers & Structures*, vol. **249**, p. 106502, 2021.

Kim, W., An improved implicit method with dissipation control capability: The simple generalized composite time integration algorithm, *Applied Mathematical Modelling*, vol. **81**, pp. 910–930, 2020.

Kim, W. and Choi, S.Y., An improved implicit time integration algorithm: The generalized composite time integration algorithm, *Computers & Structures*, vol. **196**, pp. 341–354, 2018.

Kim, W. and Reddy, J., An improved time integration algorithm: A collocation time finite element approach, *International Journal of Structural Stability and Dynamics*, vol. **17**, no. 02, p. 1750024, 2017.

Kutta, W., Beitrag zur naherungsweisen integration totaler differentialgleichungen, *Z. Math. Phys.*, vol. **46**, pp. 435–453, 1901.

Kwon, S.B., Bathe, K.J., and Noh, G., An analysis of implicit time integration schemes for wave propagations, *Computers & Structures*, vol. **230**, p. 106188, 2020.

Kwon, S.B., Bathe, K.J., and Noh, G., Selecting the load at the intermediate time point of the ρ_∞-Bathe time integration scheme, *Computers & Structures*, vol. **254**, p. 106559, 2021.

Kwon, S.B. and Lee, J.M., A non-oscillatory time integration method for numerical simulation of stress wave propagations, *Computers & Structures*, vol. **192**, pp. 248–268, 2017.

Li, J., Li, H., Lian, Y., Zhao, R., and Yu, K., A suite of second-order composite sub-step explicit algorithms with controllable numerical dissipation and maximal stability bounds, *Applied Mathematical Modelling*, vol. **114**, pp. 601–626, 2023.

Li, J. and Yu, K., An alternative to the Bathe algorithm, *Applied Mathematical Modelling*, vol. **69**, pp. 255–272, 2019.

Li, J., Yu, K., and Tang, H., Further assessment of three Bathe algorithms and implementations for wave propagation problems, *International Journal of Structural Stability and Dynamics*, vol. **21**, no. 05, p. 2150073, 2021.

Liang, S., Zhang, J., Liu, X.Z., Hu, X.D., and Yuan, W., Domain decomposition based exponential time differencing method for fluid dynamics problems with smooth solutions, *Computers & Fluids*, vol. **194**, p. 104307, 2019.

Liu, W.K. and Belytschko, T., Mixed-time implicit-explicit finite elements for transient analysis, *Computers & Structures*, vol. **15**, no. 4, pp. 445–450, 1982.

Mahjoubi, N., Gravouil, A., Combescure, A., and Greffet, N., A monolithic energy conserving method to couple heterogeneous time integrators with incompatible time steps in structural dynamics, *Computer Methods in Applied Mechanics and Engineering*, vol. **200**, no. 9-12, pp. 1069–1086, 2011.

Malakiyeh, M.M., Shojaee, S., and Bathe, K.J., The Bathe time integration method revisited for prescribing desired numerical dissipation, *Computers & Structures*, vol. **212**, pp. 289–298, 2019.

Moulton, F.R., *New methods in exterior ballistics*, University of Chicago Press, 1926.

Nakshatrala, K.B., Hjelmstad, K.D., and Tortorelli, D.A., A feti-based domain decomposition technique for time-dependent first-order systems based on a dae approach, *International Journal for Numerical Methods in Engineering*, vol. **75**, no. 12, pp. 1385–1415, 2008.

Nakshatrala, P.B., Nakshatrala, K.B., and Tortorelli, D.A., A time-staggered partitioned coupling algorithm for transient heat conduction, *International Journal for Numerical Methods in Engineering*, vol. **78**, no. 12, pp. 1387–1406, 2009.

Newmark, N.M., A method of computation for structural dynamics, *Journal of the engineering mechanics division*, vol. **85**, no. 3, pp. 67–94, 1959.

Noh, G. and Bathe, K.J., Further insights into an implicit time integration scheme for structural dynamics, *Computers & Structures*, vol. **202**, pp. 15–24, 2018.

Noh, G. and Bathe, K.J., The Bathe time integration method with controllable spectral radius: The ρ_∞-Bathe method, *Computers & Structures*, vol. **212**, pp. 299–310, 2019a.

Noh, G. and Bathe, K.J., For direct time integrations: A comparison of the Newmark and ρ_∞-Bathe schemes, *Computers & Structures*, vol. **225**, p. 106079, 2019b.

Noh, G. and Bathe, K.J., Imposing displacements in implicit direct time integration & a patch test, *Advances in Engineering Software*, vol. **175**, p. 103286, 2023.

Noh, G., Ham, S., and Bathe, K.J., Performance of an implicit time integration scheme in the analysis of wave propagations, *Computers & Structures*, vol. **123**, pp. 93–105, 2013.

Park, K., An improved stiffly stable method for direct integration of nonlinear structural dynamic equations, *Journal of Applied Mechanics*, vol. **42**, no. 2, pp. 464–470, 1975.

Park, K., Partitioned transient analysis procedures for coupled-field problems: stability analysis, *Journal of Applied Mechanics*, vol. **47**, no. 2, pp. 370–376, 1980.

Prakash, A. and Hjelmstad, K.D., A FETI-based multi-time-step coupling method for Newmark schemes in structural dynamics, *International Journal for Numerical Methods in Engineering*, vol. **61**, no. 13, pp. 2183–2204, 2004.

Prakash, A., Taciroglu, E., and Hjelmstad, K.D., Computationally efficient multi-time-step method for partitioned

time integration of highly nonlinear structural dynamics, *Computers & Structures*, vol. **133**, pp. 51–63, 2014.

Robinson, B., da Costa, L., Poirel, D., Pettit, C., Khalil, M., and Sarkar, A., Aeroelastic oscillations of a pitching flexible wing with structural geometric nonlinearities: Theory and numerical simulation, *Journal of Sound and Vibration*, vol. **484**, p. 115389, 2020.

Runge, C., Über die numerische auflösung von differentialgleichungen, *Mathematische Annalen*, vol. **46**, no. 2, pp. 167–178, 1895.

Semler, C., Gentleman, W., and Paıdoussis, M., Numerical solutions of second order implicit non-linear ordinary differential equations, *Journal of Sound and Vibration*, vol. **195**, no. 4, pp. 553–574, 1996.

Shao, H. and Cai, C., The direct integration three-parameters optimal schemes for structural dynamics, *Proceeding of the international conference: Machine dynamics and engineering applications*, Xi'an Jiaotong University Press, pp. C16–C20, 1988.

Smolinski, P., An explicit multi-time step integration method for second order equations, *Computer methods in applied mechanics and engineering*, vol. **94**, no. 1, pp. 25–34, 1992.

Toselli, A. and Widlund, O., *Domain decomposition methods-algorithms and theory*, Vol. 34, Springer Science & Business Media, 2006.

Wang, Y., Xue, X., Zhang, T., Dai, Q., Liu, Y., Xie, N., Mei, S., Zhang, X., and Tamma, K.K., Overview and novel insights into implicit/explicit composite time integration type methods—fall under the rk: No ifs, ands, or buts, *Archives of Computational Methods in Engineering*, vol. **30**, pp. 3891–3940, 2023.

Wanner, G. and Hairer, E., *Solving ordinary differential equations II*, Vol. 375, Springer Berlin Heidelberg New York, 1996.

Zhang, H., Zhang, R., Xing, Y., and Masarati, P., On the optimization of n-sub-step composite time integration methods, *Nonlinear Dynamics*, vol. **102**, no. 3, pp. 1939–1962, 2020.

Zhang, J., A-stable two-step time integration methods with controllable numerical dissipation for structural dynamics, *International Journal for Numerical Methods in Engineering*, vol. **121**, no. 1, pp. 54–92, 2020.

Zhou, X. and Tamma, K.K., Design, analysis, and synthesis of generalized single step single solve and optimal algorithms for structural dynamics, *International Journal for Numerical Methods in Engineering*, vol. **59**, no. 5,

pp. 597–668, 2004.

Zienkiewicz, O.C. and Taylor, R.L., *The finite element method for solid and structural mechanics*, Elsevier, 2005.

TABLE 1: ρ_∞-Bathe parameters and their characteristics

ρ_∞	γ	Characteristics
0	0.5 or γ_0	Standard Bathe scheme. Dissipative scheme with low dispersion. As $\Delta t \to \infty$, spectral radius, $\rho \to 0$. Used for stiff-flexible systems and wave propagation problems with CFL = 1.0 and a consistent mass matrix.
1	γ_0 (= 0.5)	Non-dissipative scheme. As $\Delta t \to \infty$, spectral radius, $\rho \to 1$. Gives spurious oscillations for stiff-flexible systems.
0.65	γ_0	Dissipative scheme with low dispersion. As $\Delta t \to \infty$, spectral radius, $\rho \to 0.65$. Used for wave propagation problems with a consistent mass matrix. Maximizes CFL number (1.25).
$1 - \sqrt{3}$	1.3	Large numerical dissipation. May be used for wave propagation problems with CFL = 1.5 and a lumped mass matrix.

TABLE 2: Parameters chosen for the MTS-Bathe method to solve the split SDOF problem

	$(\rho_\infty^A, \rho_\infty^B, \gamma^A, \gamma^B)$	Accuracy of underlying UTS-Bathe
MTS-Bathe 1	$(0, 0, \gamma_0^A, \gamma_0^B)$	2nd-order
MTS-Bathe 2	$(1, 1, 0.5, 0.5)$	2nd-order
MTS-Bathe 3	$(1-\sqrt{3}, 1-\sqrt{3}, \gamma_p^A, \gamma_p^B)$	3rd-order
MTS-Bathe 4	$(1, 0, 0.5, \gamma_0^B)$	2nd-order

TABLE 3: Computational costs and number of iterations in the duration $[0,\ 10]$ in the Duffing MDOF system

Method	$\Delta T = 0.3$				$\Delta T = 0.05$			
	Block time-step	Computational time (sec)	Number of iterations	Maximum error (%)	Block time-step	Computational time (sec)	Number of iterations	Maximum error (%)
MTS-TR	0.15	0.178	161	9.26	0.025	0.586	755	0.65
MTS-Bathe	0.30	0.234	92	2.48	0.050	0.712	400	0.43

List of Figures

1 Stiff-flexible system decomposed into subdomains and solved with multi-time-step method. 62

2 Classification of uniform time-step (UTS) methods. 63

3 Representation of two sub-steps for the UTS-ρ_∞-Bathe method. 64

4 Representation of two different time-steps for the MTS-Bathe method. 65

5 Flowchart of the proposed MTS-Bathe method 66

6 Spectral radius of the MTS-Bathe method with $\rho_\infty^A = \rho_\infty^B = 0$ (γ-Bathe) for various values of γ^A and γ^B with time-step ratio $m = 1$ and $m = 2$ without damping and $\omega_0^B/\omega_0^A = 1$ 67

7 LTEs using the proposed MTS method for the γ-Bathe scheme with $\gamma^A = \gamma^B = 2 - \sqrt{2}$ when $d_0 = v_0 = 1$, $\omega_0 = 2\pi$, $\zeta^A = 0.2$, and $\zeta^B = 0.1$. 68

8 LTEs using the proposed MTS method for the ρ_∞-Bathe scheme with $\rho_\infty^A = \rho_\infty^B = 1 - \sqrt{3}$ and $\gamma^A = \gamma^B = \gamma_p^A = \gamma_p^B$ when $d_0 = v_0 = 1$, $\omega_0 = 2\pi$, $\zeta^A = 0.2$, and $\zeta^B = 0.1$. 69

9 Accuracy analysis of the MTS-Bathe method for the γ-Bathe scheme for different values of γ^A and γ^B when $\omega_0^B/\omega_0^A = 1$. 70

10 Accuracy analysis of the MTS-TR method and MTS-Bathe methods. 71

11 Time history of (a) the velocities and (b) interface reactions using the MTS-TR and MTS-Bathe methods for the split SDOF problem. MTS-TR method uses a block time-step of $\Delta T = 4.87 \times 10^{-6}$ and the MTS-Bathe method uses a block time-step of $\Delta T = 9.74 \times 10^{-6}$ for two different time-step ratios: $m = 2, 5$. . . 72

12 Comparison of computational costs of the MTS-TR and MTS-Bathe methods for the split SDOF problem. Block time-step for the MTS-TR method is 4.87×10^{-6} and for the MTS-Bathe methods is 9.74×10^{-6}. 73

13 Global cumulative errors for the MTS-TR and MTS-Bathe methods for the split SDOF problem showing rates of convergence of these methods are 2 and 3. . . . 74

14 Time history and phase space diagram of displacement and velocity for MTS methods with $\Delta T = 0.5$ and $m = 6$. 75

15 Time history and Fourier spectrum of acceleration for MTS methods with $\Delta T = 0.5$ and $m = 6$ 76

16 Maximum global cumulative errors in MTS methods with time-step ratio $m = 6$. 77

17 3-DOF stiff-flexible system and its decomposition into subdomains Ω^A and Ω^B. . 78

18 Acceleration of nodes 2 and reaction of node 1 for various UTS and MTS methods when $m = 3$. Computational cost is 1.118, 1.177, 1.313, and 1.399 ms for UTS-TR, UTS-Bathe, MTS-TR, and MTS-Bathe methods, respectively. 79

19 Global cumulative errors in acceleration of nodes 2 and reaction of node 1 for various UTS and MTS methods when $m = 3$. The 16 points on each curve correspond to different time-step sizes $\Delta T \in [10^0, 10^{-3}]$ at intervals of $\log_{10} \Delta T = 0.2$ with increasing computational costs from left to right. Time-steps for UTS- and MTS-TR methods and UTS- and MTS-Bathe methods are set as $\Delta T/2$ and ΔT, respectively. 80
20 2D bi-material cantilever beam problem. 81
21 Global cumulative errors for the UTS-TR, UTS-Bathe, MTS-TR, and MTS-Bathe methods with a time-step ratio of $m = 5$. The 6 points on each curve correspond to different $\Delta T \in [10^{-6}, 10^{-7}]$ at intervals of $\log_{10} \Delta T = 0.2$ with increasing computational costs from left to right. Time-steps for UTS- and MTS-TR methods are set as $\Delta T/2$ and those for UTS- and MTS-Bathe methods are set as ΔT for computational cost parity. 82
22 Normal stress in the x-direction σ_{xx} and deformation plots at $t = 2.4 \times 10^{-3}$ (Deformation scale factor is 5000). 83
23 Maximum local instantaneous errors for the normal stress in the x-direction σ_{xx} for various values of ΔT and $m = 1, 2, ..., 10$. The block time-step for MTS-TR and MTS-Bathe methods is set as $\Delta T/2$ and ΔT, respectively, for computational cost parity. 84
24 Maximum local instantaneous errors in displacement and velocity for MTS-TR and MTS-Bathe methods with time step ratios of $m = 2$ and 5. The 16 points on each curve correspond to different $\Delta T \in [10^{-3}, 10^{-6}]$ at intervals of $\log_{10} \Delta T = 0.2$ with increasing computational costs from left to right. The block time-step for MTS-TR method is set as $\Delta T/2$ and that for MTS-Bathe method is set as ΔT for computational cost parity. 85
25 Two-story shear building with two subdomains. 86
26 Time history of displacement, phase space diagram, and Poincaré section of the bottom story from the reference solution. Note that for phase space diagram and Poincaré section, we consider the simulation duration $[0, 100]$ and $[0, 4000]$, respectively. 87
27 Time history of displacement of the bottom story when $m = 10$. Block time-step ΔT for MTS-Bathe method is taken to be twice that of MTS-TR method. 88
28 Phase space diagram of the bottom story in subdomain Ω^B when $m = 10$. 89
29 Fourier spectrum of displacement of the bottom story when $m = 10$. 90
30 Decomposition of a MDOF Duffing system into stiff (Ω^B) and flexible (Ω^A) parts. 91
31 Phase plane diagrams at nodes 5 and 12 with $m = 6$. 92
32 Fourier spectrum of acceleration at nodes 5 and 12 with $m = 6$. 93
33 Time history of acceleration at nodes 5 and 12 with $m = 6$. 94
34 Maximum value of global cumulative errors in displacement, velocity, and acceleration using the MTS-TR and MTS-Bathe methods when $m = 6$. The 4 points on each curve correspond to different $\Delta T = 0.3, 0.2, 0.1$, and 0.05 with increasing computational costs from left to right. 95

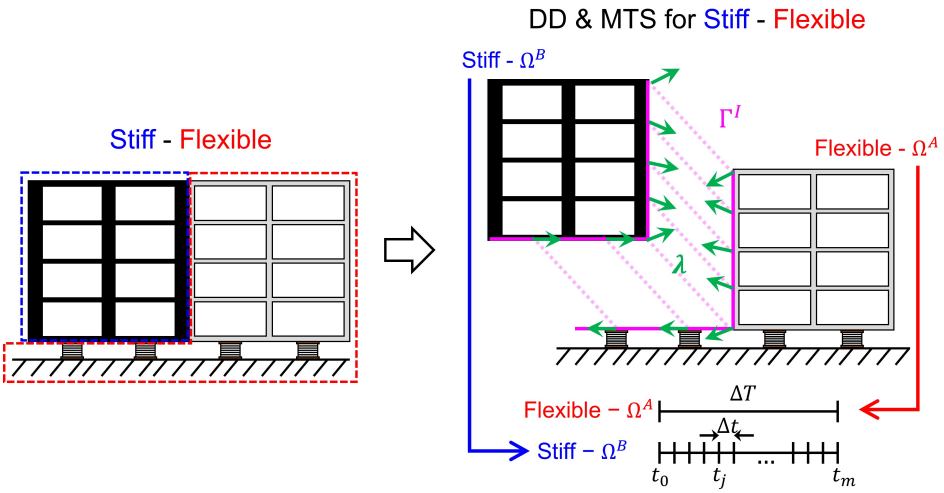

FIG. 1: Stiff-flexible system decomposed into subdomains and solved with multi-time-step method.

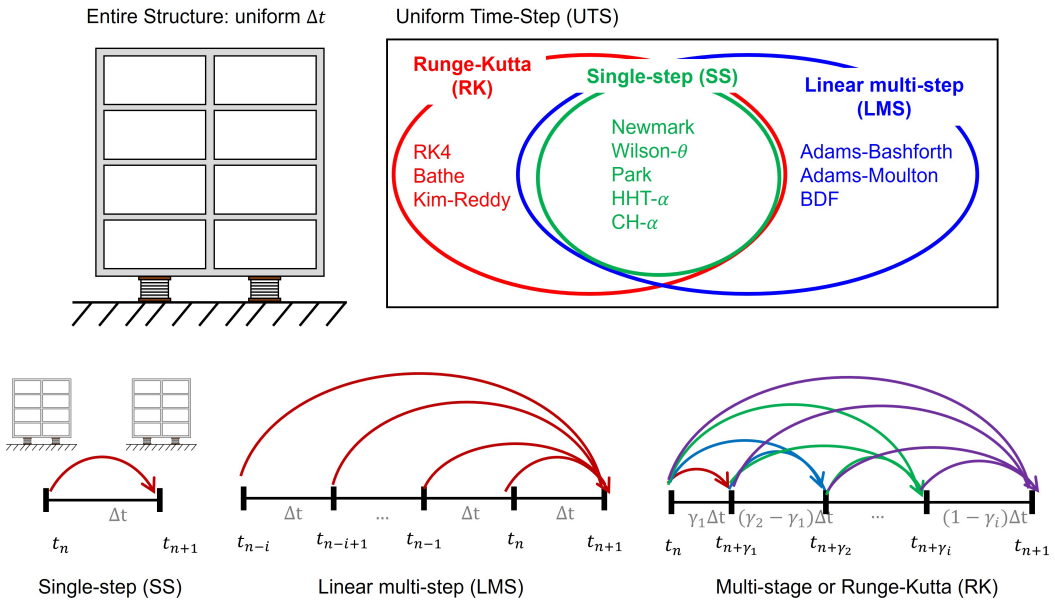

FIG. 2: Classification of uniform time-step (UTS) methods.

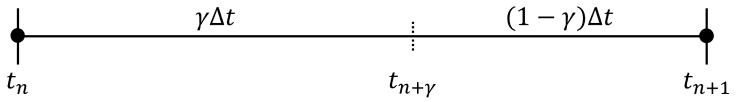

FIG. 3: Representation of two sub-steps for the UTS-ρ_∞-Bathe method.

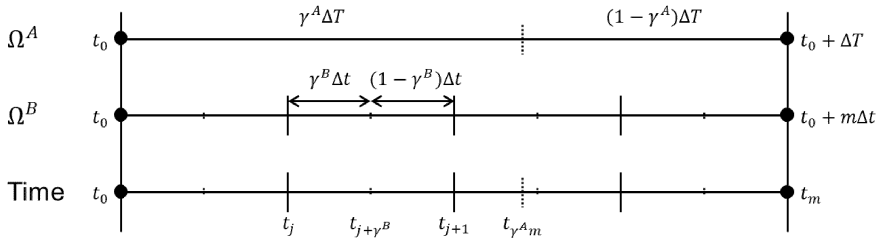

FIG. 4: Representation of two different time-steps for the MTS-Bathe method.

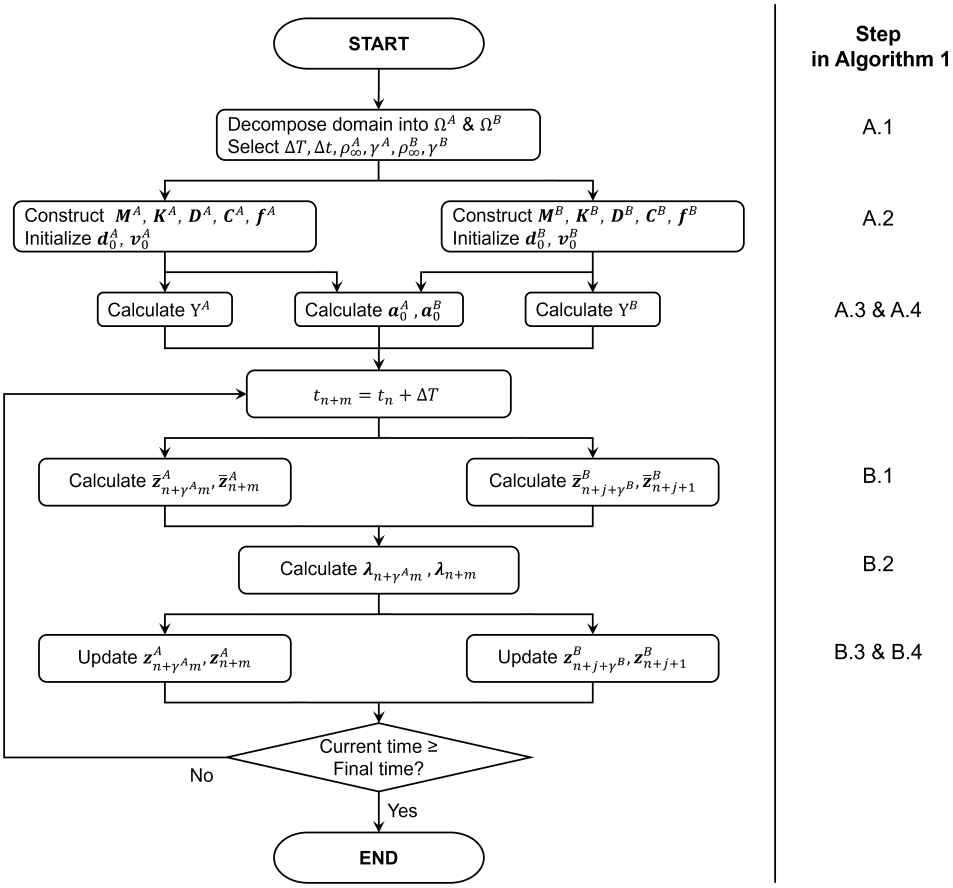

FIG. 5: Flowchart of the proposed MTS-Bathe method

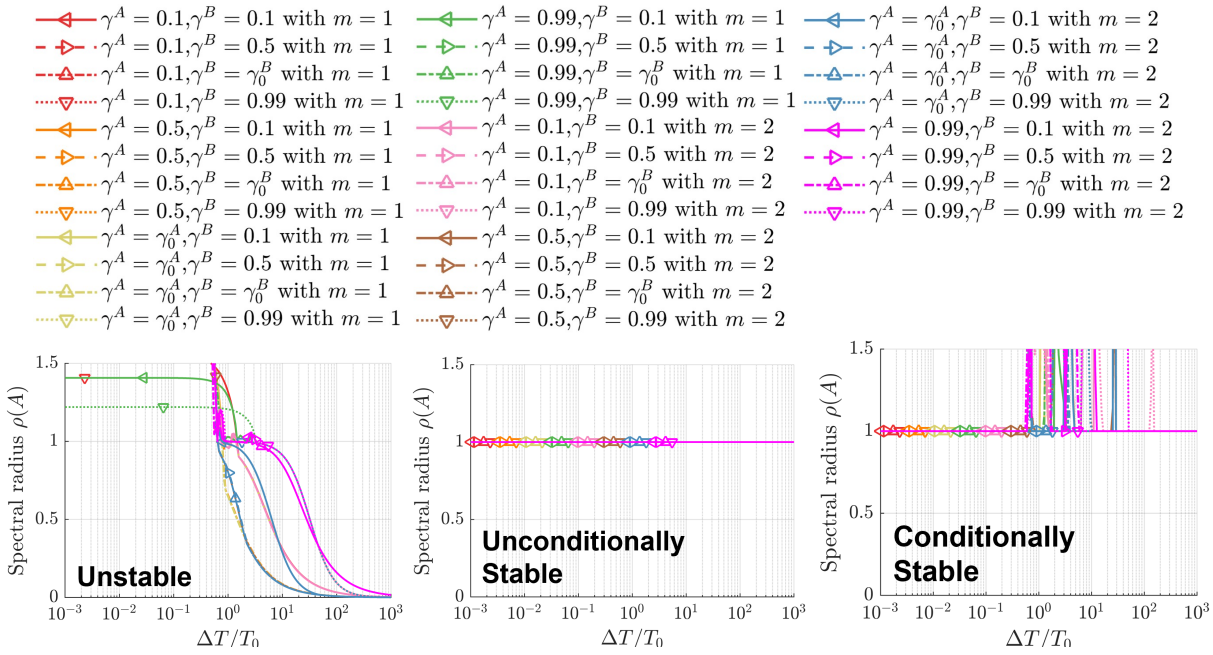

(a) Displacement continuity **(b)** Velocity continuity **(c)** Acceleration continuity

FIG. 6: Spectral radius of the MTS-Bathe method with $\rho_\infty^A = \rho_\infty^B = 0$ (γ-Bathe) for various values of γ^A and γ^B with time-step ratio $m = 1$ and $m = 2$ without damping and $\omega_0^B/\omega_0^A = 1$

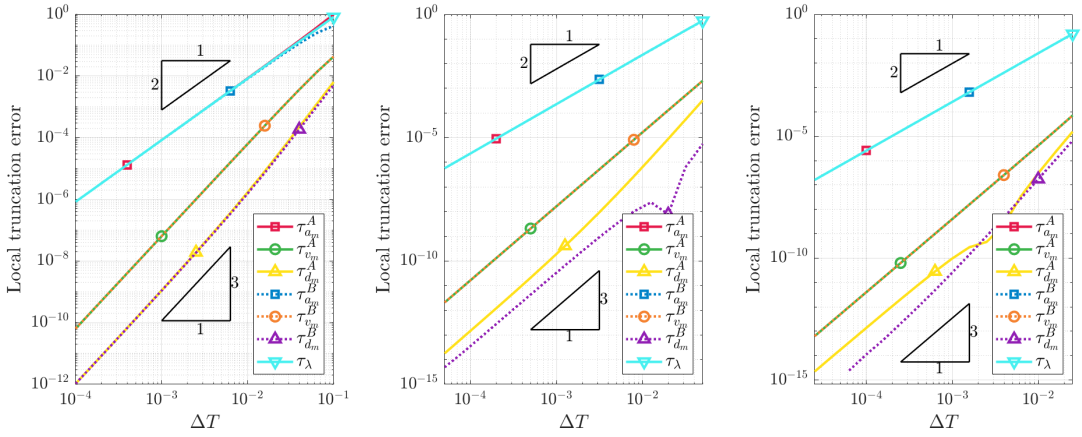

(a) $m = 1$ and $\omega_0^B/\omega_0^A = 2$ **(b)** $m = 2$ and $\omega_0^B/\omega_0^A = 10$ **(c)** $m = 4$ and $\omega_0^B/\omega_0^A = 10^3$

FIG. 7: LTEs using the proposed MTS method for the γ-Bathe scheme with $\gamma^A = \gamma^B = 2 - \sqrt{2}$ when $d_0 = v_0 = 1$, $\omega_0 = 2\pi$, $\zeta^A = 0.2$, and $\zeta^B = 0.1$.

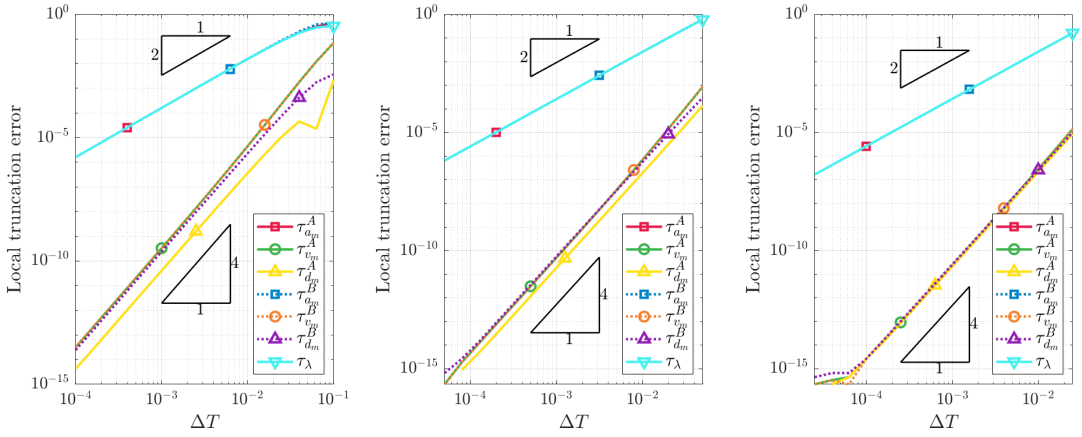

(a) $m = 1$ and $\omega_0^B/\omega_0^A = 2$ **(b)** $m = 2$ and $\omega_0^B/\omega_0^A = 10$ **(c)** $m = 4$ and $\omega_0^B/\omega_0^A = 10^3$

FIG. 8: LTEs using the proposed MTS method for the ρ_∞-Bathe scheme with $\rho_\infty^A = \rho_\infty^B = 1 - \sqrt{3}$ and $\gamma^A = \gamma^B = \gamma_p^A = \gamma_p^B$ when $d_0 = v_0 = 1$, $\omega_0 = 2\pi$, $\zeta^A = 0.2$, and $\zeta^B = 0.1$.

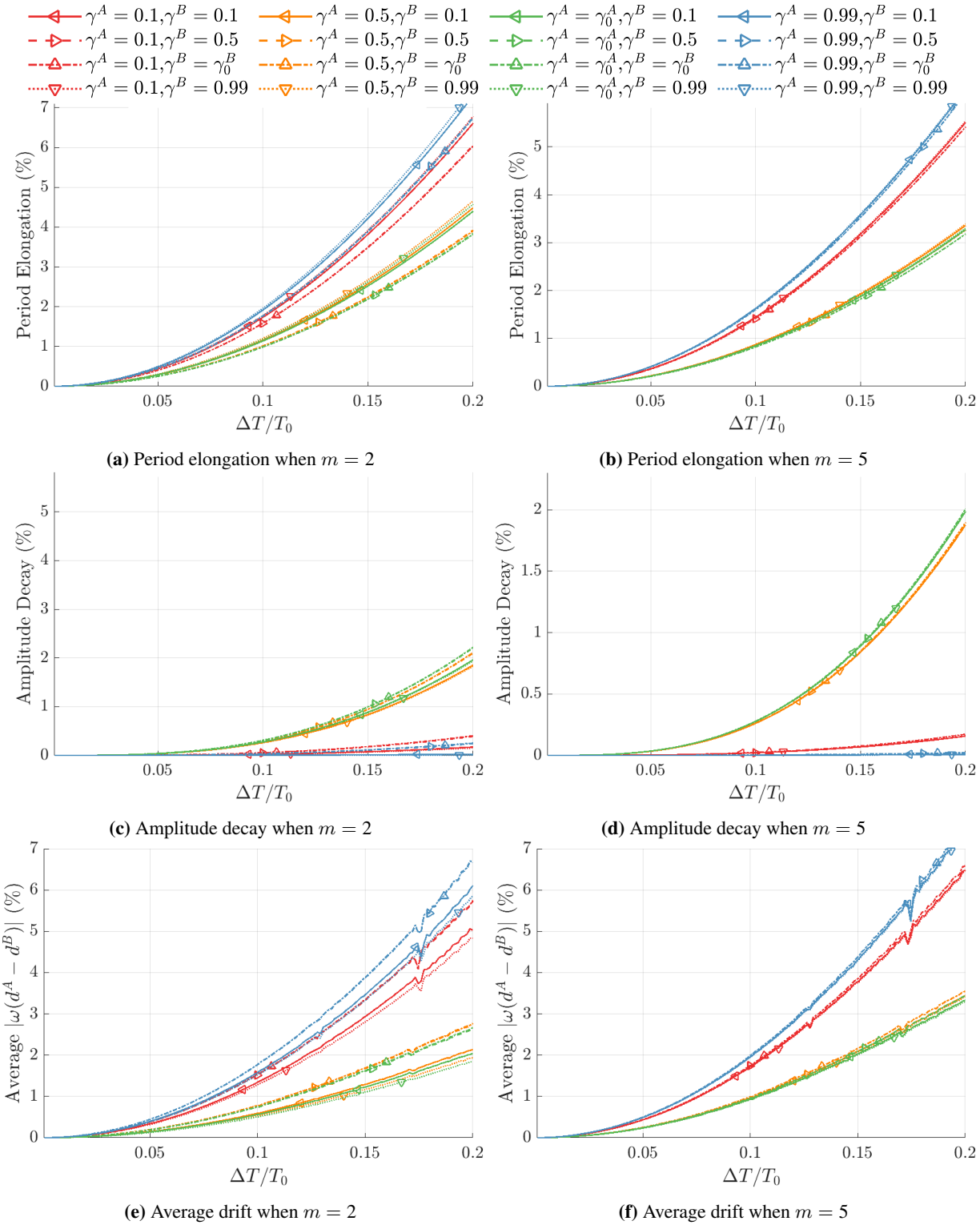

(a) Period elongation when $m = 2$

(b) Period elongation when $m = 5$

(c) Amplitude decay when $m = 2$

(d) Amplitude decay when $m = 5$

(e) Average drift when $m = 2$

(f) Average drift when $m = 5$

FIG. 9: Accuracy analysis of the MTS-Bathe method for the γ-Bathe scheme for different values of γ^A and γ^B when $\omega_0^B/\omega_0^A = 1$.

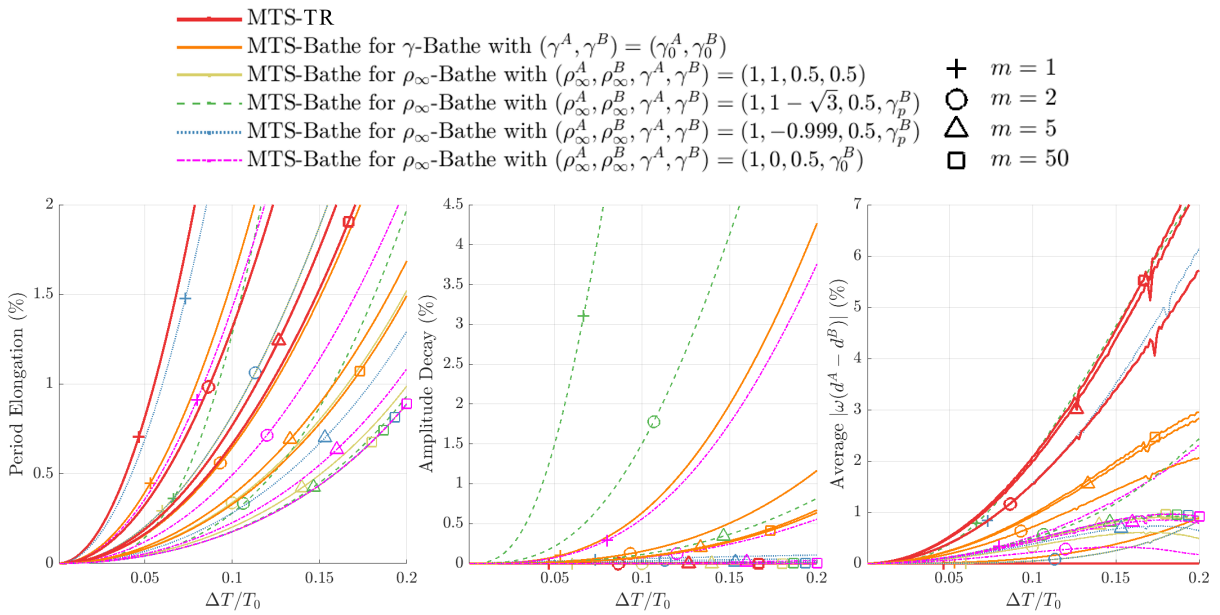

(a) $\omega_0^B/\omega_0^A = 2$

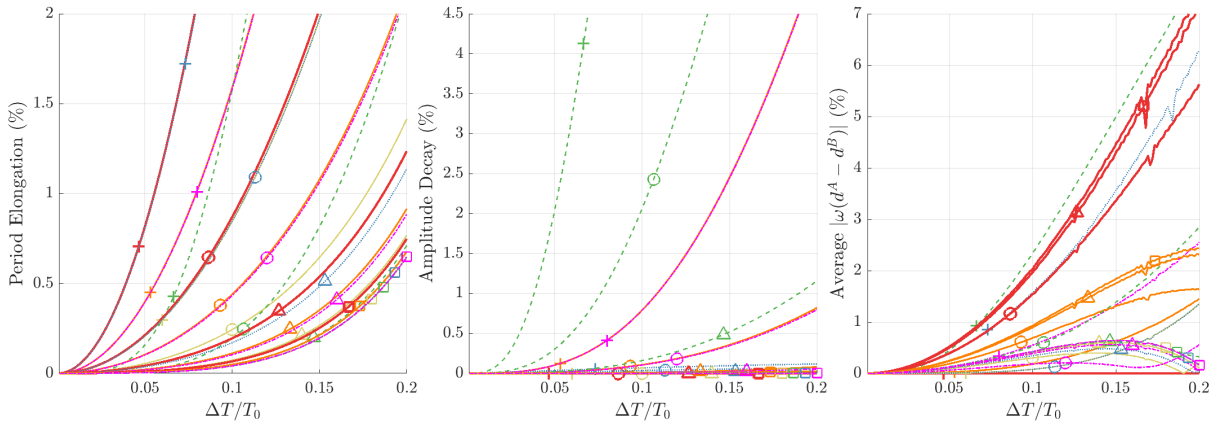

(b) $\omega_0^B/\omega_0^A = 10$

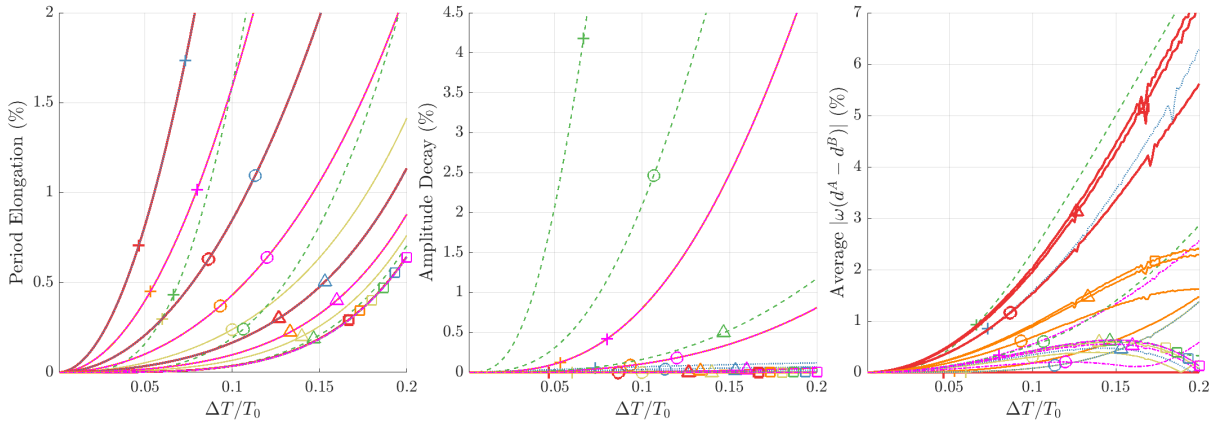

(c) $\omega_0^B/\omega_0^A = 100$

FIG. 10: Accuracy analysis of the MTS-TR method and MTS-Bathe methods.

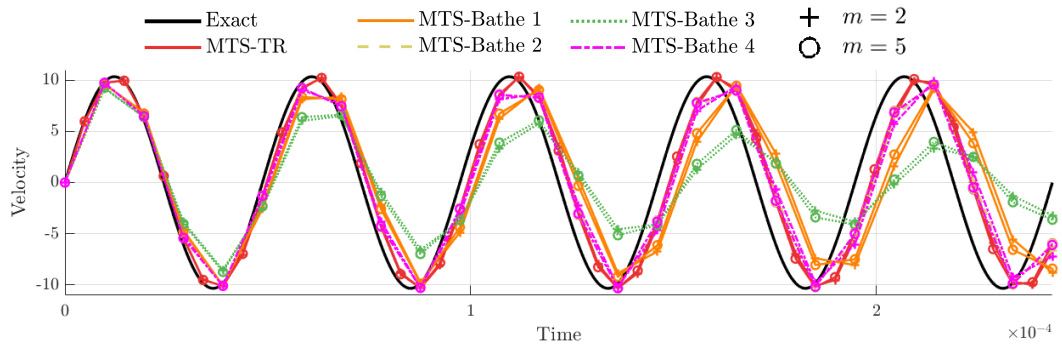

(a) Velocity

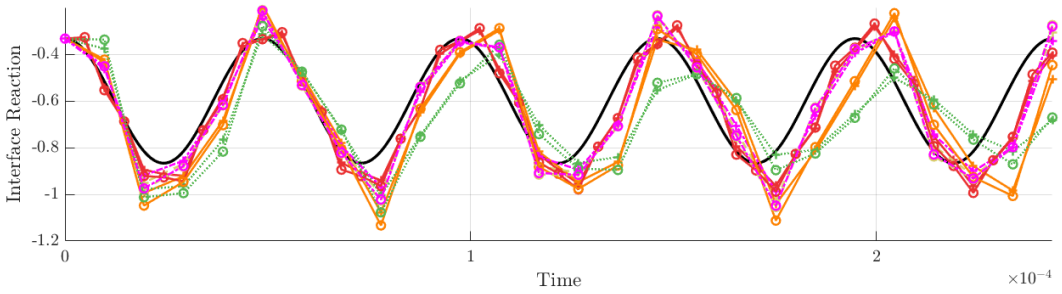

(b) Interface reaction

FIG. 11: Time history of (a) the velocities and (b) interface reactions using the MTS-TR and MTS-Bathe methods for the split SDOF problem. MTS-TR method uses a block time-step of $\Delta T = 4.87 \times 10^{-6}$ and the MTS-Bathe method uses a block time-step of $\Delta T = 9.74 \times 10^{-6}$ for two different time-step ratios: $m = 2,\ 5$.

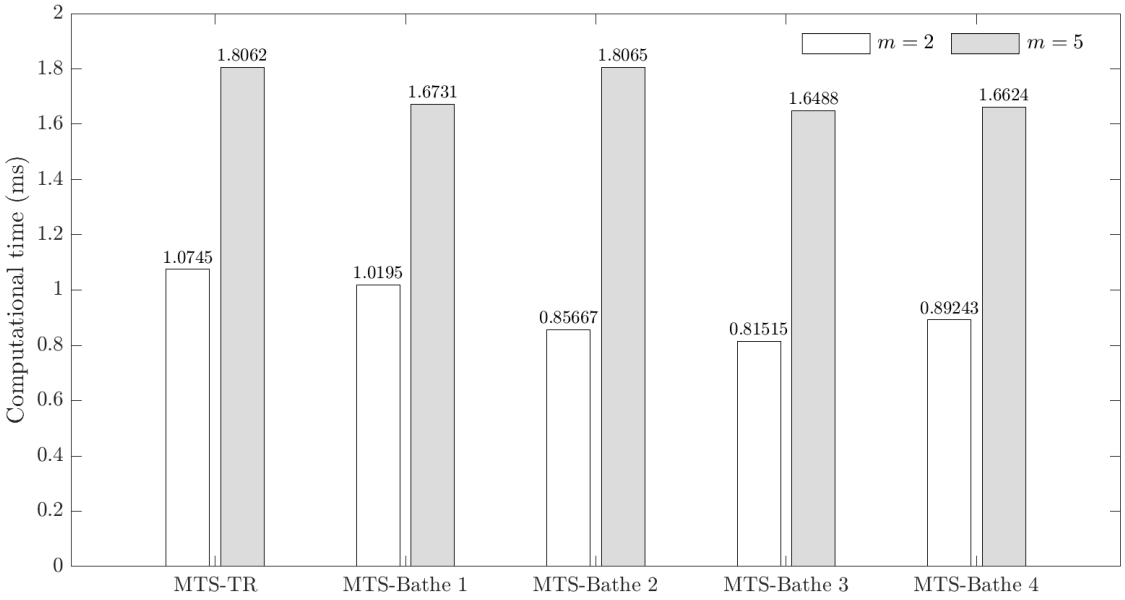

FIG. 12: Comparison of computational costs of the MTS-TR and MTS-Bathe methods for the split SDOF problem. Block time-step for the MTS-TR method is 4.87×10^{-6} and for the MTS-Bathe methods is 9.74×10^{-6}.

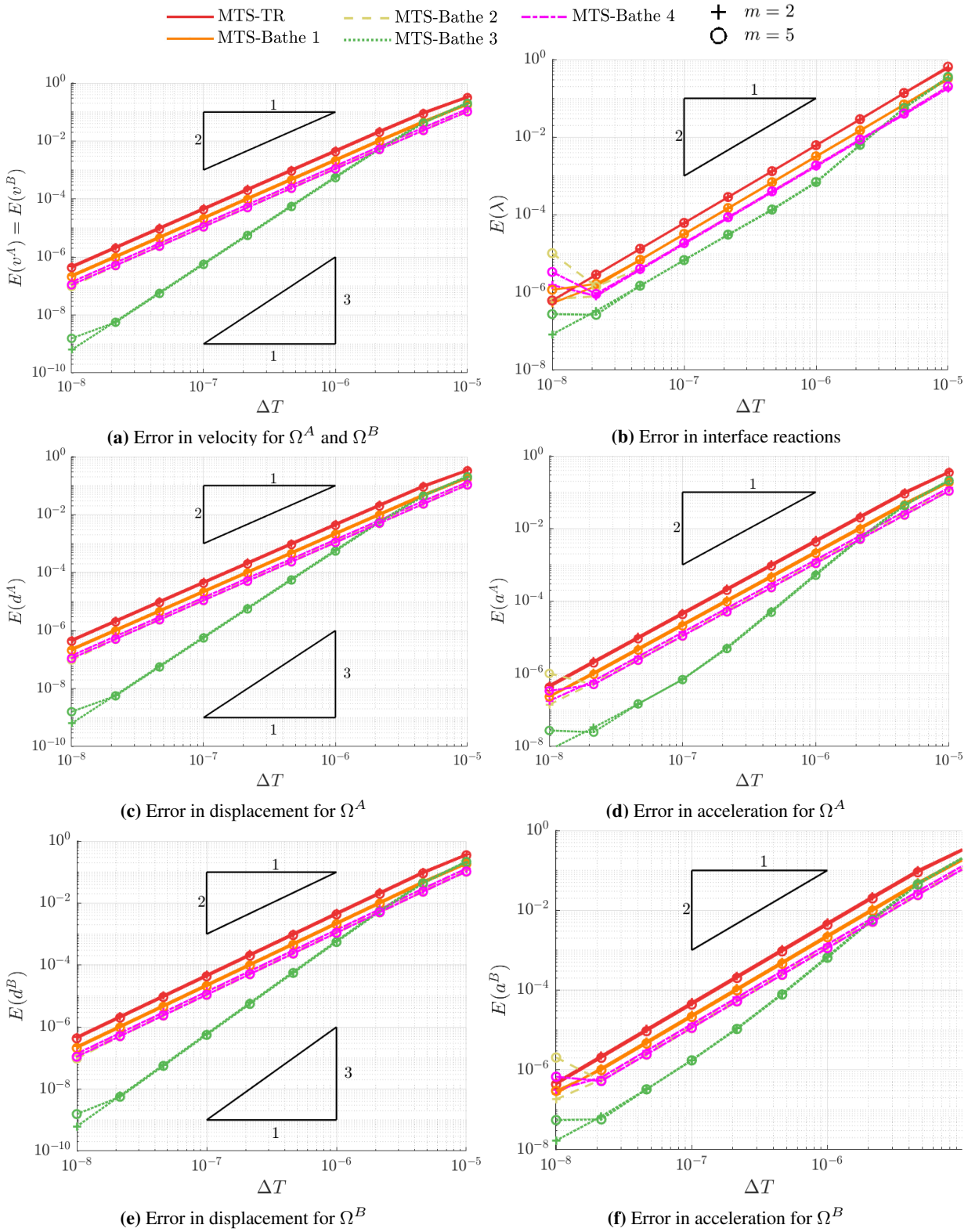

(a) Error in velocity for Ω^A and Ω^B

(b) Error in interface reactions

(c) Error in displacement for Ω^A

(d) Error in acceleration for Ω^A

(e) Error in displacement for Ω^B

(f) Error in acceleration for Ω^B

FIG. 13: Global cumulative errors for the MTS-TR and MTS-Bathe methods for the split SDOF problem showing rates of convergence of these methods are 2 and 3.

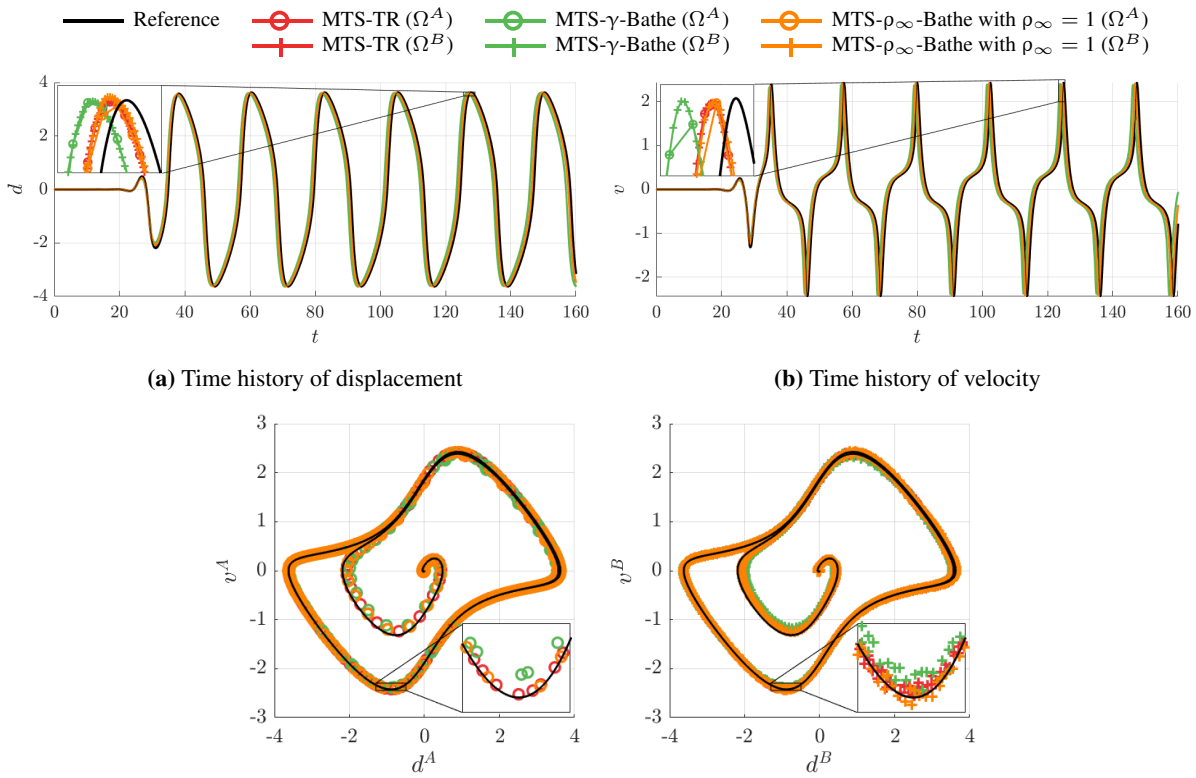

(a) Time history of displacement

(b) Time history of velocity

(c) Phase space diagram (displacement-velocity)

FIG. 14: Time history and phase space diagram of displacement and velocity for MTS methods with $\Delta T = 0.5$ and $m = 6$.

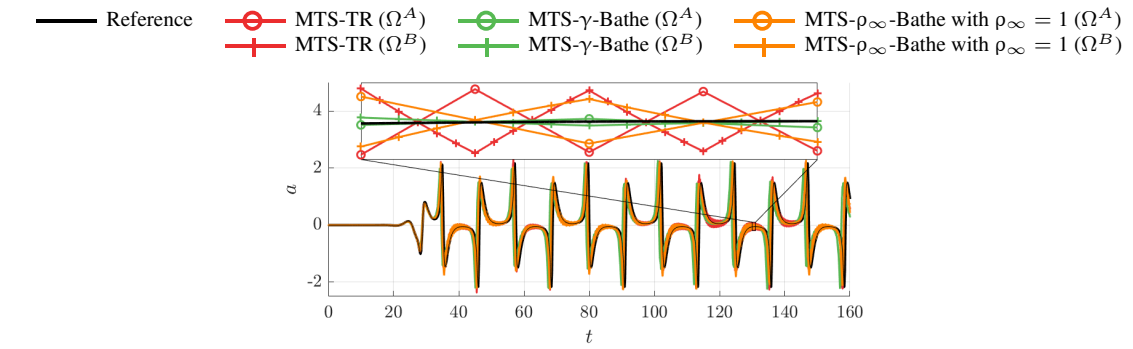

(a) Time history of acceleration

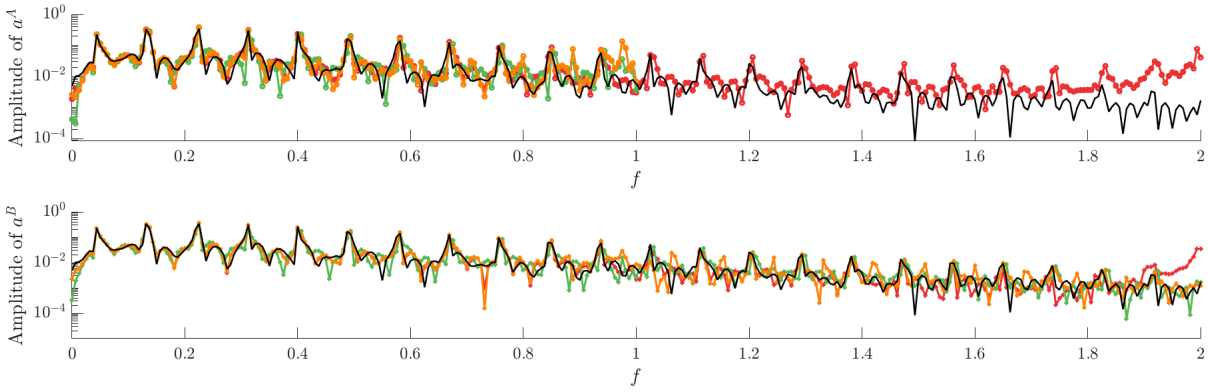

(b) Fourier spectrum of acceleration

FIG. 15: Time history and Fourier spectrum of acceleration for MTS methods with $\Delta T = 0.5$ and $m = 6$

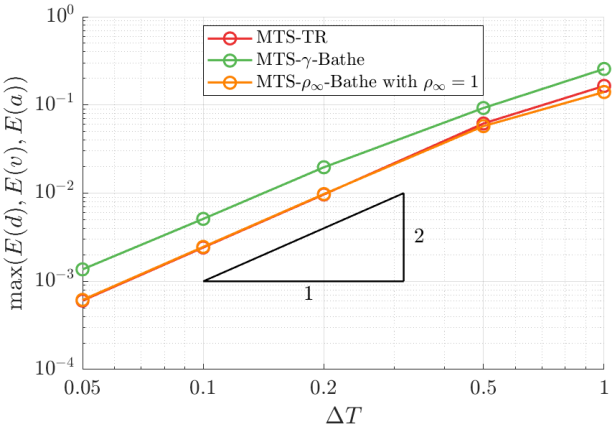

FIG. 16: Maximum global cumulative errors in MTS methods with time-step ratio $m = 6$.

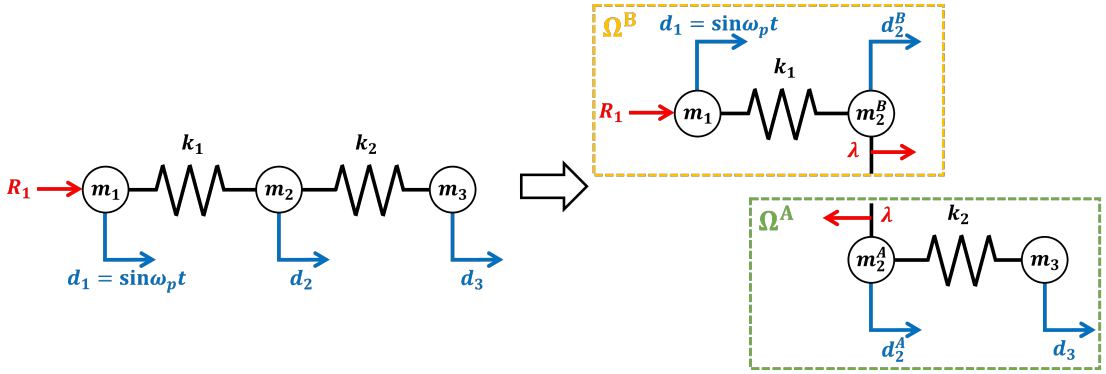

FIG. 17: 3-DOF stiff-flexible system and its decomposition into subdomains Ω^A and Ω^B.

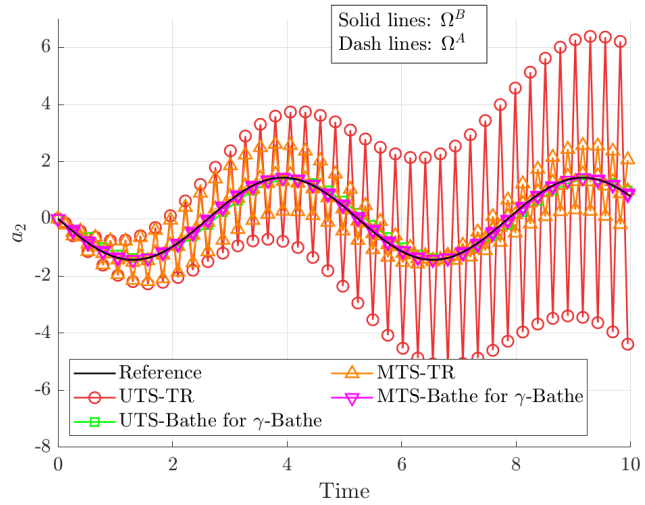

(a) Acceleration of node 2

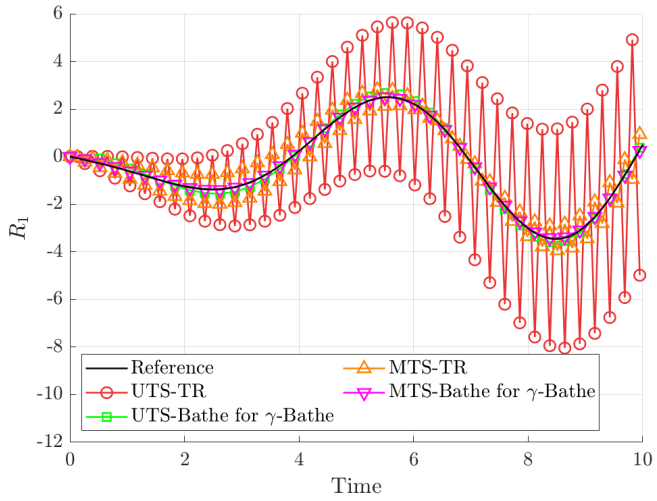

(b) Reaction of node 1

FIG. 18: Acceleration of nodes 2 and reaction of node 1 for various UTS and MTS methods when $m = 3$. Computational cost is 1.118, 1.177, 1.313, and 1.399 ms for UTS-TR, UTS-Bathe, MTS-TR, and MTS-Bathe methods, respectively.

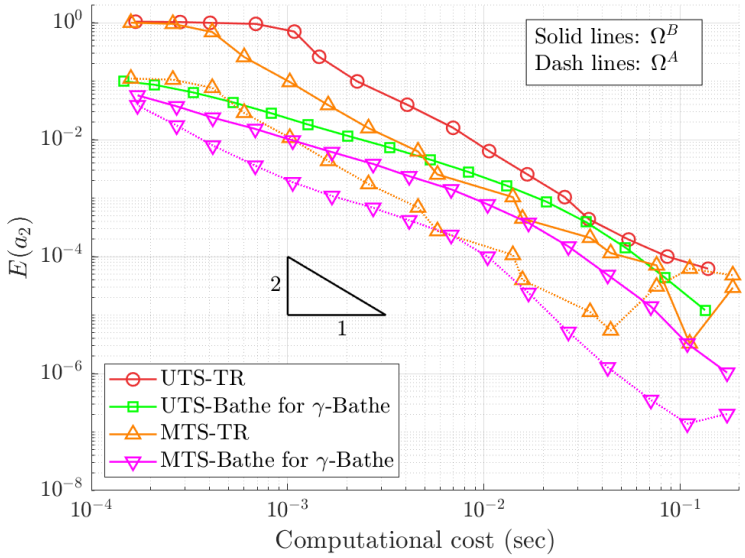

(a) Acceleration of node 2

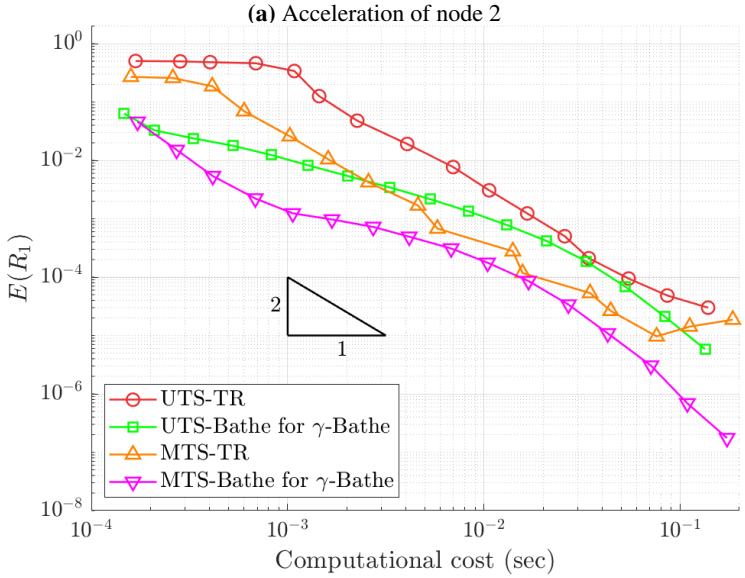

(b) Reaction of node 1

FIG. 19: Global cumulative errors in acceleration of nodes 2 and reaction of node 1 for various UTS and MTS methods when $m = 3$. The 16 points on each curve correspond to different time-step sizes $\Delta T \in [10^0, 10^{-3}]$ at intervals of $\log_{10} \Delta T = 0.2$ with increasing computational costs from left to right. Time-steps for UTS- and MTS-TR methods and UTS- and MTS-Bathe methods are set as $\Delta T/2$ and ΔT, respectively.

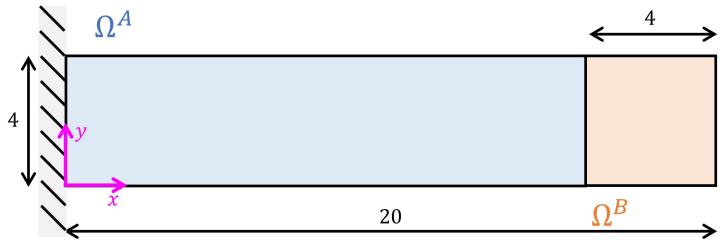

FIG. 20: 2D bi-material cantilever beam problem.

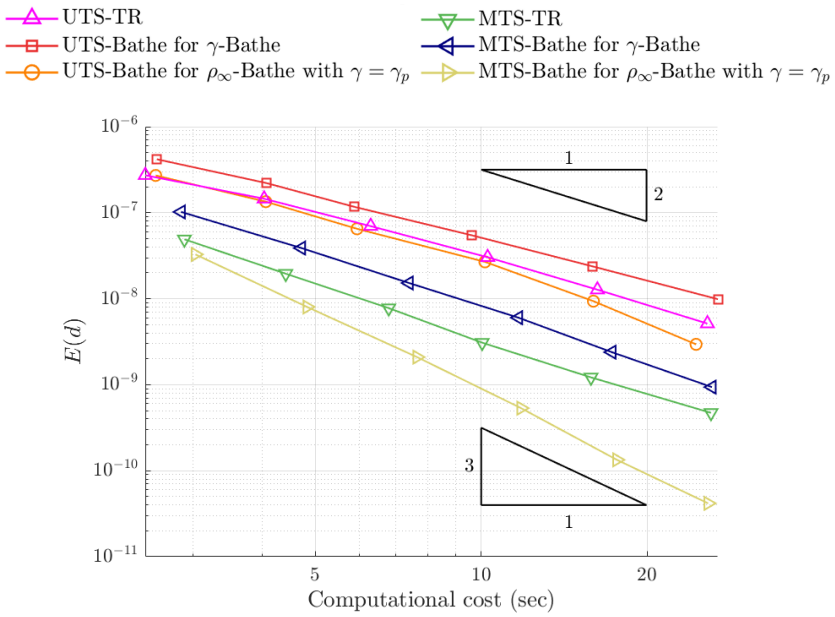

(a) Error in Displacement

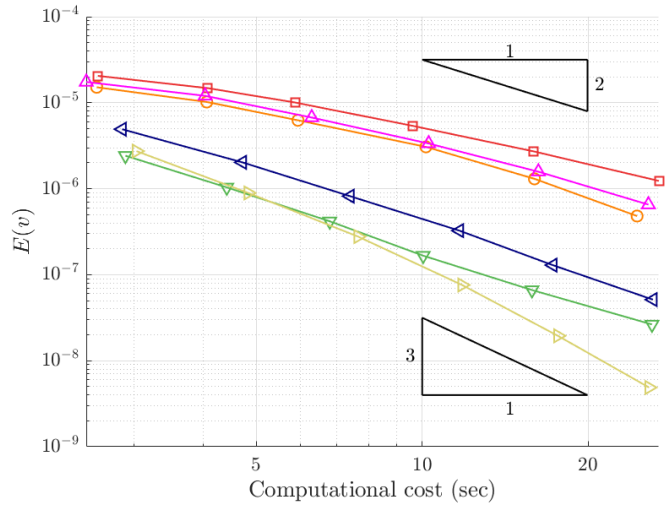

(b) Error in Velocity

FIG. 21: Global cumulative errors for the UTS-TR, UTS-Bathe, MTS-TR, and MTS-Bathe methods with a time-step ratio of $m = 5$. The 6 points on each curve correspond to different $\Delta T \in [10^{-6}, 10^{-7}]$ at intervals of $\log_{10} \Delta T = 0.2$ with increasing computational costs from left to right. Time-steps for UTS- and MTS-TR methods are set as $\Delta T/2$ and those for UTS- and MTS-Bathe methods are set as ΔT for computational cost parity.

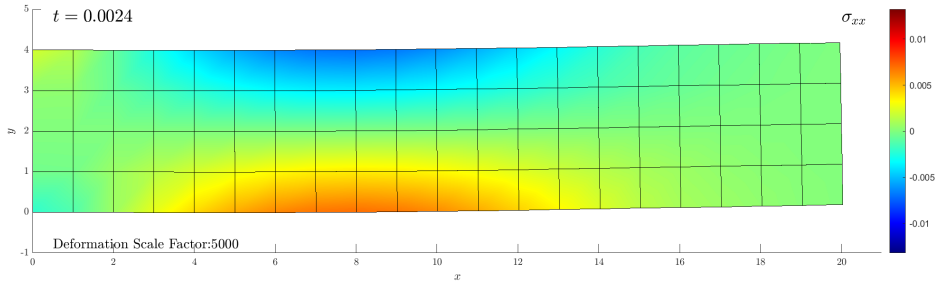

(a) Reference

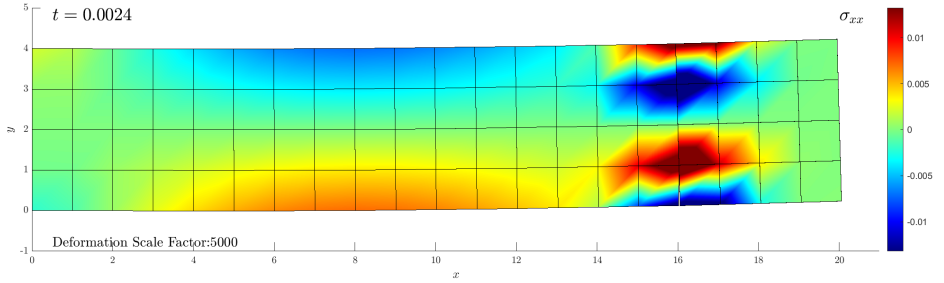

(b) MTS-TR method

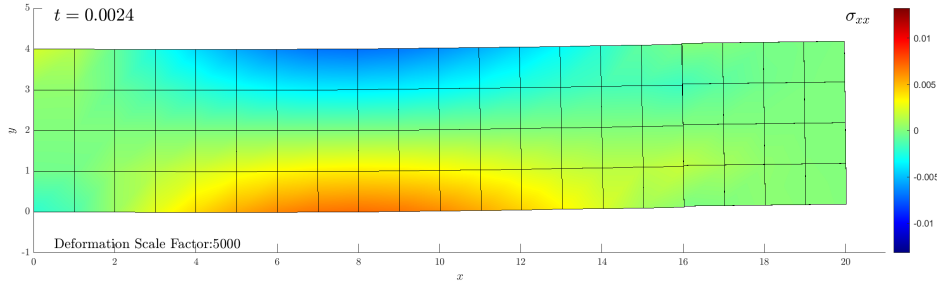

(c) MTS-Bathe method with $\rho_\infty = 0$

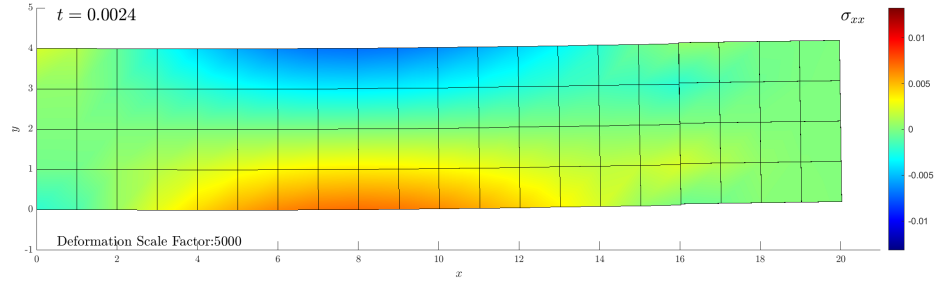

(d) MTS-Bathe method with $\rho_\infty = 0.65$

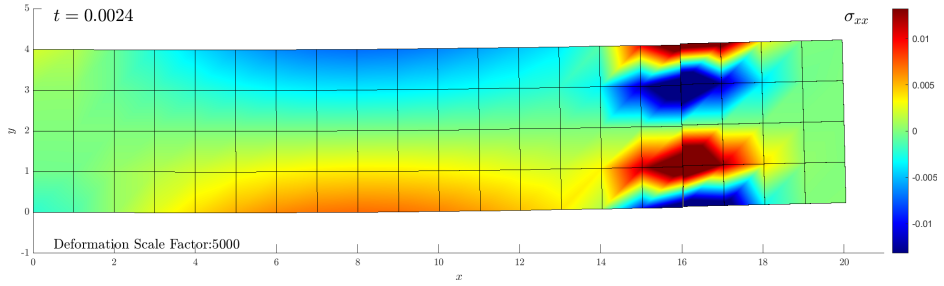

(e) MTS-Bathe method with $\rho_\infty = 1$

FIG. 22: Normal stress in the x-direction σ_{xx} and deformation plots at $t = 2.4 \times 10^{-3}$ (Deformation scale factor is 5000).

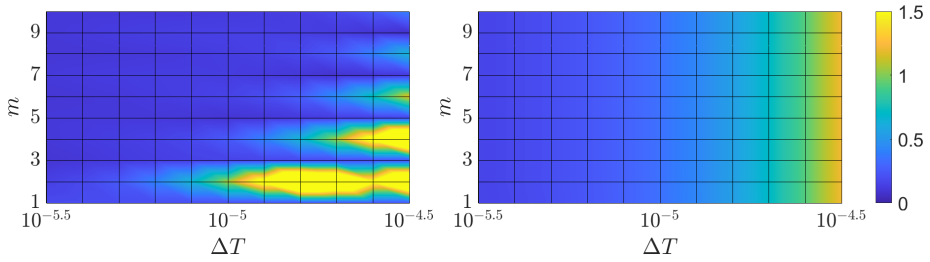

(a) MTS-TR **(b)** MTS-Bathe ($\rho_\infty = 0$)

FIG. 23: Maximum local instantaneous errors for the normal stress in the x-direction σ_{xx} for various values of ΔT and $m = 1, 2, ..., 10$. The block time-step for MTS-TR and MTS-Bathe methods is set as $\Delta T/2$ and ΔT, respectively, for computational cost parity.

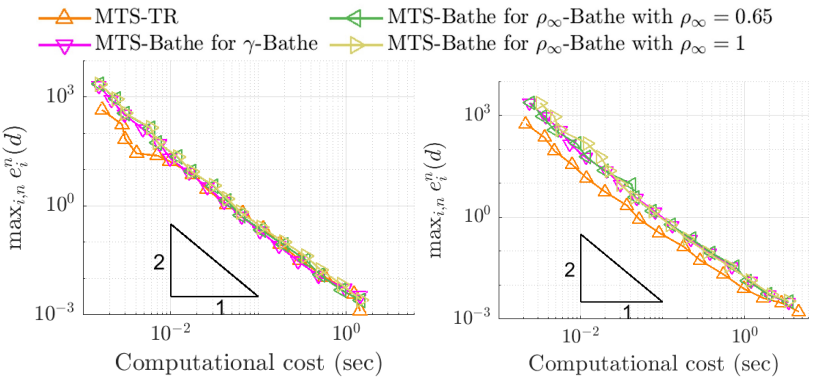

(a) Error in Displacement ($m = 2$)

(b) Error in Displacement ($m = 5$)

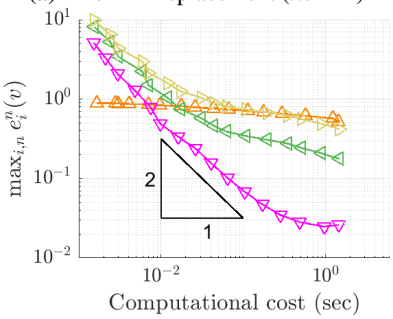

(c) Error in Velocity ($m = 2$)

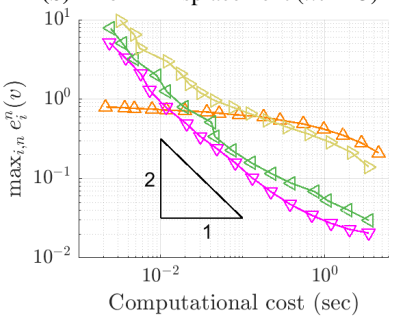

(d) Error in Velocity ($m = 5$)

FIG. 24: Maximum local instantaneous errors in displacement and velocity for MTS-TR and MTS-Bathe methods with time step ratios of $m = 2$ and 5. The 16 points on each curve correspond to different $\Delta T \in [10^{-3}, 10^{-6}]$ at intervals of $\log_{10} \Delta T = 0.2$ with increasing computational costs from left to right. The block time-step for MTS-TR method is set as $\Delta T/2$ and that for MTS-Bathe method is set as ΔT for computational cost parity.

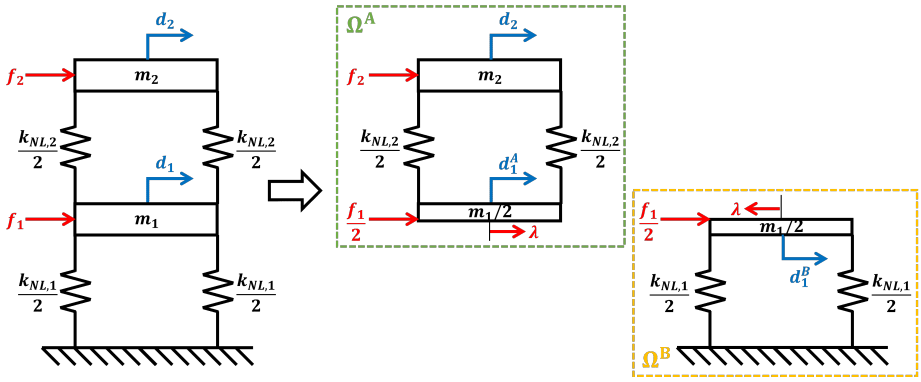

FIG. 25: Two-story shear building with two subdomains.

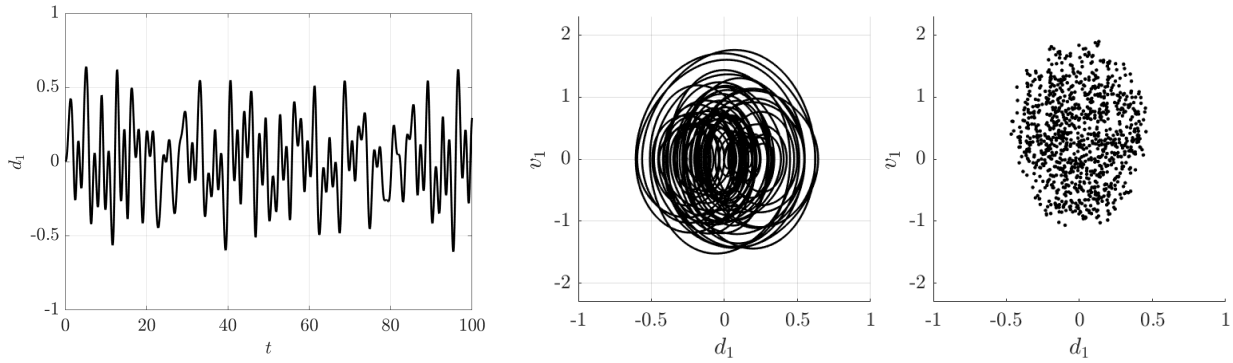

(a) Time history of displacement **(b)** Phase space **(c)** Poincaré section

FIG. 26: Time history of displacement, phase space diagram, and Poincaré section of the bottom story from the reference solution. Note that for phase space diagram and Poincaré section, we consider the simulation duration $[0, 100]$ and $[0, 4000]$, respectively.

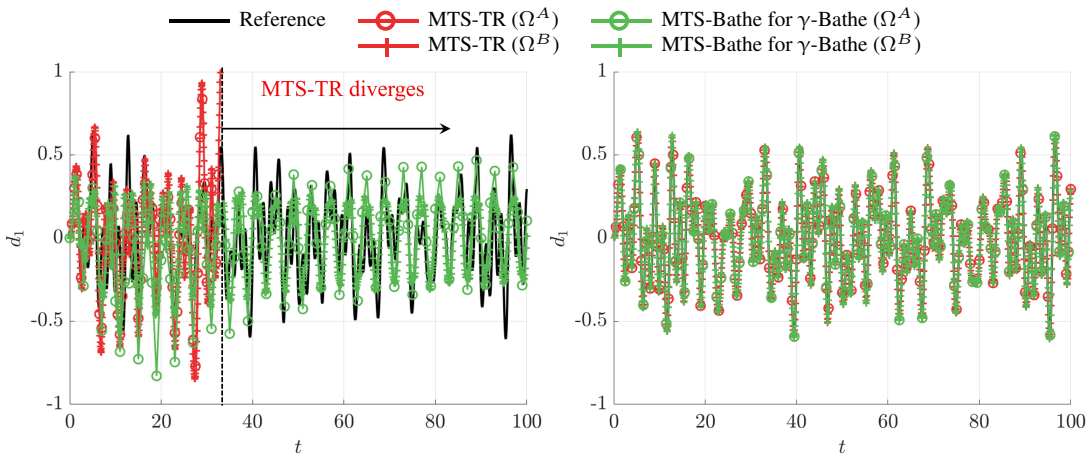

(a) $\Delta T = 1$ **(b)** $\Delta T = 0.01$

FIG. 27: Time history of displacement of the bottom ~~top~~ story when $m = 10$ ~~$m = 2$~~. Block time-step ΔT for MTS-Bathe method is taken to be twice that of MTS-TR method.

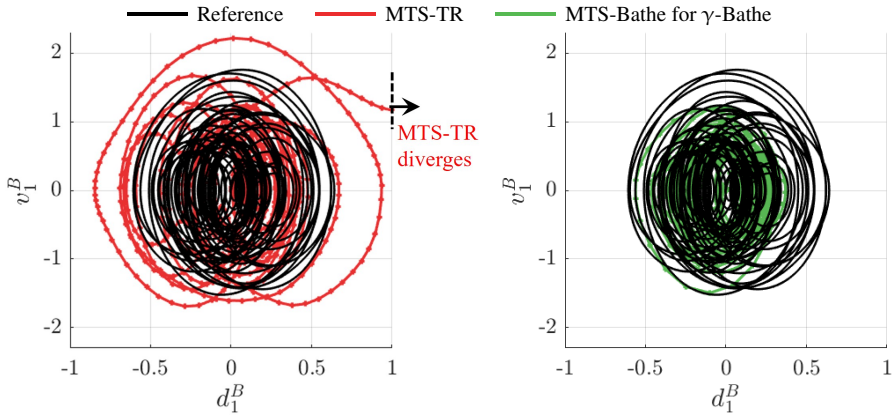

(a) $\Delta T = 1$

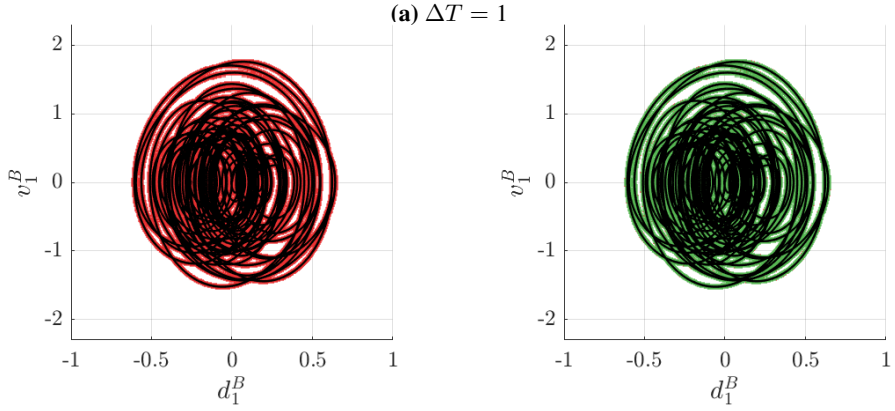

(b) $\Delta T = 0.01$

FIG. 28: Phase space diagram of the bottom story in subdomain Ω^B when $m = 10$.

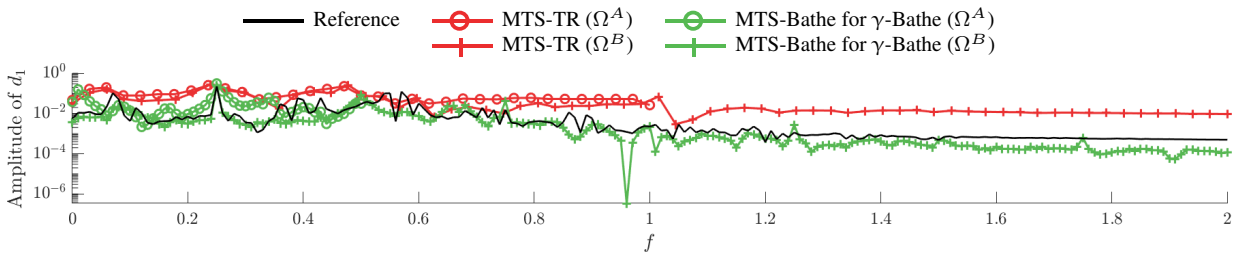

(a) $\Delta T = 1$

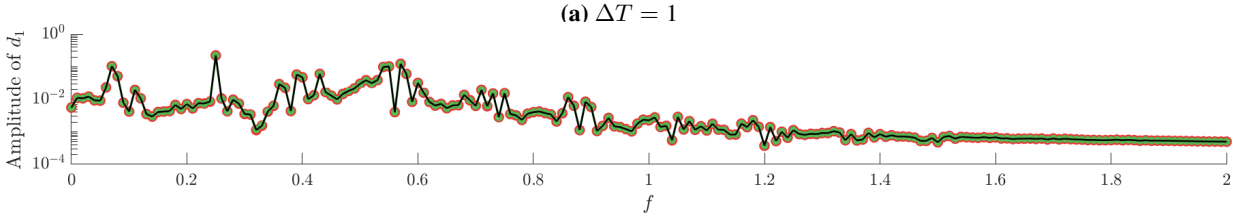

(b) $\Delta T = 0.01$

FIG. 29: Fourier spectrum of displacement of the bottom story when $m = 10$.

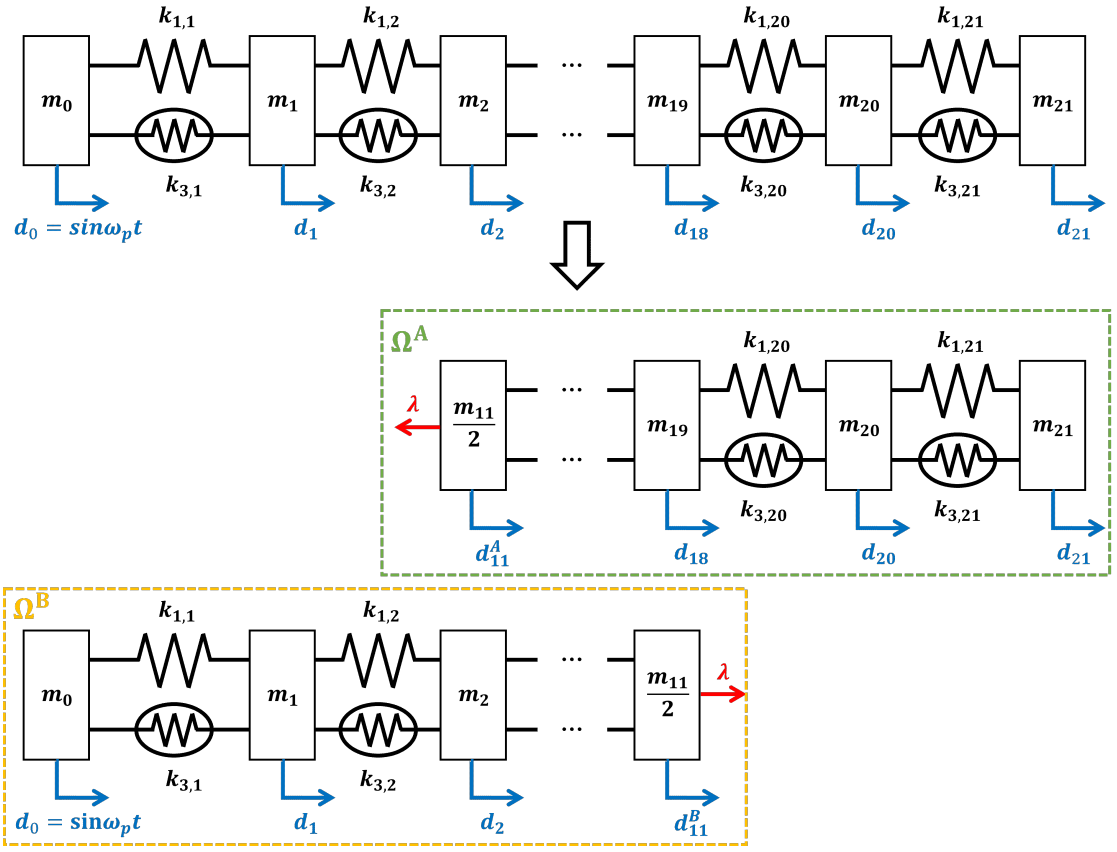

FIG. 30: Decomposition of a MDOF Duffing system into stiff (ΩB) and flexible (ΩA) parts.

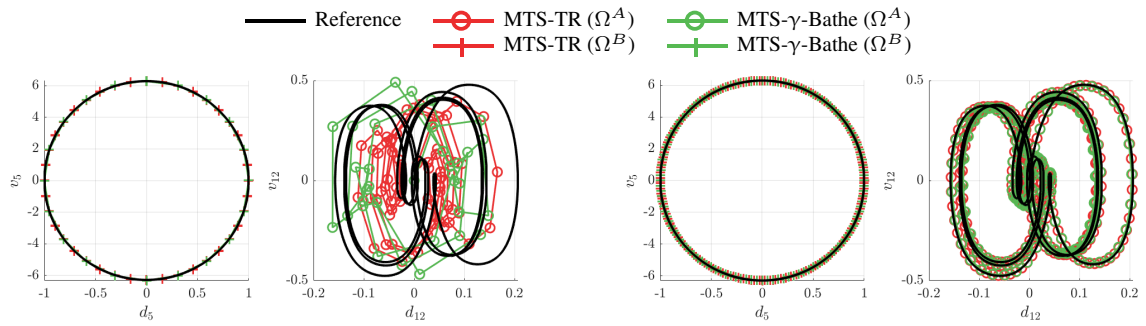

(a) $\Delta T = 0.3$ **(b)** $\Delta T = 0.05$

FIG. 31: Phase plane diagrams at nodes 5 and 12 with $m = 6$.

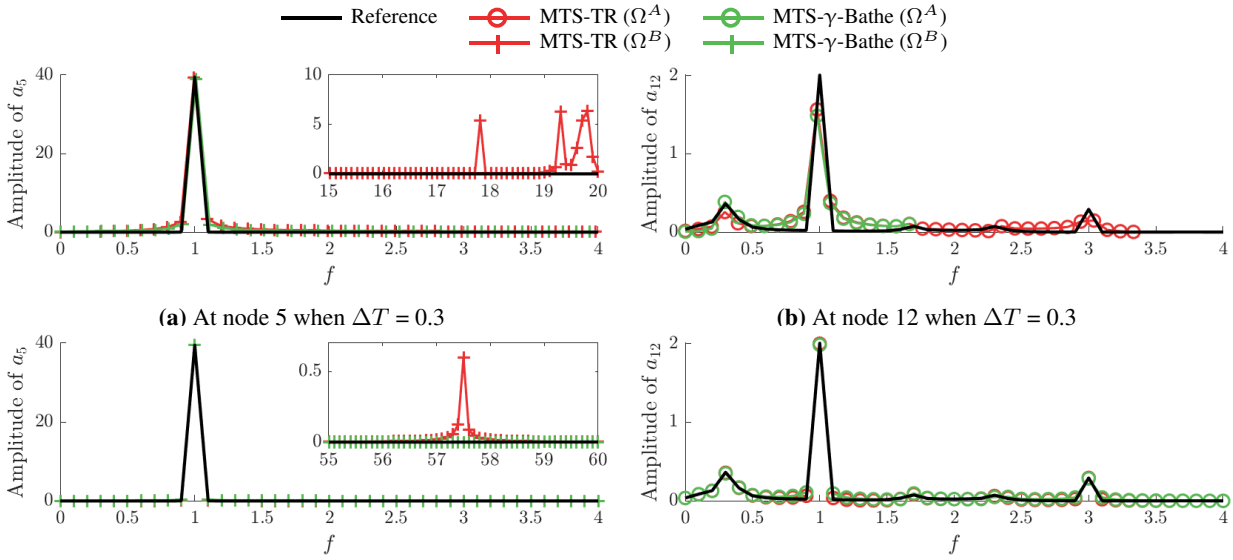

(a) At node 5 when $\Delta T = 0.3$

(b) At node 12 when $\Delta T = 0.3$

(c) At node 5 when $\Delta T = 0.05$

(d) At node 12 when $\Delta T = 0.05$

FIG. 32: Fourier spectrum of acceleration at nodes 5 and 12 with $m = 6$.

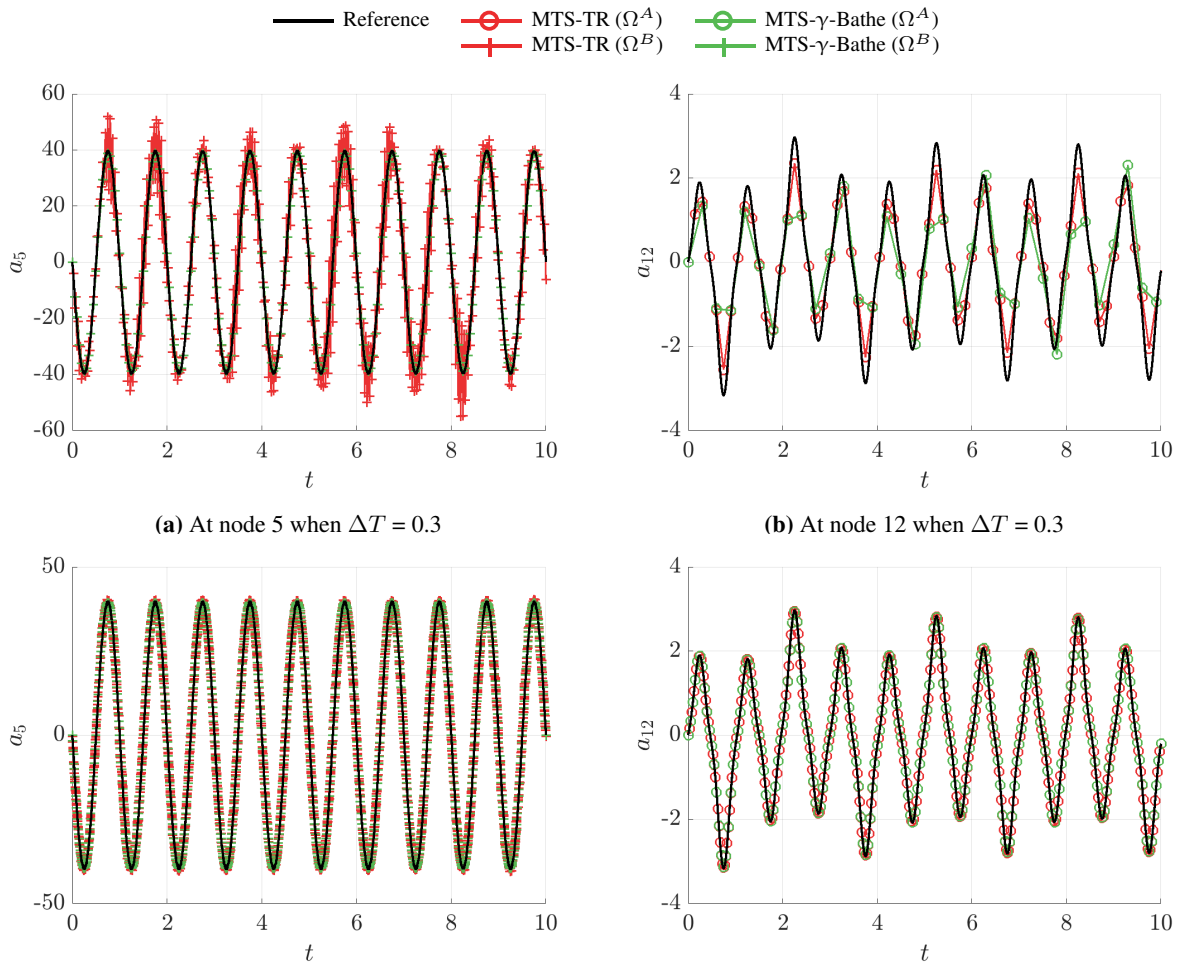

(a) At node 5 when $\Delta T = 0.3$

(b) At node 12 when $\Delta T = 0.3$

(c) At node 5 when $\Delta T = 0.05$

(d) At node 12 when $\Delta T = 0.05$

FIG. 33: Time history of acceleration at nodes 5 and 12 with m = 6

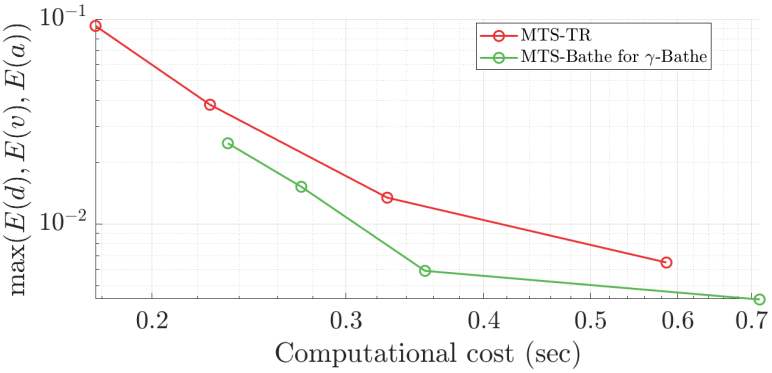

FIG. 34: Maximum value of global cumulative errors in displacement, velocity, and acceleration using the MTS-TR and MTS-Bathe methods when $m = 6$. The 4 points on each curve correspond to different $\Delta T = 0.3,\ 0.2,\ 0.1$, and 0.05 with increasing computational costs from left to right.